DEPARTMENT OF ELECTRICAL AND COMPUTER ENGINEERING

FEATURE EXTRACTION FROM OPTICAL COHERENCE TOMOGRAPHY IMAGES FOR TISSUE CLASSIFICATION

DOCTOR OF PHILOSOPHY DISSERTATION

CHRISTOS PHOTIOU

2020

DEPARTMENT OF ELECTRICAL AND COMPUTER ENGINEERING

FEATURE EXTRACTION FROM OPTICAL COHERENCE TOMOGRAPHY IMAGES FOR TISSUE CLASSIFICATION

CHRISTOS PHOTIOU

A dissertation submitted to the University of Cyprus in partial fulfillment of the requirements for the degree of Doctor of Philosophy

April 2020

VALIDATION PAGE

Doctoral Candidate: Christos Photiou

Doctoral Dissertation Title: Features extraction from Optical Coherence Tomography images for tissue classification

The present Doctoral Dissertation was submitted in partial fulfillment of the requirements for the degree of Doctor of Philosophy at the ***Department of*** *Electrical and Computer Engineering and was approved on the …… by the members of the* ***Examination Committee.***

Examination Committee:

Research Supervisor: _____

(Dr. Costas Pitris, Professor)

Committee Member: _____

(Dr Adrian Podoleanu, Professor)

Committee Member: _____

(Dr. Constantinos Pattichis, Professor)

Committee Member: _____

(Dr. Stavros Iezekiel, Professor)

Committee Member: _____

(Dr. Julius Georgiou, Associate Professor)

DECLARATION OF DOCTORAL CANDIDATE

The present doctoral dissertation was submitted in partial fulfillment of the requirements for the degree of Doctor of Philosophy of the University of Cyprus. It is a product of original work of my own, unless otherwise mentioned through references, notes, or any other statements.

…….. **[**Full name of Doctoral candidate]

…….. **[**Signature]

"If you torture the data enough, it will confess."

ΠΕΡΙΛΗΨΗ

Ένα μεγάλο ποσοστό καρκίνων πηγάζει από το επιθήλιο των οργάνων του σώματος. Πριν γίνουν επεμβατικοί, στα στάδια της δυσπλασίας και του καρκινώματος *in situ*, τα πρώιμα καρκινικά κύτταρα αλλάζουν την επιθηλιακή δομή. Πιο συγκεκριμένα, ο αριθμός των κυττάρων, και συνεπώς των πυρήνων, αυξάνεται. Οι πυρήνες γίνονται μεγαλύτεροι και υπερχρωματικοί, χαρακτηριστικά προφανή κατά την ιστολογική εξέταση. Επί του παρόντος, αυτές οι πρώιμες ανωμαλίες είναι ανιχνεύσιμες μόνο με ιστοπαθολογία ή, μη επεμβατικά, με τεχνικές οπτικής απεικόνισης όπως συνεστιακή ή μικροσκοπία πολλαπλών φωτονίων. Δυστυχώς, καμία από τις δύο τεχνικές δεν έχει εφαρμοστεί κλινικά λόγω πολυπλοκότητας και περιορισμένης διείσδυσης. Πρόσφατα, χρησιμοποιήθηκαν αλγόριθμοι μηχανικής μάθησης για την ανίχνευση ανωμαλιών και την εύρεση περιοχών που χρειάζονται περαιτέρω εξέταση, αυξάνοντας έτσι την ακρίβεια και την αποτελεσματικότητα της διάγνωσης.

Η Τομογραφία Οπτικής Συνοχής (OCT) είναι μια μη επεμβατική τεχνική ιατρικής απεικόνισης με αυξανόμενη χρήση στη διάγνωση, σε τομείς όπως η οφθαλμολογία, η καρδιολογία, η γαστρεντερολογία κ.λπ. Αντίθετα με τους υπέρηχους, λόγω της υψηλής ταχύτητας του φωτός, χρησιμοποιούνται συμβολομετρικές τεχνικές για την ανίχνευση του φωτός που οπισθοσκεδάζεται από τη μικροδομή των ιστών. Το κύριο πλεονέκτημα της είναι ότι διαθέτει ευκρίνεια παρόμοια με αυτή της ιστοπαθολογίας (1-20μm) σε πραγματικό χρόνο καθιστώντας την πολύ ελκυστική στις περιπτώσεις όπου βιοψίες δύσκολα μπορούν να εκτελεστούν.

Όταν αξιοποιηθεί πλήρως, η OCT θα μπορούσε να βελτιώσει σημαντικά τον τρόπο διάγνωσης και θεραπείας. Εκτός από την απεικόνιση της μικροδομής, η OCT μπορεί επίσης να παρέχει πρόσθετες πληροφορίες σχετικά με την κυτταρική σύσταση του ιστού. Εκτός από την εκτίμηση του πυρηνικού μεγέθους, που επιδείχθηκε νωρίτερα, η διασπορά και ο δείκτης διάθλασης μπορούν επίσης να εξαχθούν από τις εικόνες OCT και μπορούν να χρησιμεύσουν ως διαγνωστικά σημαντικοί βιοδείκτες. Επιπλέον, η ανάπτυξη ενός πλήρως αυτοματοποιημένου αλγορίθμου για τμηματοποίηση των εικόνων και εξαγωγή χαρακτηριστικών μπορεί να ενισχύσει περαιτέρω το κλινικό δυναμικό της OCT. Αυτή η διατριβή ολοκληρώνεται με σύγκριση διαφόρων αλγορίθμων ταξινόμησης ML, οι οποίοι χρησιμοποιούν χαρακτηριστικά εικόνας OCT, ως προς την ικανότητά τους να διακρίνουν και να αναγνωρίζουν ανωμαλίες στον ιστού του ανθρώπινου οισοφάγου σε πρώιμο στάδιο, κάτι που θα μπορούσε να βελτιώσει σημαντικά την καταπολέμηση των οισοφαγικών παθήσεων όπως το αδενοκαρκίνωμα.

ABSTRACT

A large proportion of cancers originates from the epithelium of various organs throughout the human body. Before they become invasive, at stages known as dysplasia and carcinoma *in situ*, early cancer cells alter the epithelial structure. More specifically, the number of cells, and therefore the number of nuclei, increases. The nuclei become bigger and become hyperchromatic, features that are obvious during histological examination. Currently, these early abnormalities are only detectable by histopathology or, non-invasively, by optical imaging techniques such as confocal or multi-photon microscopy. Unfortunately, neither of the two techniques has been clinically implemented due to complexity and limited penetration issues. Recently, machine learning (ML) algorithms have been employed to review medical images, detect abnormalities, and find regions that need further examination, thus increasing the accuracy and efficiency of diagnostic procedures.

Optical Coherence Tomography (OCT) is a noninvasive medical imaging technique with increasing use in the diagnosis of disease, in areas such as ophthalmology, cardiology, gastroenterology etc. Images are formed by measuring light backscattered from the tissue microstructures. However, unlike ultrasound (US), because of the high speed of light, interferometric techniques are utilized to detect the signal. The main advantage of OCT is that it can perform imaging at a resolution similar to that of histopathology (1-20μm), in real time, making it very attractive for applications where conventional biopsies cannot be performed.

When fully exploited, OCT could significantly enhance the way doctors and researchers diagnose and treat disease. In addition to imaging the micro-structure, OCT can also provide additional information regarding the constituents and stage of the cellular components of the tissue. In addition to the estimation of the nuclear size, which was demonstrated earlier, dispersion and index of refraction can also be extracted from the OCT images and can serve as diagnostically important biomarkers. Moreover, the development of a fully automated algorithm for tissue segmentation and feature extraction can further enhance the clinical potential of OCT. This thesis concludes with a comparison of various ML classification algorithms, which use OCT image features, for their ability to distinguish and recognize human esophagus tissue abnormalities at early stage, something that will improve the fight against esophageal diseases such as adenocarcinoma.

ACKNOWLEDGMENTS

This research project was performed under the supervision of Dr. Costas Pitris, Professor at the Department of Electrical and Computer Engineering of the University of Cyprus. First and foremost, I would like to express my deepest gratefulness to my advisor, Prof. Pitris, for his professional and patient guidance with his open-mindedness and kindness during the Ph.D. project period. His kind support and tremendous help, as well as his insightful comments and ideas and his enthusiasm about research were essential for overcoming any obstacle and for achieving the goals during this Ph.D. project. It was a great honor for me to work with Prof. Pitris and the encouragement that he gave me will be of great supportiveness for my career and throughout my whole life.

Special thanks to Dr. Stavros Iezekiel, Dr. Julius Georgiou, Dr. Constantinos Pattichis and Dr. Adrian Podoleanu for their participation in the committee. The time and effort that they spent to review the dissertation is really appreciated, while their comments have been important and helpful for improving the quality of this dissertation.

I would like to express my sincere thanks to all my colleagues at KIOS Research Center for the lovely environment and the endless friendship and their help. Special thanks to all biomedical team members of Dr. Costas Pitris for the very effective collaboration and the sharing of research experience during all these years.

Finally, I want to express the most important and the sincerest gratitude to my parents and my beloved sisters for their exceptional and unconditional love and their encouragement throughout my life.

To my parents. Thank you for everything

TABLE OF CONTENTS

LIST OF TABLES

LIST OF FIGURES

Acronyms

ANN	Artificial Neural Network
AOM	Acousto Optical Modulation
AUC	Area Under the probability Curve
BCC	Bacal Cell Carcinoma
BE	Barret's Esophagus
BOCR	Bifocal Optical Coherence Refractometry
CAD	Computer Aided Diagnosis
CCD	Charge Coupled Device
CNN	Convolutional Neural Network
COD	Correlation Of the Derivative
CSAC	Center Symmetric Autocorrelation
CT	Computed Tomography
DISR	Double Immersion Spectroscopic Reflectometry
DFT	Discrete Fourier Transform
ERCP	Endoscopic Retrograde Cholangiopancreatography
EOCT	Endoscopic Optical Coherence Tomography
FD	Fractal Dimension
FD-OCT	Fourier Domain Optical Coherence Tomography
FF-OCT	Full Field Optical Coherence Tomography
FFT	Fast Fourier Transform
FP	Fabry Perot Interferometer
FrFT	Fractional Fourier Transform
FS	Fused Silica
FWHM	Full Width at Half Maximum
GI	Gastrointestinal
GMAC	Global Minimization of the Active Contour
GTDM	Grey Tone Difference Matrix
GVD	Group Velocity Dispersion
KNN	K-Nearest Neighbors
LCI	Low Coherence Interferometry
LDA	Linear Discriminant Analysis
LISR	Liquid Immersion Spectroscopic Reflectometry
LOOCV	Leave-One-Out-Cross-Validation

LSS	Light Scattering Spectroscopy
MANONA	Multivariate Analysis of Variance
MFAC	Morphological Feature Analysis Classification
MI	Michelson Interferometer
ML	Machine Learning
MRI	Magnetic Resonance Imaging
n	Index of Refraction
NN	Neural Network
OCT	Optical Coherence Tomography
PMMA	Poly-Methyl-Methacrylate glass
PSF	Point Spread Function
RBC	Red Blood Cells
rdf	Resolution Degradation Function
ReLU	Rectified Linear Unit
ROI	Regions Of Interest
RSOD	Rapid Scanning Optical Delay
RVM	Relevance Vector Machine
sdf	Speckle Degradation Function
SGLDM	Spatial Gray Level Dependence
SS	Scatterer Size
SISR	Solid Immersion Spectroscopic Reflectometry
SS-OCT	Swept Source Optical Coherence Tomography
STFT	Short Time Fourier Transform
SVM	Support Vector Machine
TD-OCT	Time Domain Optical Coherence Tomography

CHAPTER 1
INTRODUCTION

1.1 Scope of the thesis

The vision of this PhD thesis was to enhance the capabilities of Optical Coherence Tomography (OCT) to perform accurate diagnosis of clinically challenging diseases such as cancer. Going beyond the current empirical evaluation of microstructural attributes, the extraction and combination of additional features from the OCT images could lead to detection of cell and tissue alterations at early disease stages. This work could have a particularly significant impact on the diagnosis of cancer and other malignancies, allowing much earlier detection, thus improving patient prognosis and allowing more effective disease management.

The main objective of this work was to implement novel methodologies to extract features from OCT images, such as group velocity dispersion (GVD) and refractive index (*n*) distribution of the tissue, and combine them with intensity features and nuclear size estimation, for tissue classification of esophageal disease. The classification of early tissue abnormalities could provide the ability to recognize earlier different benign or malignant areas. A fully automated algorithm is proposed for tissue segmentation and feature extraction, from regions of the epithelium, in order to evaluate the performance of different machine learning classification techniques for the discrimination of normal and abnormal areas of esophageal disease.

The tissue and other sample images of different experimental samples used in the development of the new feature extraction techniques were acquired using a Santec IVS-300 swept-source OCT system (Santec Corp., Komaki, Japan). The system has a center wavelength of 1300 nm with 60nm FWHM, axial and lateral resolutions of 12 and 22 μm respectively and an imaging depth range of 4 mm (in air).The methods developed were subsequently applied to *in vivo* OCT images from a Massachusetts General Hospital (MGH) study involving patients with esophageal disease. Those images were acquired with a swept source EOCT system with a centre wavelength of 1300 nm, an axial resolution of 10 μm and an A-Scan rate of 40 kHz. Each catheter rotation produced 2,048 A-Scan, displayed in real-

time, and multiple cross-sectional esophagus images were collected as the catheter was manually pulled up from the gastroesophageal junction.

1.2 Dissertation outline

Chapter 1 begins with an introduction and the scope of the proposed thesis. Chapter 2 presents a background as well the theory and applications of OCT. The first part of this chapter is a general introduction to OCT. In the second part, the development of the OCT from a historical perspective is presented, including an overview of the technology and the capabilities of the OCT imaging systems. In the third part, some basic theoretical background is provided and finally clinical applications of OCT are presented.

Chapter 3 includes the literature analysis of the different features and classification methods that have been evaluated in this thesis. It begins with an analysis of various methods that can be used to measure the GVD and diagnostic potential of this feature. A review of index of refraction estimation methods and the evaluation of the feature as a potential biomarker follows. A new metric known as the correlation of the derivative bandwidth, used for nuclear size estimation, is also presented. Furthermore, there is an analysis of the features that are generally used for medical imaging classification and which are suitable for OCT. The chapter closes with an assessment of the machine learning techniques used over the last decades for OCT images classification.

Chapter 4 proposes a novel technique for GVD estimation by using the image speckle at different depths that is applicable for *in situ* and *in vivo* measurements. Chapter 5 presents a second novel technique for GVD estimation, based on extension of the walk-off method, which uses novel image processing algorithms and it is also applicable for *in vivo* application. Chapter 6 presents a detailed comparison of existing methods and the two new techniques developed for GVD estimation to elucidate their capabilities and limitations as well as examine their applicability to tissue measurements. Chapter 7 introduces of a new technique for index of refraction estimation that uses images from various angles to estimate this important optical parameter from *in vivo* and *in situ* measurements. Chapter 8 describes the classification of different human esophagus regions as normal, Barret's and dysplastic tissue comparing different intensity statistics in combination with features that were developed within this thesis.

The thesis ends with conclusions and future plans. It highlights the fact that the contribution of the new methods developed for feature estimation could be easily applicable

in vivo and, along with an automated algorithm created for image segmentation and feature extraction, could be used for effective image classification.

1.3 Contribution

On the way, as a result of this research project two novel techniques were developed that are applicable to *in vivo* tissue dispersion measurements. They were validated and compared with existing methods to provide proof of their applicability to samples with different scattering properties such as human tissues. Furthermore, a novel technique for index of refraction estimation that can be also applied for *in situ* and *in vivo* measurements was demonstrated. Finally, this thesis concluded with a comparison of classification using various machine learning methods utilizing features extracted from an automated algorithm developed for this study. The results proved that the proposed methods and algorithms for tissue segmentation and feature extraction can be effectively used for tissue classification in a clinical application to assist medical diagnosis without the need of highly complicated optical or computationally expensive systems.

List of Publications

Refereed Archival Journal Publications

1. Christos Photiou, Costas Pitris, "Dual-angle optical coherence tomography for index of refraction estimation using rigid registration and cross-correlation," J. Biomed. Opt. 24(10), 106001 (2019), doi: 10.1117/1.JBO.24.10.106001.
2. Christos Photiou, Costas Pitris, "Comparison of tissue dispersion measurement techniques based on optical coherence tomography," J. Biomed. Opt. 24(4), 046003 (2019), doi: 10.1117/1.JBO.24.4.046003.
3. Christos Photiou, Evgenia Bousi, Ioanna Zouvani, Costas Pitris, "Using speckle to measure tissue dispersion in optical coherence tomography", Biom. Opt Exp.May 1; 8(5): 2528–2535. (2017)

Refereed Archival Conference Proceedings

1. Photiou Christos, George Plastiras, Guillermo Tearney, and Costas Pitris. "Comparison of classification methods of Barret's and dysplasia in the esophagus from in vivo optical coherence tomography images." In *Optical Coherence Tomography and Coherence Domain Optical Methods in Biomedicine XXIV*, vol. 11228, p. 1122820. International Society for Optics and Photonics, 2020.
2. Christos Photiou, Costas Pitris, "Index of refraction estimation using dual-angle OCT," Proc. SPIE 10867, Optical Coherence Tomography and Coherence Domain Optical Methods in Biomedicine XXIII, 108673S (22 February 2019); doi:10.1117/12.2510925

3. Christos Photiou, Evgenia Bousi, Ioanna Zouvani, Costas P., "Measuring tissue dispersion using the cross-correlation of half-spectrum optical coherence tomography images," Proc. SPIE 10867, Optical Coherence Tomography and Coherence Domain Optical Methods in Biomedicine XXIII, 108670D (22 February 2019); doi: 10.1117/12.2510949.
4. Christos Photiou, Costas Pitris, "Tissue dispersion measurement techniques using OCT," Proc. SPIE 10053, Optical Coherence Tomography and Coherence Domain Optical Methods in Biomedicine XXI, 100532W (17 February 2017); doi: 10.1117/12.2251681
5. Christos Photiou, Evgenia Bousi, Ioanna Zouvani, Costas Pitris, “Using speckle to measure tissue dispersion in optical coherence tomography”, Proc. SPIE 10053, Optical Coherence Tomography and Coherence Domain Optical Methods in Biomedicine XXI, 100532W (17 February 2017).
6. Christos Photiou, Evgenia Bousi, Ioanna Zouvani, Costas Pitris, “Measuring Tissue Dispersion Using Optical Coherence Tomography Speckle”, Optical Coherence Imaging Techniques and Imaging in Scattering Media II, edited by Maciej W., S. A. Boppart, Wang-Yuhl Oh, Proc. of SPIE-OSA Vol. 10416, 104160H (2017) SPIE-OSA · CCC code: 1605-7422/17/$18 · doi: 10.1117/12.2287737.
7. Christos Photiou, Evgenia Bousi, Ioanna Zouvani, Costas Pitris, “Extracting Dispersion Information from Optical Coherence Tomography Images”, IEEE International Symposium on Signal Processing and Information Technology. (2016).

CHAPTER 2
OPTICAL COHERENCE TOMOGRAPHY

2.1 Introduction

Optical coherence tomography (OCT) is an interferometric non-invasive imaging technique that can be used to obtain high resolution images of a sample's internal micro-structure [1]. OCT has been extensively used for medical imaging, especially for ophthalmologic pathologies, but also in cardiology, gastroenterology, cancer diagnosis, tissue optics and engineering. Further applications were also developed for other fields such as industrial non-destructive testing, optical fiber and polymer composite characterization and even in the jade industry [2], [3], [4]. OCT, originally conceived in 1991, offers many advantages such as safety, since it uses near infrared (NIR) light, and cost, since it is based on mass produced fiber-optic communication technology. More significantly, OCT also provides non-contact, non-or minimally invasive imaging, suitable for *in vivo* use, a great advantage for medical applications.

Axial scanning of the system results to one-dimensional A-Scans that include the depth-dependent backscattered intensity in the sample along the beam's path that reaches a static detector that is typically coaxial with the source. Two-dimensional cross-sectional OCT images of tissue are constructed by juxtaposing a series of axial measurements at different transverse positions. The resulting data set is a two-dimensional array, which represents the optical backscattering within a cross-sectional slice of the tissue. Three-dimensional imaging can also be created by stacking the two-dimensional cross-sectional images at different transverse positions (Figure 2.1). In OCT, the axial and the transverse imaging resolutions are independent. The axial resolution is mainly determined by the coherence length of the light source and is decoupled from the beam focusing which determines the transverse imaging resolution. The probe beam sources of OCT exhibit short temporal coherence length, high spatial coherence and point-source-like properties. Some examples include superluminescent diodes, femto second pulses, wavelength scanning sources [5].

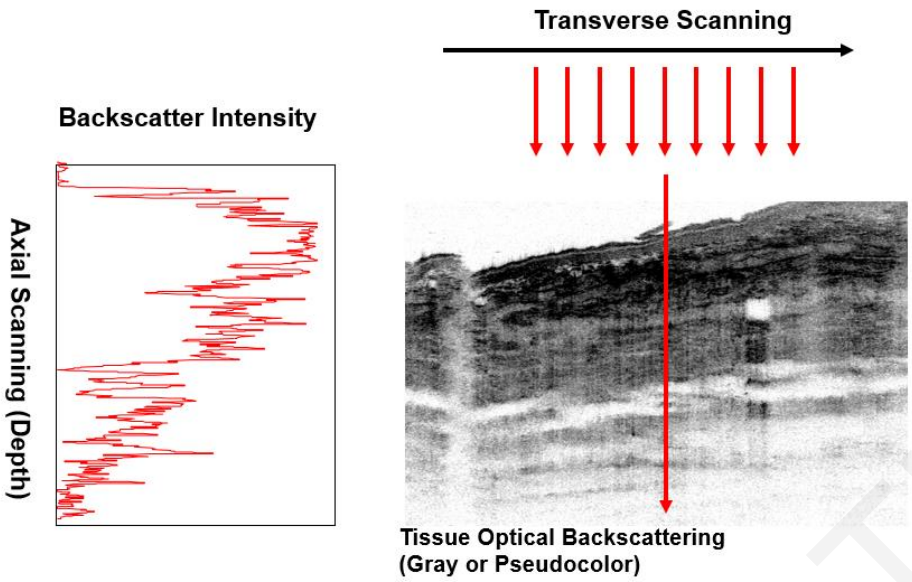

Figure 2.1. From left to right: Axial scanning of an OCT system (A-scan), cross-sectional scan (B-scan) obtained by combining a series of axial scans.

The axial (depth) resolution of an OCT system is usually ~ 2-15 μm, which is 10 to 100 times better than standard ultrasound imaging [6]. For ultrasound frequencies of ~100 MHz a resolution of 15–20 μm can be reached. However, high frequencies are highly absorbed by biological tissues thus limiting the imaging depth. Other optical techniques, including confocal multi-photon microscopy, can provide very high resolution but they are clinically limited by poor imaging depth and it is difficult to apply them *in vivo*. Instead, OCT can achieve one micrometer resolution *in vivo* OCT imaging using femtosecond laser sources [7]. From a resolution and penetration depth perspective, OCT fills the gap between optical imaging (confocal and multi-photon microscopy) and conventional clinical imaging (ultrasound, X-ray, MRI) technologies. The major advantage of OCT is its ability to acquire high resolution images in real-time, *in situ* and *in vivo*. Although penetration can only reach a few millimeters (~3mm), OCT is extensively used for micro-structural characterization and detection of abnormalities in many tissues.

OCT imaging has a number of features, which make it attractive for a broad range of applications. It can perform imaging with resolutions approaching that of conventional histopathology, while at the same time imaging is possible *in situ* and in real time. OCT can be implemented fiber-optically using devices such as handheld probes, endoscopes, catheters, laparoscopes, and needles that enable non-invasive or minimally invasive internal body imaging. OCT can be performed in real time, allowing guidance of excisional biopsy or interventional procedures. 3D-OCT data sets provide comprehensive, volumetric information on architectural morphology. Cross-sectional images with arbitrary orientations, as well as projection and rendered views, can be generated. OCT data is in digital form,

facilitating quantitative image processing techniques as well as electronic storage and transmission. OCT technology has significantly improved over the past few years with the introduction of fast, high resolution OCT systems which are uniquely suited for *in vivo* applications. However, some tissue and cellular changes, which are characteristic hallmarks of cancer, remain below the resolution limit of OCT. Diagnosis is further limited by lack of contrast at the cell or tissue level. The extraction of features from the OCT images, characteristic of many intrinsic tissue parameters, can significantly enhance OCT's clinical capabilities for early detection and diagnosis of malignancies [1], [7], [8].

2.2 Theory and operation

OCT is based on low coherence interferometry (LCI) using a Michelson interferometer (MI). Interferometric detection can measure the light backscattered from the sample with high sensitivity and dynamic range. LCI is performed with a low coherence length light source. One arm of the interferometer illuminates the tissue and collects the backscattered light (sample arm). The other arm, is scanned as a function of time (reference arm). Path delay comes between the two arm lengths and is not restricted to one arm. Optical interference between the light from the sample and reference arms occurs only when the optical delays match to within the coherence length of the light source (Figure 2.2).

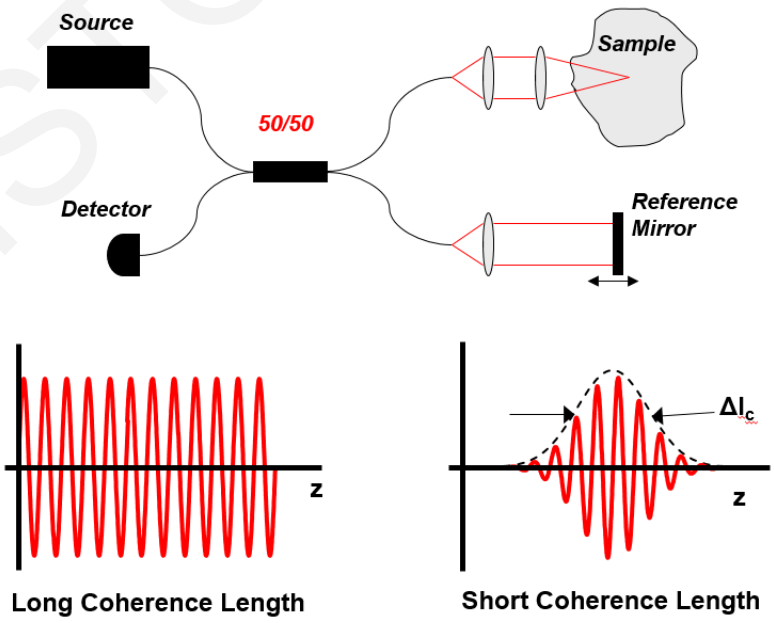

Figure 2.2. Schematic of low coherence interferometry.

In a typical configuration, OCT records a series of adjacent axial scans (A-scans) to construct a cross-sectional image of the object. Each of the A-scans contains the depth-dependent intensity of reflections or back scattering in the sample along the beam's path that reach the detector. The depth dimension of an A-scan represents the optical distance, i.e. the product of the refractive index and the geometric length. In addition, the contrast mechanism of the image is the refractive index profile, since scattering occurs at index changes, and allows one to distinguish sites of different optical properties in the sample. Two main forms of OCT have been developed independently. Time-Domain and Fourier-Domain OCT [9].

2.2.1 Time - Domain OCT (TD-OCT)

The first OCT systems developed were Time-Domain OCT (TD-OCT) systems and were first reported in 1991 for imaging of the human retina *in vitro* [10]. In TD-OCT the reference arm is scanned to determine the path length of the light backscattered from the sample. Interference occurs only if the sample path length equals the reference path length. For sufficiently short coherence length lasers, inhomogeneity regions within the sample will create independent interference patterns. For that purpose, the coherence length of the source should, thus, be less than half of the sample's internal structure scale. The major limitation of TD-OCT is that the imaging speed is restricted because of the need to scan the reference mirror. It requires accurate mechanical scanners and the imaging speed cannot usually exceed a hundred A-Scans per second.

In TD-OCT, the optical depth ranging is achieved by physically scanning the reference arm mirror. A simple TD-OCT system with the interference signal and the A-Scan envelope is shown in Figure 2.3. When both arms have a mirror, for simplicity reasons, the backscattered intensity of light to the detector can be presented as a function of the arms path length difference ΔL as:

$$I_d(\Delta L) = I_s + I_r + 2\sqrt{I_s I_r}\,|\,\Im\{S(k)\}\,|\cos(k_0 \Delta L) \qquad (2.\ 1)$$

where *Is* and *Ir* are the light intensities reflected from the sample and the reference arm respectively, $k_0=2\pi/\lambda_0$ is the average wave number and the relation $\lambda_0=c/f_0$ is used to transform from the time domain to the path domain. *S(k)* is the power spectrum of the light source [9] [11] [12].

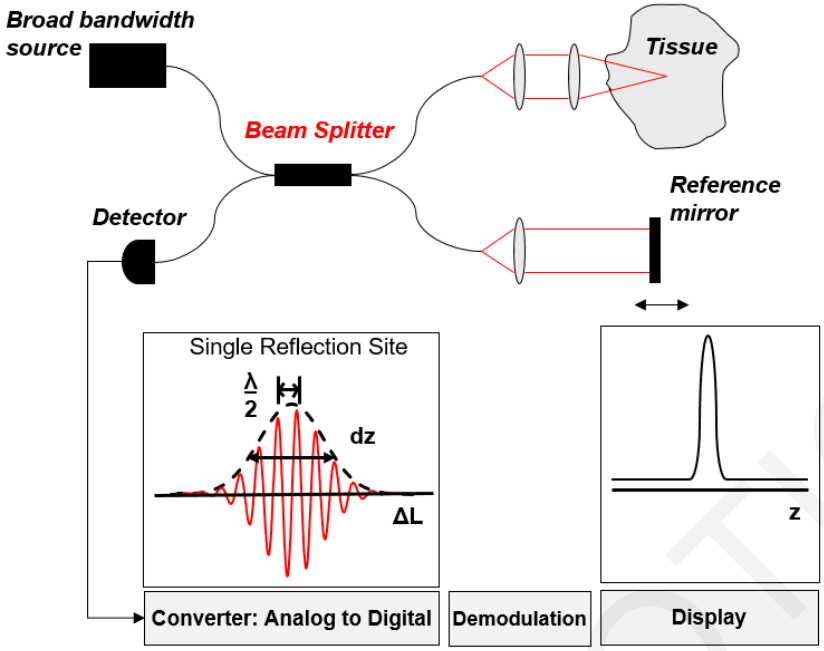

Figure 2.3. Fiber Optic implementation of Time Domain low coherence interferometer, interferogram, and the AScan envelope.Where ΔL is the optical path length difference and dz the coherence length.

2.2.2 Fourier - Domain OCT (FD-OCT)

Fourier Domain OCT (FD-OCT), proposed by Fercher in 1995, is based on Wolf's inverse scattering solution for objects with limited scattering properties [13]. It relies on the relation between the Fourier components of the object's scattering potential and the Fourier components of the scattered field detected outside the object. In FD-OCT, there is no movement of the interferometer arm and the intrinsic morphology of the sample, which is encoded in the spectral response, is extracted by Fourier transformation. Substituting the moving mirror with a dispersive grating was introduced by Schwider in 1994 to assess the surface profile of a material. FD-OCT can be utilized for measurements of the retina as well as for measurements of high scattering skin [13], [14].

In FD-OCT, depth information is provided by an inverse Fourier transform of the spectrum of the backscattered light. A simplified optical setup of a FD-OCT system is shown in Figure 2.4. The amplitude of the spectrum of the light backscattered from the sample $I(k)$ is acquired using a spectrometer. The interference spectrum for a single scatterer at a distance from the reference plane is a cosine function multiplied by the spectrum of the source $S(k)$. Analytically, the interference signal from multiple scatterers is given by the spectral intensity distribution of the light source times the square of the sum of the back reflected reference and sample signals [9], [8]:

$$I(k) = S(k)\left|a_R \exp(j2kr) + \int_0^{\infty} a(z)\exp(j2k(r+n(z).z)\,dz\right|^2 \qquad (2.\ 2)$$

k: wavenumber $k=2\pi/\lambda$

r: path length in the reference arm

$r+z$: path length in the object arm

z: path length in the object arm, measured from the reference plane

z_0 : offset distance between reference plane and object surface

n: refractive index (n = 1 for $z < z_0$ and varying depending on the sample for longitudinal positions in the object $z > z_0$)

aR: reflection coefficient of the reference

$a(z)$: backscattering coefficient of the object signal, a(z) is zero for $z < z_0$

$S(k)$: spectral intensity distribution of the light source

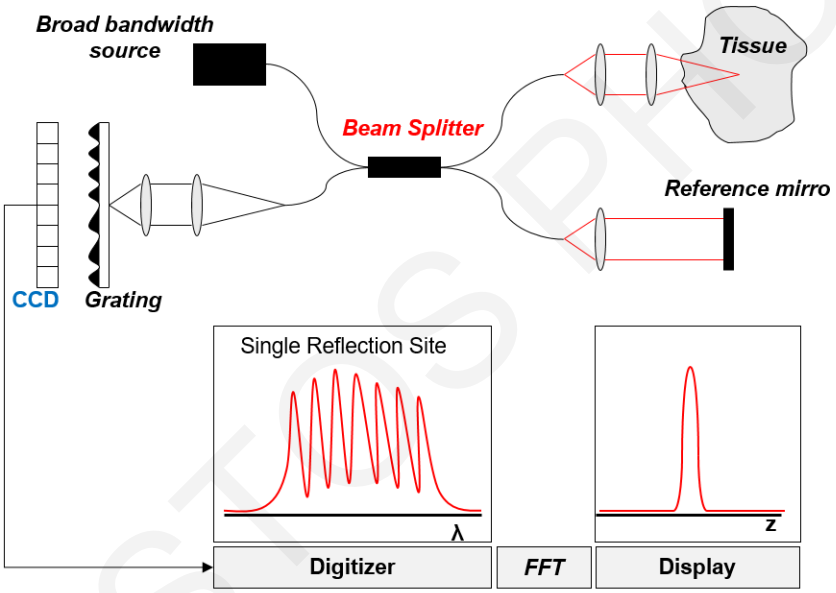

Figure 2.4. Fiber-optic implementation of Fourier Domain low coherence interferometer, spectrogram, back reflection profile.

FD-OCT measures the signal in the Fourier domain and, by Fourier transformation, provides the scattering profile in the spatial domain. The inverse Fourier transform of the recorded spectral intensity yields the same line scan signal as obtained by standard LCI and provides a back reflection profile as a function of depth. In contrast to TD techniques, the time-consuming mechanical reference arm scan is replaced by a spectral measurement. In addition, since all the backscattered light is detected simultaneously, the signal-to-noise ratio (SNR) and sensitivity of FD-OCT is superior to TD-OCT. FD-OCT significantly improves the detection sensitivity and allows much higher scan speeds than TD-OCT systems. The short acquisition time, the lack of moving parts and the direct access to spectral information has made FD-OCT more preferable over TD-OCT [14], [15].

FD-OCT has its limitations and some artifacts that must be mentioned. The interference pattern includes direct DC, autocorrelation and cross-correlation parts (Figure 2.5). To avoid overlap of the autocorrelation and cross-correlation component, the mismatch length between the sample and the reference arms must be longer than the optical thickness of the sample. However, this introduces other issues. Higher frequency features in the resulting spectra require a higher resolution spectrometer to support the same detectable range inside the sample thus imposing demanding requirements on the spectrograph and CCD camera [15]. The system signals also display conjugate artifacts. As the signal of the spectrum is a real function, its Fourier transform is Hermitian and the created image holds both the sample and its mirror image. These artifacts can be eliminated by phase shifting interferometry (PSI) also known to as Phase Stepping Interferometry or computationally with intelligent algorithms [16], [17], [18].

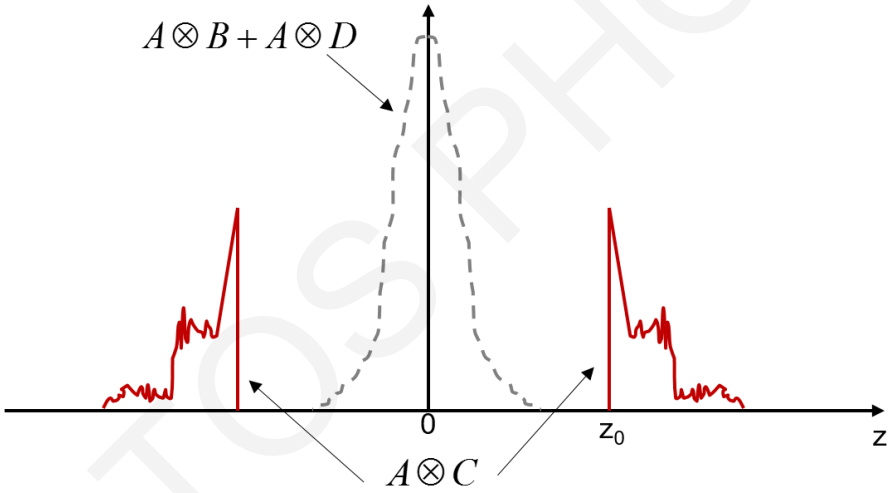

Figure 2.5. Amplitude of the results of the Fourier transform of the spectral interferogram recorded with FD-OCT. DC term: $A \otimes B$: source spectrum (correlogram), $A \otimes D$: autocorrelation terms of mutual interference. $A \otimes C$: symmetric cross-correlation terms of tissue scattering amplitude.

In Swept Source OCT (SS-OCT), a variation of FD-OCT, the wavelength-dependent intensity data are not recorded simultaneously by using a broadband light source and a spectrometer. Instead, they are recorded sequentially, with a single photodetector while tuning the wavelength of the light source. If the tuning of wavelength λ of the laser (Figure 2.6) is constant, the intensity at the photodetector can be calculated as**:**

$$I = I_s + I_r + 2\sqrt{I_s I_r}\cos(2\pi\Delta\Phi) \qquad (2.\ 3)$$

where I_s and I_r are the light intensities reflected from the sample and reference, respectively. $\Delta\Phi = 2Lk/2\pi$ is the phase difference between the two beams.

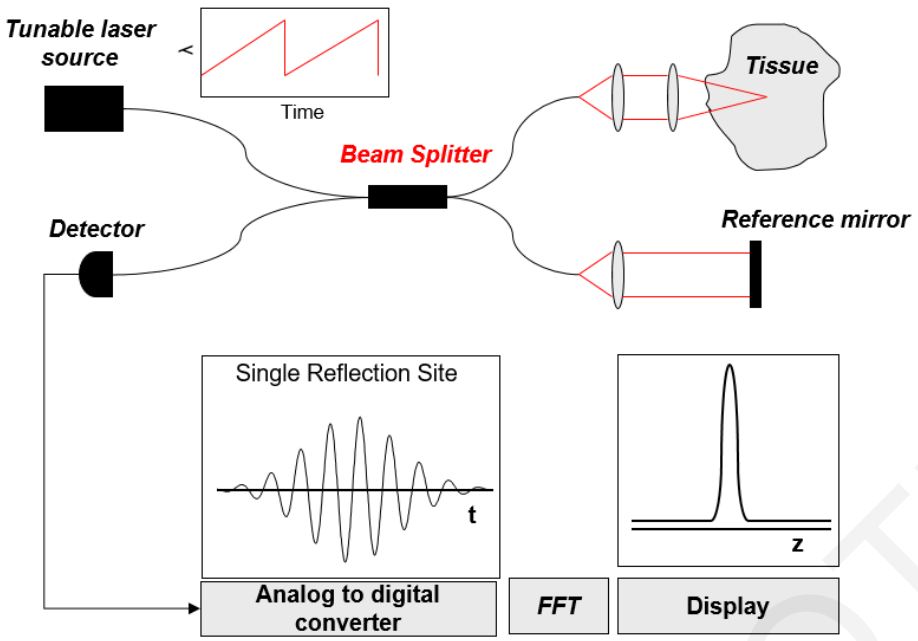

Figure 2.6. Fiber-optic implementation of Swept Source low coherence interferometer, interferogram, and back reflection profile.

As in the case of FD-OCT, the main advantage of this technique, as compared to TD-OCT systems, is that the reference arm length is fixed and no moving parts are required. This significantly increases the speed of scanning. Compared to FD-OCT, SS-OCT also offers high data acquisition speed and improved SNR and sensitivity. In addition, using two photodetectors, in a heterodyne configuration, provides the added advantage of easy rejection of the unwanted DC intensity terms and improved SNR. This enhances the usable dynamic range of the detection system considerably. The main disadvantage of this approach is that the light sources are expensive and only available for a limited range of wavelengths. However, this limitation will probably be circumvented in the near future [9], [8] [19].

2.3 OCT clinical applications

As mentioned before, many features of OCT make it uniquely suited for clinical applications. OCT can image in high resolution, non-or minimally invasive, in real time, without the need to process a sample as in conventional biopsy and histopathology. It, thus, allows pathology to be monitored *in situ* and can enable real time diagnosis and enable surgical guidance [9] [17]. OCT is fiber-optically implemented and can, therefore, combined with a wide range of instruments including catheters, endoscopes, laparoscopes, and surgical probes. This allows access to many internal organ systems. Finally, OCT is compact and portable, which is an important feature for a clinically viable device. The most developed

clinical OCT applications are those focusing on ophthalmology [20] [21], cardiovascular pathologies [22], [23], dermatology [24], [25], [26] [27] and GI tract imaging [28], [29], [30] [31]. Table 2-1 shows an overview of the OCT imaging applied in various medical fields. OCT technology has been utilized for surgery image-guidance in many medical disciplines [32], [33], [34], [35]. Table 2-1 shows the estimates cancer deaths in the USA, and therefore, OCT imaging is able to detect and diagnose different kind of cancers [36], [37], [38], [39], [40], [41], [42], [43], [44], [45], [46].

OCT could be suitable for three general scenarios in the diagnosis of malignancies. First, OCT can guide standard excisional biopsies to decrease false negative results. This can improve the accuracy of biopsy and reduce the number of biopsies that are taken, resulting in better prognosis as well as significant cost savings. Second, it may be possible to use OCT to directly diagnose or grade disease. This application will be more challenging since it implies making a diagnosis based on OCT rather than conventional histopathology. Scenarios include situations where OCT could be utilized to grade early neoplastic abnormalities or detect the depth of neoplastic invasion. Third, diagnosis and treatment might be performed in real time based on OCT imaging. This would require that the OCT diagnostic information is directly coupled to the treatment decisions. The integration of diagnosis and treatment could lessen the number of patient visits, resulting in an important decrease in health care expenses and enhance patient compliance. Each of these scenarios demands a different level of OCT performance not only in its aptitude to image various tissues, but to attain the obligatory level of sensitivity and specificity for each clinical situation. Thus for, using empirical image features, radiologists can discriminate varius glands and tisuues from OCT images [47], [48]. More recently, researchers are using machine learning models for automatic classifocation of OCT images in an effort to find less time consuming diagnosis procrdures (to be covered in Chapter 3).

TABLE 2-1. OCT IMAGING STUDIES ON DIFFERENT MEDICAL APPLICATIONS

Medical Fields	Clinical Application	References
Ophthalmologic Pathologies	Retinal pathologies evaluation Surgery, guidance	Karst 2019 [21] Eladawi 2018 [20]
Oral Cancer	Surgery guidance, malignancies detection	Capocasale 2018 [49]
Gastroenterology	GI tissue discrimination Endoscopic procedures Colon cancer identification Stomach carcinoma Hepatic cancer detection Esophagus malignancies recognition	Tearney 1997 [50] Li 2017 [28] Luo 2019 [51] Struk 2018 [31] Zhu 2015 [52] Liang 2016, Lee 2017 [29], [53]
Skin Pathologies	Imaging, Skin cancer Examination of burn wounds	Podoleanu 2000 [24] Rajabi 2019 [26] Iftimia 2018 [25] Rangaraju 2019 [27]
Urology	Prostate cancer assessment Bladder condition diagnosis Renal disease assessment	Singh 2019 [39] Xiong 2019 [38] Onozato 2010 , Lee 2012 [37], [36]
Breast	Cancer surgery guidance Cancer imaging	Boppart 2004a [32] El Haddad 2017 [54] Scolaro 2014 [40] Ha 2019 Butola 2019 [41], [42]
Neural - Brain	Surgery guidance Brain imaging	Milner 2019 [33] Baumann 2019 [43]
Gynecology	Cervical cancer evaluation Ovarian cancer assessment	Malone 2020 [44] Wang 2015, Peters 2016 [45], [46]
Cardiology	Acute coronary syndrome assessment Stent thrombosis detection	Samir 2015 [23] Joner 2018 [22]
Respiratory	Lung pathologies detection	Hariri (2015, 2016) [55], [56]
Endocrinology	Nodes, tissues and thyroid discrimination Thyroid cancer screening Surgery guidance	Ladurner 2013 [47] Zhou 2010 [48] Sommerey 2015 [35] Erickson 2018 [34]

In dermatology, researchers have investigated the diagnostic accuracy of OCT in distinguishing basal cell carcinomas (BCC) *in vivo*. Those studies yielded promising results with sensitivity and specificity ranging from 80 to 93 and 84 to 95%, respectively [57], [58]. In addition, Ulrich et al., examined the diagnostic value of OCT combined with clinical and dermoscopic evaluation. The study showed a better diagnostic accuracy compared to clinical and dermoscopic information, with sensitivity and specificity of 96 and 75%, respectively. However, even for skilled observers, it was very challenging to discriminate BCC from actinic keratosis, which suffered from a 50% error rate [58], [59].

Oral cancer, especially squamous cell carcinoma, is mainly treated by a mixture of surgery and radiotherapy. Because of the difficult location and the neighboring structures, it is crucial to achieve complete tumor removal. OCT utilized in various studies to evaluate its potential to distinguish between malignant and benign oral tissue with promising diagnostic accuracies (82%). The morphological characteristics were verified by quantitative analysis, but no studies have yet been performed for real-time assessment of the surgical resection margins [60], [61] [49].

Furthermore, OCT was also evaluated for the visualization of lung cancer during bronchoscopy and after surgery on resected specimens. Bronchial malignancies were primarily defined on OCT images by a thickened epithelium wall and loss of sub epithelial identifiable microstructures. Tumor invasion was shown as loss and/or disturbed architecture of the basement membrane [62], [63], [64]. While the diagnostic accuracy was quite high (81.8 to 83.3%), OCT during bronchoscopy it is yet not sufficiently sensitive to completely replace biopsy. Although OCT has the prospective to be applied during bronchoscopic procedures for the diagnosis of lung tumors, valuation of tumor margin detection during surgery was not been assessed [55].

For breast cancer, OCT was evaluated for tumor and sentinel lymph node detection in breast cancer patients, using various criteria. It was shown to have high diagnostic accuracy (84%) in boundary assessment compared to histology (Figure 2.7). A handheld OCT system with a camera, which could be used during surgical procedures, was also considered for margin assessment and provided very good results. For lymph node detection, Full-field Optical Coherence Tomography (FF-OCT) was capable to discriminate malignant invasion of lymph nodes from benign lymph nodes with high sensitivity and specificity (89 and 87%) [65] [66] [67] [68] [69].

Several studies, assessed the use of OCT for the diagnosis of ovarian cancer, of which two during surgery. Studies evaluated the tumor characteristics based on qualitative image analysis using SS-OCT or FF-OCT (Figure 2.8) [46], [70] , [71]. Ovarian malignancies were distinguished by the appearance of hyperintense regions with irregular patterns, which turned out to be disorganized collagen fibers. Metastases could also be detected as shown by Peters et al [46]. Additionally, some studies analyzed tumor images quantitatively, focusing on optical coefficients, which were extracted from normalized histograms After building a logistic classifier model, Nandy et al., were able to achieve

sensitivity and specificity of 91.6% and 87.7% for tumor classification from FF-OCT images [72], [73].

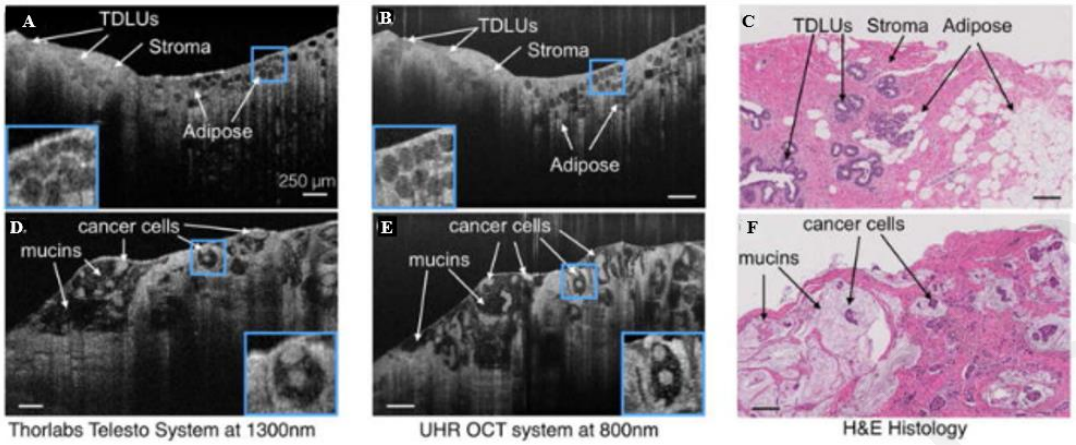

Figure 2.7. Comparison of OCT B-scans taken from different OCT systems (A,B,D,E) and their histopathological correlations (C,F). (A)–(C) show an example of normal breast tissue, with adipose, stroma and ducts. (D)–(F) show mucinous carcinoma. Insets: zoom-in view of adipose region, covering 0.3mm by 0.3mm area. Scale bar: 250 µm. [68]

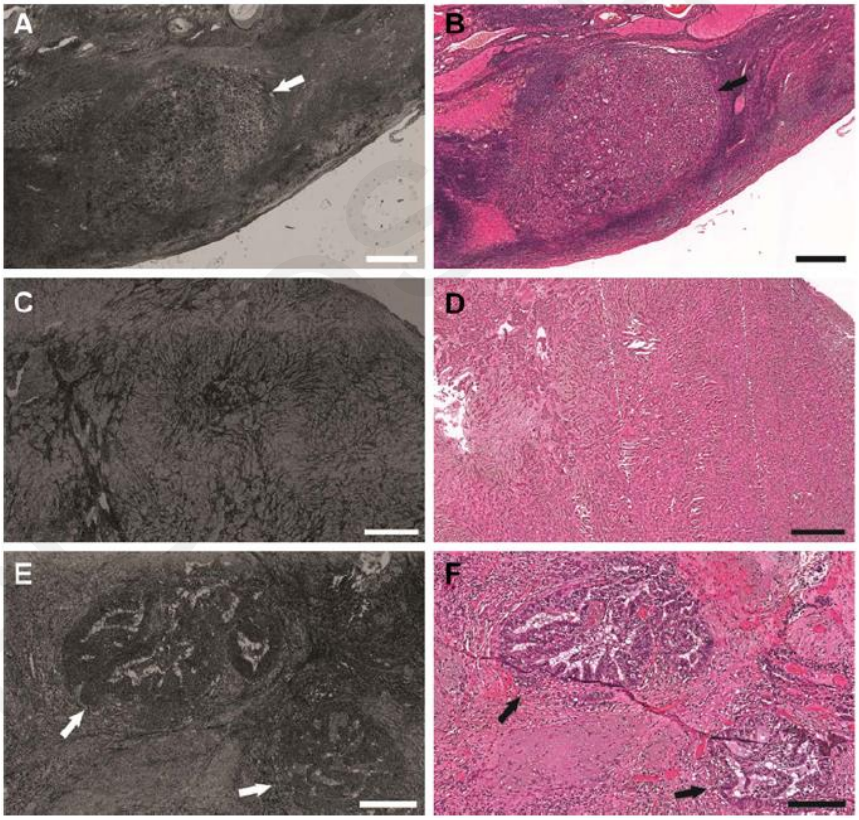

Figure 2.8. FF-OCT images (left column) and corresponding histology images (right column) of ovarian metastases. An ovary containing a solitary metastasis is shown in A and B (indicated by arrows). An ovary with disseminated breast tumor cells is shown in C and D. Micrometastases originating from endometrial carcinoma are shown in E and F (indicated by arrows); scale bars, 500 (A–D) and 200 mm (E–F). [46]

OCT was also applied effectively in the gastrointestinal tract. It was utilized for malignant and benign pancreatic duct strictures discrimination both *in vivo* and *ex vivo* during basic endoscopic retrograde cholangiopancreatography (ERCP) procedures [74],

[75]. Biliary duct imaging with OCT was demonstrated by Arvanitakis et al., using specific criteria to detect malignant biliary strictures, with an accuracy of 84% in 37 patients [76]. OCT appeared promising in preoperative detection, compared to arbitrarily taken biopsies, with a 67% accuracy in the same cohort. Furthermore, Van Manen et al., assessed the accuracy of FF-OCT in distinguishing pancreatic tumors from surgical specimens and compiled specific criteria for different types of pancreatic tumors such as disruption of glands and the presence of tumor stroma [77]. (Figure 2.9). Zhu et al. checked the application of FF-OCT in hepatic specimens [52]. Regular hepatic structures, such as blood vessels and bile ducts could be very well distinguished and hepatic adenocarcinoma was identified by the presence of nuclear atypia and large tumor nodules separated by thick fibrous bands.

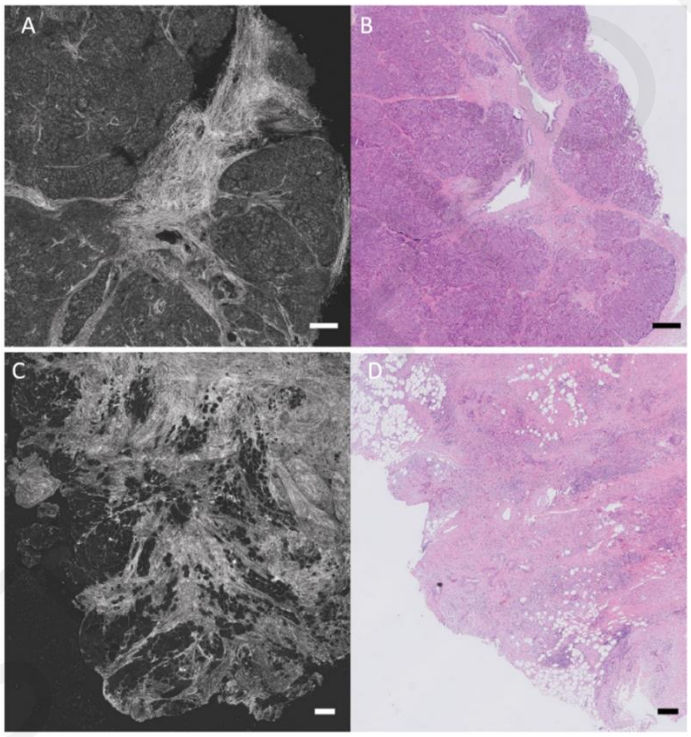

Figure 2.9. FF-OCT images of the pancreas. (A-B): FF-OCT image and corresponding hematoxylin and eosin (H&E) image of normal pancreatic tissue. (C-D): an example of an FF-OCT image of a moderately differentiated pancreatic adenocarcinoma with corresponding H&E image, showing tumor cells infiltrating into fat tissue (Bar = 250 μm). [77]

OCT has been also evaluated for the diagnosis of esophageal carcinomas, Barret's esophagus (BE), and dysplasia. Different characteristics of BE, dysplasia and adenocarcinoma, were evaluated, with promising results. However, discrimination between normal glands and BE and tumor glands was very challenging. Bouma et al., performed the first *in vivo* study with 32 patients, who underwent routine endoscopy, and exhibited some characteristics of BE [78]. OCT was also used for detection of BE before and after radiofrequency ablation therapy where OCT was found to distinguish normal glands from buried Barrett's glands only in a small percentage of the patients (7.7%) (Figure 2.10) [53],

[79]. Another study showed 81% sensitivity and 66% specificity in the detection of BE, indicating that OCT is presently not as accurate as histology [80]. OCT was further evaluated for the detection of esophageal dysplasia [81], [82]. Dysplasia was identified in OCT images based on reduced scattering and tissue structure changes, which are currently the only available criteria. Adenocarcinomas were also identified in OCT images with neoplastic epithelium containing large pockets of mucin surrounded by fibrotic and hypervascular tumor stroma. Occasionally, infiltration of heterogeneous structures into the muscular layers was mentioned as a feature of tumor invasion. Asymmetrical shape and crowding of submucosal glands was also indicating of the presence of adenocarcinoma (Figure 2.11) [80], [83]. Identification of adenocarcinoma, in patients who underwent upper GI endoscopy, at a recognition rate of 95% also showed promise [84].

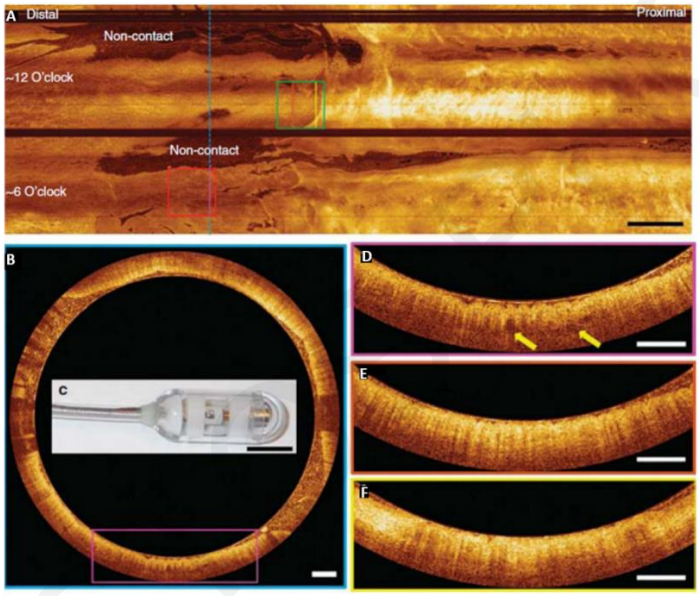

Figure 2.10. (A) *En face* OCT obtained below esophageal surface. Only the distal 12 cm out of 24 cm data is shown. (B) Representative cross-section (blue) from EMR region (red). (C). (D) Enlargement (pink) from (B) showing layer effacement, surface signal greater than subsurface, and multiple dilated glands (arrows). (E) Cross-section (brown) showing layered BE, which is likely non-dysplastic. (F) Cross-section (yellow) showing the squamo-columnar junction at a tongue of BE. Inset scale bars 1 mm. [53]

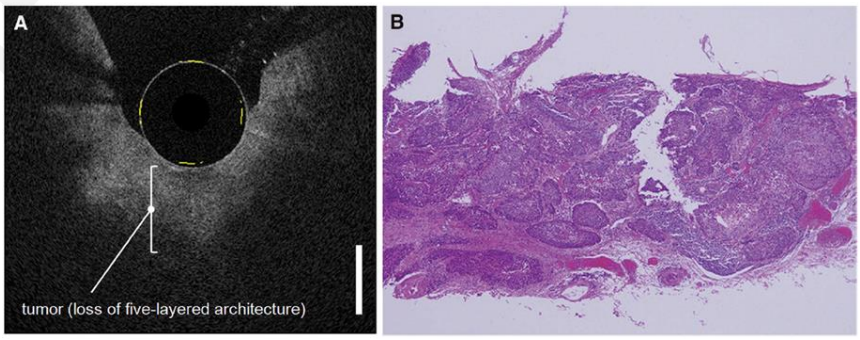

Figure 2.11. Example of endoscopic OCT of an esophageal squamous cell carcinoma. Corresponding OCT (A) and histology (B) image of tumor invasion in the submucosal layer, resulting in a loss of the five layered architecture (Bar = 1000 μm). Reprinted by permission from Elsevier: Gastrointestinal Endoscopy [85]

The application of OCT during colonoscopy for tumor recognition has not been often analyzed. Now, quantitative analysis could be achieved for both tumor and polyp detection; but unfortunately, the diagnostic accuracy has low sensitivity. Tearney et al., [86] first showed the application of OCT during colonoscopy for precancerous tissue identification and imaging of normal colonic wall features was also demonstrated by Westphal et al. [87]. For colorectal cancer, quantitative analysis was performed in two studies, concluding that abnormal malignant tissue has lower scattering properties and less variation of signal intensity from the surface, resulting in 78% sensitivity and 74% specificity [88], [89].

Other studies evaluated the diagnostic performance of OCT for the identification of cancer in bladder biopsies or surgical specimens in populations varying between 21 and 116 patients [90], [91], [92], [93]. Distorted tissue layers and sub-epithelial nests of tumor cells were mainly found in biopsies of tumors. By using these criteria, sensitivity and specificity ranged between 84 and 100%, and 65 and 89% respectively for tumor recognition. Using FF-OCT, more details of tumor cells, such as the existence of large nuclei and newly formed blood vessels (as bright spots) could be seen (Figure 2.12). With appropriate training of the reviewers, disease diagnosis could be obtained with an accuracy up to 96% [93].

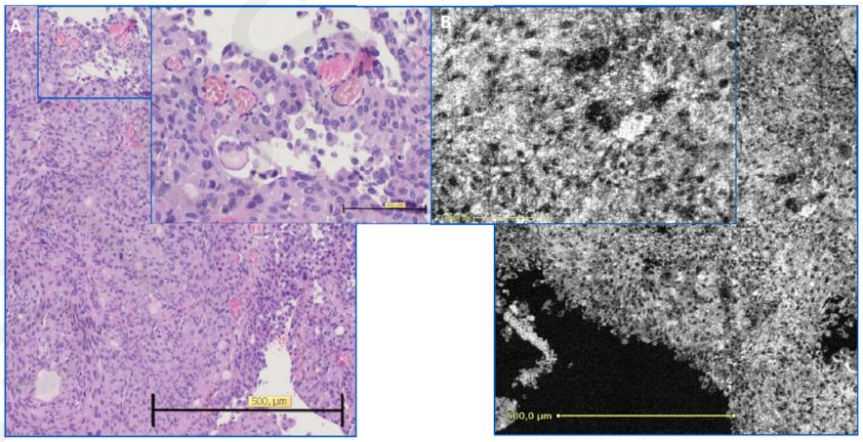

Figure 2.12. Hematoxylin and eosin stained histology section (A) and FFOCT images (B) of malignant features highlighted showing disorganized cells with large dark nuclei confirmed in histology as papillary carcinoma. [93].

CHAPTER 3

BACKGROUND

3.1 OCT and dispersion compensation

Group velocity dispersion (GVD) is a physical phenomenon that causes different wavelengths of light to travel at different velocities. When a light pulse with a broad spectrum enters a medium, different wavelengths are travelling at different velocities since there is a variation in the index of refraction with wavelength or frequency. There are many examples showing how the phenomenon of dispersion affects the performance of photonic devices from communication to biomedical imaging systems. In communication systems, second order dispersion leads to a broadening of the pulses used to represent digital information. The pulse broadening causes adjacent bits to overlap and results in intersymbol interference or cause resolution degradation in biomedical imaging systems [94]. In imaging systems such as OCT, dispersion mismatch between the interferometer arms, causes a broadening of the interferometric peak resulting in resolution degradation.

A feature unique to OCT is that the axial and lateral resolutions are decoupled, each being governed by separate optical phenomena. In the axial dimension the coherence length of the optical source and in the lateral dimension diffraction impose the physical resolution limits. In an OCT system, dispersion balance between reference and sample arms in the interferometer is necessary to produce the narrowest interferogram and, hence, resolution. For high axial resolution a larger source bandwidth is required and, as a result, the dispersion increases especially if not properly compensated. Therefore, the cross-correlation function becomes more broad and asymmetrical and the axial resolution worsens. With even more broad source bandwidths, dispersion compensation methods have become increasingly important for OCT.

Traditional methods rely on placing the right amount of dispersion balancing material in one interferometer arm of the OCT setup. To allow dispersion balancing, a fused-silica (FS) prism pair is inserted in the reference arm, with faces in contact and index matched, to form a variable-thickness window. The width of the cross-correlation function is minimized by translating the prisms along their touching faces. This simple adjustment compensates for

differences in fiber length, collimating lens, and microscope objectives between the interferometer arms. A uniform group-delay dispersion is assured by flattering the phase of the Fourier transform of the interference signal from a mirror in real time. To minimize higher order dispersion effects, FS prism pour is used to compensate for fiber-length differences and BK7 prisms to compensate for optical material mismatch in the interferometer. However, this method is usually practical only for up to second order dispersion [95].

Another way to compensate for dispersion mismatch is by using grating-based phase delay scanners. Using the rapid-scanning optical delay (RSOD), one can adjust dispersion by displacing the diffraction grating from the focal plane of the lens. The RSOD can compensate dispersion and achieve transform-limited interferogram profiles, to achieve the optimal fringe visibility and the highest possible axial resolution in OCT. Although previous studies showed promising results, attempts to compensate completely for the dispersion, by moving only the grating in the RSOD, were unsuccessful, possibly because of high-order dispersion. The incorporation of acousto-optical modulation (AOM) into the RSOD was reported to improve the performance of high-speed reference scan and OCT image fidelity [50].

In another approach, dual optical fiber stretchers were used for second order dispersion compensation with some degree of tunability [96]. In particular, it was demonstrated that two fiber stretchers, made of different fiber types and operated in parallel, compensated for a variable amount of chromatic dispersion while simultaneously allowing adjustment of the group delay between the two arms of the interferometer. The dispersion of a fiber of specific length and second-order dispersion coefficient changes upon elastic stretching. By using two fiber stretchers made up of different fiber types, an all-fiber tunable dispersion compensator was implemented in an OCT system in which the delay and the dispersion in the two arms of the interferometer could be adjusted independently. The setup was completely constructed from fiber elements and did not require any critical alignment, making it compact and versatile for use in *in vivo* experiments. The technique could similarly be used to compensate average sample dispersion and its use was not restricted to interferometer geometries, as the two stretchers could be used in sequence to adjust the dispersion and the group delay of a single piece of fiber, e.g., in telecommunication systems. It is, however, limited to the 2^{nd} order term and the remaining 3^{rd} order dispersion cannot be properly compensated by using only the two stretchers. These approaches require bulky

components and are difficult to adapt for depth-dependent compensation of sample dispersion.

A fiber-stretching-based dispersion compensator has also been combined with a grating based, scanning free, time domain OCT system to compensate for both second and third order dispersion, but the method increased the complexity [97]. The main advantage of the solution was its ability to independently compensate 2nd and 3rd order terms which are the predominant terms involved in OCT. Taking a closer look at the properties of this approach, it was hypothesized that the tunability of this method could also allow compensation of depth dependent dispersion in the sample, in a continuous manner. This could be a kind of adjustable depth dependent dispersion compensator if coupled to the fact that real time A-scans were obtained with a scan free system.

Another approach revisits the problem of numerical dispersion compensation with the use of the fractional Fourier transform (FrFT) [98]. The fractional Fourier transform (FrFT) is a generalization of the traditional Fourier transform and can be seen as a tool to visualize the physics behind dispersion compensation. By using the FrFT one obtains depth information in FD-OCT while, simultaneously, numerically compensating for group velocity dispersion. The technique was successfully demonstrated on a biological sample. Furthermore, it provided new insights on the tissue depth-dependent dispersion. Simulations have shown that both normal and anomalous sample dispersion can be addressed by dynamically adapting the order parameter as a function of depth. This method can be seen as analogous to a “short time” FrFT but is more efficient and intuitive and may even be applicable to samples without isolated scatterers. From the optimized FrFT order parameter one can also readily obtain some information about the amount of dispersion in an OCT configuration and sample. The relationship between the FrFT order parameter and group velocity dispersion was derived and used to successfully measure the group velocity dispersion coefficient of distilled water and some single mode fibers.

3.2 OCT and tissue dispersion

While an OCT interferometer can be optimized for its intended purpose, dispersion differences will still emerge due to the variability and diversity of the properties of the tissues that are imaged. Interestingly, since dispersion is specific to the tissue that is causing the effect, it can carry useful information regarding its composition and/or constituent concentrations. OCT technology has significantly improved over the past few years with the

introduction of high resolution systems which are well suited for *in vivo* applications. However, many disease changes, such as those associated with early stage cancer, are in the micron and sub-micron range, remaining below the resolution limit for detection. Tissue dispersion can, therefore, play an important diagnostic role as a biomarker of disease.

The concept of exploiting dispersion as a source of contrast is not new since there have already been examples of using the dispersion of biomolecules to quantify their concentration. For example, the dispersion of hemoglobin was used to extract the concentration of hemoglobin (Hb) in intact red blood cell (RBC) [99]. It provides a simple and practical method, using spectroscopic phase imaging, to simultaneously measure Hb concentration and cell volume of living RBCs. As demonstrated, dispersion provides molecular specificity and quantitative phase maps at different wavelengths can help differentiate among molecules. The relation between dispersion and biochemical composition was further exemplified using quantitative dispersion microscopy, which has confirmed that the dispersion of live HeLa cells agrees well with the dispersion measured for pure proteins solutions [100]. Variations in the dispersion of different types of normal skin have also been identified *in vivo* with coherent reflection measurements of different skin types [101]. Given the dramatic changes in cellular biochemistry caused by cancer [102], which are discernible by other optical techniques such as Raman spectroscopy [103], it is highly likely that dispersion can also be used as a contrast mechanism in OCT imaging. Therefore, Group Velocity Dispersion (GVD) could be used to detect, for example, changes associated with early cancer and result in more accurate disease diagnosis.

3.2.1 Methods of measuring group velocity dispersion (GVD)

Three main methods are described in literature for estimating the dispersion from OCT images: (i) measuring the resolution degradation [104], [105], (ii) measuring the shift (walk-off) between images taken at different center wavelengths [106], [107] and (iii) calculating the second derivative of the phase of the spectrum [108], [109]. However, these methods require that a strong, distinct, reflector is present in the image which is rarely the case in living tissue. In addition, the presence of Mie scattering and speckle can be detrimental to the attempt to measure dispersion. Each of these methods were evaluated, for the purposes of this thesis, with images from samples with different scattering properties as well as tissue images (*ex vivo*).

Point spread function (PSF) degradation method

The most straight-forward method to estimate the dispersion is by measuring the broadening of a single reflection's Gaussian envelope (Figure 3.1).

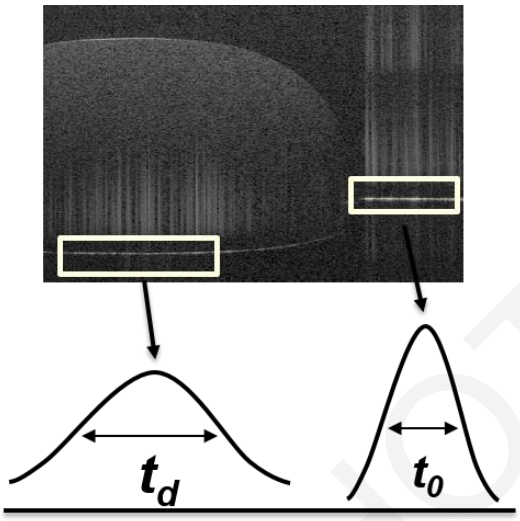

Figure 3.1. OCT image of collagen gel. Dispersion causes broadening of the pulse width (t_d) the can be estimated using the bottom surface of the sample. The reflector line can be used for the estimation of the original pulse width (t_0).

If the original signal has an interferogram width of t_0, the degraded interferogram will have a broader width, t_d, and the two will be related by

$$t_d^2 = t_0^2\left[1+\left(L\cdot GVD\cdot t_0^{-2}\right)^2\right] \qquad (3.1)$$

where L is the sample thickness and GVD is the Group Velocity Dispersion [104], [105]. Thus, the GVD can be estimated by:

$$GVD = \sqrt{\left(t_d^2 t_0^2 - t_0^4\right)L^{-2}} \qquad (3.2)$$

In an OCT image, the effects of dispersion are observed as a broadening of the Point Spread Function (*psf*) and, therefore, as a degradation of the resolution. The system resolution, d_0, is defined as the full-width-at-half-maximum (FWHM) of the coherence envelope of a point reflector and is related to the interferogram width, t_0, by

$$t_0 = d_0 \Big/ \left(c\sqrt{4\ln(2)}\right) \qquad (3.3)$$

where c is the speed of light. The same also holds for d_d and t_d, the dispersion-degraded widths. Since the values of d_0 and d_d can be readily measured using OCT, the GVD can be estimated from an OCT image as long as there are distinct point reflectors below and outside the sample. Although this can be arranged *ex vivo* [110], it is rarely the case *in vivo*.

Walk-off method

Dispersion causes each wavelength to travel at different phase velocity. This is due to index of refraction variations and causes different wavelengths to be subjected to varying path length. The result is in an apparent shift in the OCT images at different wavelengths, called a walk-off (Figure 3.2).

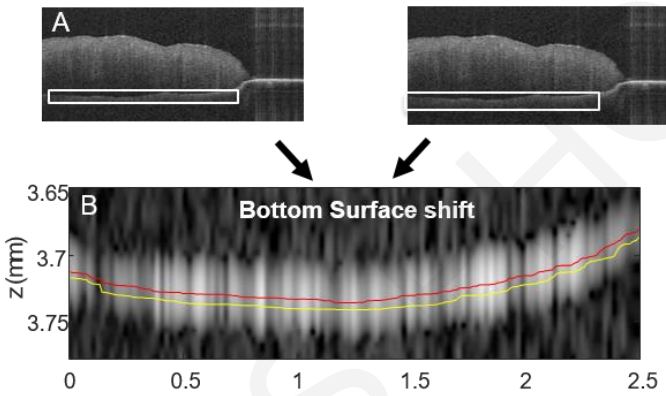

Figure 3.2. Adipose tissue images acquired using OCT at different central wavelengths of the spectrum (A).The comparison between the bottom surfaces of the images shows an image shift that is used to estimate the GVD (B).

Envelope broadening of the optical pulses can be written as $GVD = \frac{1}{c}\frac{\Delta n}{\Delta \omega}$ where c is the speed of light, n the index of refraction and ω the optical frequency. A dispersion measurement can be obtained from path length measurement through the material of interest. In OCT we aim to identify sample areas on a micrometer scale. This requires a sufficiently broad spectrum to obtain a measurable change in accumulated optical path length. The differential walk-off Δz is evaluated between two spectrally separated independent source spectral as a function of index of refraction, $\Delta n = \frac{\Delta z}{L}$, where L is the sample thickness. Thus, the group velocity dispersion can be written as:

$$GVD = \frac{\Delta z}{cL\Delta\omega} \tag{3. 4}$$

Note that $\omega = 2\pi f = \frac{2\pi c}{\lambda} \Rightarrow \Delta\omega = \frac{2\pi c \Delta\lambda}{\lambda_0^2}$ and so,

$$GVD = \frac{\Delta z \lambda_0^2}{2\pi c^2 L \Delta\lambda} \tag{3. 5}$$

where Δz is the differential walk-off between two sources, $\Delta\lambda$ the source bandwidth and L is the sample thickness [106], [107] .

Phase difference method

In spectral interferometry, the dispersion parameter can be obtained from the interference spectrum produced by two time delayed beams. Two beams from the two arms of the interferometer interfere and a spectral interferogram is produced. The spectrum produced for a given time or phase delay is given by (Figure 3.3):

$$I(\omega) = |E_0(\omega)|^2 + |E(\omega)|^2 + f(\omega)\exp(i\omega\tau) + f^*(\omega)\exp(-i\omega\tau) \tag{3. 6}$$

The delay is due to index of refraction variations and appears as a phase shift between different wavelengths. Hence, the GVD can be estimated from the phase changes of the spectrum of the OCT signals.

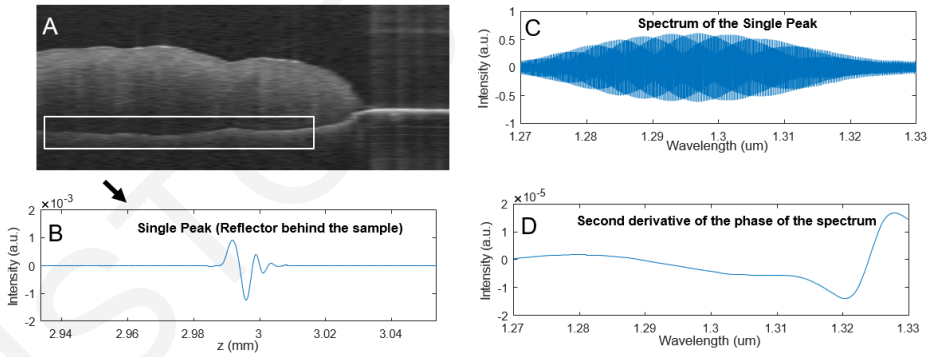

Figure 3.3. Using an adipose tissue OCT image a single peak is isolated from the bottom surface (A), (B).To take advantage of the phase changes the spectrum of the peak in (C) is used to calculate the second derivate of the spectrum and estimate the GVD (D).

Note that $f(\omega) = \Im\{f(t)\} = |E_0^*(\omega)E(\omega)|\exp(i\Delta\varphi(\omega))$ includes the phase information on the spectral phase difference as $\Delta\varphi(\omega) = \arg[f(\omega)]$. To derive the phase difference $\Delta\varphi(\omega)$, the inverse Fourier transform(FT) of $I(\omega)$ is performed and the following is obtained:

$$\Im^{-1}(I(\omega)) = E_0^*(-t) \otimes E_0(t) + E^*(-t) \otimes E(t) + f(t-\tau) + f(-t-\tau)^* \tag{3. 7}$$

Then a FT is applied to the component $f(t-\tau)$ to transfer it back to the spectral domain and the complex amplitude becomes:

$$f(\omega) = |E_0(\omega)||E(\omega)|\exp(i\Delta\varphi(\omega) + \omega\tau) \tag{3. 8}$$

The phase of this complex amplitude minus the linear part $\omega\tau$ that is due to the delay yields the spectral phase difference between the two beams. Finally, from phase-frequency plot the first derivative leads to group delay and the finally the group velocity dispersion is given by the second derivative of the spectrum phase as [108], [109]:

$$GVD(\omega) = -\frac{1}{L}\frac{\partial^2(\Delta\varphi)}{\partial^2(\omega)} \tag{3. 9}$$

3.3 Index of refraction as a diagnostic tool

The index of refraction (*n*) determines how fast the light propagates through a medium and can be calculated by the division of the speed of light, (*c*), and the speed of light, (*v*), as it propagates through a medium. Note that *n* is always greater than one. The use of index of refraction, as an important intrinsic biomarker has been explored recently.

All materials have unique *n* value, which is associated with the electrical permittivities. Classic phase contrast or differential interference microscopy use *n* values as an optical imaging contrast. However, they do not provide a detailed mapping of *n* distributions in tissue samples, but are rather limited to thin slices from the samples that are fixed on slides or cell cultrures. Recently, there has been an escalating interests in measuring 3D *n* distributions for various applications in bioimaging. Mainly because *n*, as an intrinsic optical parameter, provides the possibility for label-free cell imaging with the added advantage of giving a quantitative information about the sample.

Recent studies have shown that the tissue index of refraction distribution could be used as a biomarker for medical diagnosis. Microbiology studies show that *n* distribution can provide valuable information about cellular growth and division and bacteria identification. Past studies have reported that 3D *n* tomograms of individual bacteria can be measured using holotomography (HT), a technology that directly provides the measurements of the 3-D *n* distribution of a cell. Using a Mach–Zehnder interferometer and illumination scanning, 3-D *n* tomograms of bacteria, extracted from a sample of *E. coli*, have been demonstrated [111]. Recently, white-light diffraction tomography was utilized to image 3-D *n* tomogram of *E. coli* [112]. Furthermore, 3-D *n* distributions of a magnetostatic bacterium which produces magnetic particles (magnetosome), were measured [113]. In addition, *n* information can be exploited to retrieve cellular dry mass and concentration information about individual bacteria. Dry mass refers to the non-aqueous contents inside cells and can be used as a marker of cellular growth and division. It can be simply retrieved

by calculating 2-D optical phase delay maps and averaging over cell area since the optical phase delay map of a cell corresponds to the integration of *n* differences between the non-aqueous contents inside cells [114].

In hematology, different types of cells were identified by their *n* value. Blood borne infectious diseases (malaria) or chronic human disease (sickle cell anemia, diabetes mellitus) could be identified by *n* distribution. In addition, the use of 3D *n* tomography in the field of hematology allowed the simultaneous measurement of various optical parameters of individual red blood cells such as volume, surface area, sphericity, Hb content concentration, and membrane fluctuations that differ from reference values in case of disease [115], [116], [117].

Imaging of hepatocytes has played an important role in hepatology. The structure of hepatocytes is clearly associated with liver diseases and can be identified using their *n* value. Among subcellular structures of hepatocytes, lipid droplets (LDs) are very important because they are directly related to the lipid metabolism. LDs consist of a monolayer of phospholipids and associated proteins surrounding a core of neutral lipid and are ubiquitous intracellular organelles storing and supplying lipids in most cell types as well as hepatocytes [118]. Recent studies suggest that LDs participate in various pathological roles, such as cancer and diabetes mellitus, and exhibit 3-D motions to regulate lipid storage and metabolism [119]. LDs can be effectively visualized exploiting their *n* value. The index of lipid is significantly higher than protein [120] and thus LDs can be identified by performing 3-D *n* tomograms. However, the detailed process of LD dynamics, including biogenesis, growth and 3-D subcellular motions, are incompletely represented [121].

Cancer studies have shown that the presence of cancerous cells can be identified by different values of *n* distributions and can be indicative of breast, prostate and epithelial cancer [122], [123], [124]. Recently, label-free tissue imaging, utilizing *n* information, was adapted to neuroscience. Index of refraction distributions could be helpful for the diagnosis of serious neurological situations such as Alzheimer's [125] and Parkinson's diseases [126].

However, there are some limitations when *n* distributions are used for medical diagnosis. First, it is difficult to relate *n* to molecular information. This is mainly because proteins have similar *n* values regardless of their type. Another problem is that the distribution of *n* values can provide limited morphological information about tissue

structure. Also cells have refractive indices similar to their environment and this can result in significant errors.

3.4 Methods of estimating *n* distributions

3.4.1 Bulk optical methods

Various methods for the measurement of *n* are available for many materials and tissues. The majority of these techniques are based on Snell's law (total internal reflection and Brewster's angle) and wave interference. They employ experimental setups using prisms and different types of interferometric techniques such as Michelson's or Fabry-Perot interferometers [127]. The indices of refraction of a material can be measured very precisely using prism cut-outs of the material [128], [129]. The refractive index is calculated by estimating the incident angle at which total internal reflection of the prism base breaks. The main limitation of this method is that it requires prism shaped samples and is not suitable for routine measurements.

3.4.2 Interferometric methods

Interference methods are also used for index of refraction measurement using a Michelson or a Fabry-Perot interferometer [130], [131]. These methods utilize wave interference and produce a fringe pattern from the backscattered intensity of the light as it propagates through the sample. Although these methods are usually employed to detect very small relative phase differences, they were extended to measure absolute *n* values. In the Michelson Interferometer (MI) method, a sample is placed in one of the two arms of the interferometer continuously changing the optical path length difference, and hence producing a fringe pattern (with respect to the angle of incidence). From this pattern, and knowing the sample thickness, *n* can be easily determined with the accuracy of mm, the error arising mainly from the sample thickness measurement, because the *n* and the thickness cannot be independently determined from a single fringe pattern.

The Fabry Perot (FP) method is another interferometric technique used. In this case, the fringe pattern is determined solely by the phase difference between the directly transmitted light wave and the collinearly propagating waves, therefore the FP fringe pattern is more stable against environmental perturbations than the MI fringes. However, in both methods, the thickness measurement limits the accuracy of the *n* determination [131].

3.4.3 Immersion methods

Immersion Spectroscopic Reflectometry (ISR) was first developed to calculate the *n* and thickness of a transparent thin film [132] but was later applied to systems up to three layers. The technique's basis was presented by Ellis in 1963 for estimating only the *n* of one layer thin films [133]. Ohlidal in 1980 developed it into a method for determining the index of refraction and thickness of thin films that was precise when assessing systems with more than three layers if the substrate index of refraction was known. If the environment medium in ISR is liquid, the method is called liquid immersion spectroscopic reflectometry (LISR) or solid immersion spectroscopic reflectometry (SISR) in case the environment medium is solid. The main goal is to extract the optical properties from the spectral response changes by varying the environment around a slab of material. LISR requires different non-absorbing media with known indices to change the spectral response of the sample while in SISR, a film with known *n* but with changing thicknesses is used to obtain various spectral responses. SISR was based on a previous method, created by Fränz in the 70's, which acquired the same information by gradually etching the film thickness. Moreover, double-immersion spectroscopic reflectometry (DISR) was also developed for three layer systems. DISR is based on evaluating four spectral reflectances, utilizing all possible combinations of refractive indices of two different transparent environment media and two different non-absorbent substrates [134].

The immersion technique is based on the fact that for a two layer system, when the *n* of the medium is the same with the *n* of the film, the effect of the first layer can be removed away and the reflectance of the system matches the reflectance of the system immersed in a medium of different *n*. So, the problem of finding the optical parameters of a two-layer system could be reduced to examining a single layer problem. For a non-absorbing double layer formed on a non-absorbing substrate with known *n*, the indices of the layers can be obtained from the odd order of the reflectance spectrum oscillations. The same procedure is also used for SISR. This method was used to analyze non-absorbing single layer of silicon nitride, non-absorbing double layers of silicon dioxide, and silicon nitride thin films by measuring the spectral reflectance in air and in water. DISR was used for triple layers formed by titanium dioxide and silicon dioxide films placed on glass [132].

3.4.4 Confocal microscopy method

A confocal microscopy technique (dual beam) using a single wavelength source was also proposed for the simultaneous measurement of thickness and refractive index of a stepped sample (thickness changing through the sample) [135]. In this method the incident polarized beam (45 degrees) was divided using a Nomarski prism in front of the scanning objective lens. The prism created two closely spaced lateral confocal gates for the two orthogonal polarization states of the laser beam. Each channel pointed to two close lateral regions of the object with different unknown thickness and the intensity of each channel detected separately. The index of refraction of the object could be estimated from measuring the travelled distances of the scanning objective lens to the front and rear surfaces of the object for each channel. This method could not be applied to flat surface samples since the required two channels would not be present. The experimental validation was done using a microscope cover glass, with thickness ranging between 165 and 175 μm and with a refractive index of 1.525.

3.5 Index of refraction measurement in OCT

By using Low Coherence Interferometry (LCI) or OCT, multiple layers can be identified in terms of optical thickness, the geometric thickness multiplied by the refractive index [136]. Several methods have been developed to estimate the index of refraction and thicknesses in the optical thickness measurements.

3.5.1 OCT imaging method

Tearney et al, in 1995 proposed an *in vitro* method that exploits the ability of OCT to measure the optical path length of excised tissue specimens. It determines the index of refraction of a sample by placing it on top of a planar reflecting surface to acquiring an OCT image (Figure 3.4). The thickness of the sample, *z*, can be determined by subtraction the axial position of the reflector outside the tissue from the axial position of the tissue surface in the OCT image. The additional optical path length delay *z´* can be measured by subtraction of the axial position of the reflector outside the tissue from the axial position of the reflector imaged through the tissue. Finally, the refractive index of the sample can be defined as:

$$n = \frac{L + L'}{L} \qquad (3.\ 10)$$

Although the method comparing physical and optical path lengths is necessarily invasive, it can therefore be used to determine the refractive indices of many different sample types. In that study, they determined the refractive indices of BK7 and fused silica (1.515 ± 0.01, 1.458 ± 0.018) and also of human tissue (stratum corneum, 1.51 ± 0.02, and epidermis, 1.34 ± 0.01).The main limitation of the method is that it cannot be used for *in vivo* measurement as it requires a reflector under the tissue [110].

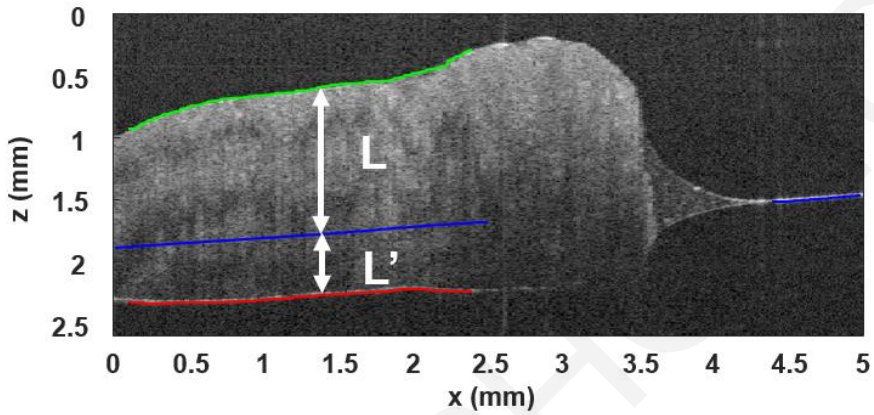

Figure 3.4. OCT image of adipose tissue placed on an unpolished metal substrate. The two vertical bars represent *L, L'*, from top to bottom.

3.5.2 Focus Tracking Methods

These methods combine the concepts of a confocal microscope and LCI to decouple the estimations of distance and index of refraction. In these techniques, the focal point of the sample arm beam is scanned through the sample from the top surface to the bottom surface either by displacing the sample stage or by displacing the focusing lens. The physical location of the light beam focus is taken from the confocal signal and the change of phase information is extracted by utilising the scanning reference arm. These method allow the measurement of both the phase and group refractive index (n_g and n_p) of the sample at each point. The measurement accuracy is low due to the resolution of the translation stages moving the focal point or the sample.

Ohmi *et al*, in 1997, performed measurements on z-cut sapphire and glass plates nearly one mm thick and on a plate nearly 0.5mm thick. By moving the object and scanning through the sample they estimated an index of refraction accuracy of ≤ 0.3% [137]. Also, in another study by the same group in 2000 [138], they used biological samples of animal tissue, human tooth and nail with sample thicknesses ranging from 150μm to 550μm and resulting in refractive index measurements ranging from 1.37 to 1.65 and an accuracy of ± 1% (assuming that the index of refraction was homogeneous through the sample thickness).

Furthermore, in the same study the technique was utilized on a more challenging two-layer sample. The first layer was a piece of crab-leg crust, which consisted of a white viscous layer, and the second was a semitransparent carapace. They managed to report separated measurements for each layer (1.375 and 1.411) with an accuracy of ±1%.

Confocal scanning has also been utilized and evaluated in combination with FD-OCT. In this scenario, optical thicknesses was estimated from the Fourier transform of the spectral data. Both the index of refraction and thickness could be calculated by moving the objective lens to focus on the top and bottom surface of a single layer object. This experimental procedure was implemented on water, air and oil solutions inside a 250μm deep container and the results followed the reference values within 0-1% error [139].

When applying focus tracking, it is important to note that if the phase and group index of the object are not the same, another piece of information is required to calculate the three parameters (phase and group index, thickness). The additional information could be the light pulse dispersion relation or quantification of the thickness by another technique. One approach [140] was to place the sample between two reference glass plates with known separation. Then, by estimating the gaps between the sample and the glass plates, the single layer thickness could be calculated independently. For the experimental verification of this procedure, materials such as sapphire, electro optic crystals, fused quartz, flint glass and crown glass were used. The measurements resulted in phase and group refractive indices estimations with an error of 0.3% or less. The index of refraction range was 1.45 to 2.25 and the thickness range between 0.5mm to 1mm. Similarly, experiments were performed with FD-OCT systems [141]. For these experiments, the samples were Glass slide, BK7, Fused Silica with thickness about 1000 μm and in addition, they also used a slab of ITO glass with thickness about 700μm. The resulting estimates exhibited an error of about $7x10^{-4}$ for both the index and the thickness. There are, however, occasions when using this method is not practical since the sample must be placed in a special holder before the procedure. Therefore, in such cases, if possible, it is useful to take an expression of the chromatic dispersion of the under plate index. One approach of getting this dispersion information is to repeat the measurement with two or more different central wavelength sources for a single layer object [142]. This method was assessed experimentally for materials such as BK7, B270, CaF2, Silica, cover glass, and C.C film with wide range of thicknesses between 0.023-5.2mm and group and phase indices ranging between 1.43-1.53. The reported average measurement errors were about %0.061 for the geometrical thickness, %0.066 for the phase index, and %0.057 for the group index.

In the early 2000's, Maruyama *et al* proposed a new expression of the chromatic dispersion in terms of the phase index and showed that the phase and group refractive index and physical thickness of a single layer sample can be estimated without using a special sample holder [143]. The materials for the experiments were single layer samples like z-cut sapphire, x-cut $LiNbO_3$ and z-cut $LiTaO_3$, and Poly-viny-lchloride plates. The indices ranged between 1.45 and 2.17 and the measured estimates resulted in accuracies of 0.3% or better. In addition, a different study with similar measurements using this approach, on a 500μm thick fused-quartz plate and a 125μm thick z-cut $LiNbO_3$ plate, reported an accuracy of 0.3% or better [144]. In addition, in this work, a multi point estimation of a radial-graded-index rod lens was reported to give an approximation of the index gradient distribution.

Another work assessed the applicability of the focus scanning method using multi-layer systems, for both the object and the lens scanning methods, developing a generalized formula for the estimations. The technique utilized a pile of cover slips sample made of 13 layers of glass and air [145]. Even though the layers were detected using the proposed method, there was no quantitative information about the accuracy of the measured index of refraction or thicknesses in the conclusions.

Bifocal optical coherence refractometry (BOCR) was proposed by Alexandrov in 2003 [146]. That technique was based on the simultaneous sample image formation of two accurately spaced confocal gates by using two lenses in the sample arm beam with different focal lengths such that two axially separated focal points were formed. The optical path length change between the gates was measured using the principles of LCI and was used for the calculation of the index of refraction. In another implementation of this technique, the two confocal gates were formed using an adaptive liquid-crystal lens [147]. The experimental measurements reported an *in vivo* measurement of the refractive index of the stratum corneum of skin on the dorsal surface of a human thumb. The index of refraction was 1.50 with a deviation of ±0.02.

In another implementation of focus tracking, the sample was moved toward the objective lens with a defocus occurring at the image plane. The objective lens was then displaced to compensate the amount of defocus and extract the optical path changes. Recently, Min *et al*, suggested numerically shifting the image plane to find the focusing position instead of moving the objective, something that appeared to also be also applicable to multilayer systems [148]. They used various combinations of fused silica and BK7 glass for their experimental procedure and estimated the indices of the two layers with thicknesses

from 0.15 to 1.5 μm. The mean error of the resulted indices of layers 1 and 2 was 0.062% and 0.128% respectively. For thickness measurements, the mean error was 0.180% and 1.394%. Finally, for multilayer samples, various combinations of plates and films, of various thicknesses were stack, on a 0.153 mm thick oil layer. The index of refraction and thickness of the oil layer were estimated with a mean error of 0.065% and 0.990%.

3.5.3 Interferometric Methods

The index of refraction can also be estimated by inserting the object into a Michelson interferometer. Fochs in 1950, [149], reported the first study of this type by using a white light Michelson interferometer and a spectrometer to record the spectral response pattern. The measurements were taken: (i) without a sample, (ii) with the sample placed normally in the interferometer and finally (iii) in the presence of the sample but with the interferometer mirrors covered. The measured thickness of a mica specimen was 12.19 with a deviation of ± 0.02μm, and for the index 1,601 with a deviation of ± 0,03. Jin *et al*, in 2010 also used a Michelson interferometer to measure the index of refraction and the sample thickness of a single slab while the slab was partially inserted in the sample arm of the interferometer [150]. The resulting spectral response was a mixed pattern of the beam travelling in free space and the beam that passes through the sample. The optical thickness of the object, placed in the sample arm, was estimated from the Fourier transform of the spectral response of the perturbed beam. The experimental results for a double-sided polished Silicon wafer were 334.85μm for the thickness and 3.5 for the index with deviations of 0.49 μm 0.004 and respectively. Following the same experimental approach, Cheng *et al* in 2010 used an OCT system with two reference arms and one sample arm [151]. First, the optical path difference between the sample arm and the reference arms was fixed without a sample. Then the sample was placed in the sample arm and the first reference arm was displaced in order to receive interference patterns when the signals of the two arms mixed while the other reference arm was not moved. The experiment was performed on a BK7 glass sample with an index of refraction of 1.501 (group) and thickness of 0.71mm and on B270 Glass with index of refraction 1.52 and thickness 2.0mm. The mean experimental errors were 3.81% and 1.1% respectively.

In another study, both thickness and group index of refraction estimations were estimated using low coherence reflectometry with a setup comparable to an OCT system [152]. A reflecting mirror was fixed in the sample arm at a known position in front of the sample and the surfaces of both the mirror and the sample were detected by scanning the

reference mirror. The index of refraction and the thickness could be estimated by using the optical path displacement of the detected reflecting mirror position when the sample was placed in the sample arm. The method was used to estimate the sample thickness and index of refraction of a piece of Tygon tubing and resulted in 6.753mm and 1.511 with a deviation of ± 0.004 and ± 0.001 respectively. In addition, the method was applied to two fused silica samples (thickness 9mm and 12mm) and the resulted index was 1.46 with an uncertainty of $6x10^{-4}$. In another study, the combination of LCI with a reflector plate and a moving reference arm was used for measuring poly-methyl-methacrylate glass (PMMA) with a thickness of 1.9 mm and an index of 1.66 with an accuracy of 0.04% [153]. In yet another application of this method, Na *et al* in 2009 used an FD-OCT system and measured a 1.555 mm thick fused silica plate with the results showing a standard deviation of $\pm 2x10^{-4}$ for both thickness and the index of refraction. This method was also utilized to estimate the index and thickness of a glass plate by both TD-OCT and FD-OCT systems. The results showed mean errors for index of refraction and thickness in TD-OCT of 1.74% and 1.65% respectively while the mean error using FD-OCT was reduced to 0.03% and 0.26% [154].

A FD-OCT system was employed to measure the index of refraction of a stepped layer of SiO_2 thin-film deposited on a silicon substrate with thicknesses ranging from 0.5 to 4.0 μm [155]. The index of the film layer was estimated with an accuracy of μm without prior reference of the geometrical properties. Park *et al* in 2011 reported a simultaneous measurement of sample thickness and group index of refraction based with spectral domain optical LCI with two sample probes facing each other that was applicable for transparent as well as absorptive or opaque samples [156]. The optical thickness extracted (after applying the Fourier transformation on the interference spectrum) by each probe made it possible to estimate the index of refraction and the physical sample thickness. The resulting measurements for the thickness had values from 0.15 mm to 3 mm with indices around 1.5 (Cover glass, BK7, Silica, CaF2, NG9). The mean error for the group index of refraction and sample thickness was 0.06%.

Finally, a Tandem interferometer (composed of a Michelson and a Fizeau interferometer) has also been used to estimate the index of refraction and thickness of single layer objects. This method is not affected by group delay dispersion and can be used with thick samples and broad source spectral line widths. Experimentally, three BK7 glass plates were tested, about 100, 150, and 300μm thick, which were placed in the interferometer arm. The resulting index of refraction exhibited a $7x10^{-4}$ difference from the reference value [157]. In another application of this method, without employing compensators, the indices

of BK7 glass plates with thicknesses 10,1mm and 3.5mm were estimated with a difference from the reference value of 1.85×10^{-4} and a standard deviation of 5.1×10^{-6} [158].

3.6 Scatterer size estimation using OCT images

Spectral variations are related to scatterer size by Mie theory and have already been used in many OCT studies as a contrast enhancement mechanism. Various researchers have tried to estimate the size of epithelial cell nuclei using Light Scattering Spectroscopy (LSS) [159], [160]. Recently, LSS has been combined with low-coherence interferometry (LCI), providing depth localization of the LSS signal [161], [162]. OCT has also been proposed as for spectroscopic, depth-resolved, imaging. Spectroscopic OCT (SOCT) operates on the localized spectra that are inherently available in the OCT signal [163]. In order to take advantage of the SOCT capabilities, there has been great effort to find spectroscopic metrics that could precisely measure the size of cell nuclei, the main scatterer in epithelial tissues.

The majority of the methods reported so far have been based on the hypothesis that epithelial cell nuclei can be considered as spheroidal scatterers whose interactions with light are described by Mie theory [120]. An approach to get their nuclear size is to curve-fit the backscattered spectra, extracted from the OCT or LCI signal, to the theoretical prediction curves [164]. The main limitation of this approach is that it requires an exhaustive search through many possible scattering sizes and precise knowledge of the index of refraction of the scatterer and the ambient medium [165]. Furthermore, it does not sufficiently account for the spectral changes that could appear in the experimental measurements if the incident beam waist spot size is small, or similar to the wavelength size and that Mie theory was not created for Gaussian beams but mainly for plane waves [166]. Many studies using Mie theory have been based on the observation that the oscillation “frequency” increases with the particle size. Some pre-processing of the backscattered spectrum followed by a Fourier transform was recommended by Wax et al, [162]. The position of the maximum of this function is indicative the dominant scattering features in the region under observation. This technique, with various studies on phantoms and biological tissues that followed, resulted in very good calculations of the scatterer sizes [162], [165], [167]. However, when the spectrum of light source is narrow, it does not provide a sufficient number of oscillations in the backscattered spectrum and becomes challenging to extract the maximum peak from other, low-frequency, components [168]. Another approach for measuring the scatterer size, reported by Adler *et al*, was based on estimating the autocorrelation width of the backscattered spectrum [169]. It relied on the observation that backscattered spectra with

high spectral modulation give autocorrelation functions that shift quickly away from the central point while the autocorrelation function of spectra with low spectral modulation is broader. Utilizing this information, the contrast of OCT images was enhanced. The main advantage of this spectroscopic analysis method is that it does not rely on the distribution of optical power over absolute wavelength and therefore it is not sensitive to many sources of spectroscopic noise. Still, it does not always result in a precise estimation of the scatterer size.

Variations of the above methods were implemented in other studies. Oldenburg *et al*, utilized the autocorrelation width of backscattered spectra, at 80% of the peak value, in order to improve the contrast of OCT images of macrophages and fibroblasts [168], while Kartakoullis et al., and Jaedicke et al., used the spectral information with principal component analysis (PCA) and clustering algorithms in an effort to discriminate phantom samples of microspheres with various diameters [170], [171]. Tay *et al* proposed that the use of many distinct bandwidths could enhance the sensitivity of scatterer size estimates, applying the method in spectroscopic OCT images of solutions of 0.5 and 45 μm microspheres which could be clearly discriminated [172].

3.6.1 Correlation of the derivative method

Kasinopoulos et al., used Mie theory to create a new metric for SOCT, the bandwidth of the correlation of the derivative (COD) bandwidth [173]. The feasibility, accuracy and robustness of this new method, in estimating scatterer size, has been confirmed utilizing images from microsphere phantoms and human gastrointestinal normal and cancerous tissue. The concept behind this approach is presented in Figure 3.5 where the backscattered spectra for 6.0, 10.0 and 16.0 μm diameter scatterers in the wavelength range of the laboratory SS-OCT system are presented. The characteristic oscillations are easily distinguishable in the spectra. The COD bandwidth method estimates the scatterer size by the extraction of the first derivative of the spectrum followed by the calculation of its autocorrelation. After the calculation of the autocorrelation, the lag position of the first minimum at the graph is used as a metric for scatterer size estimation and is referred to as the bandwidth of the Correlation of the Derivative (COD) bandwidth. Figure 3.5(D)-1(F) illustrate the COD function for the case of 6, 10 and 16 μm diameter scatterers. The red arrows indicate the COD bandwidth. The utilization of the derivative, before calculating the autocorrelation, is important to give more emphasis on the oscillations of the spectrum, since the derivative is self normalizing and eliminates big differences in the peak intensities of the spectrum.

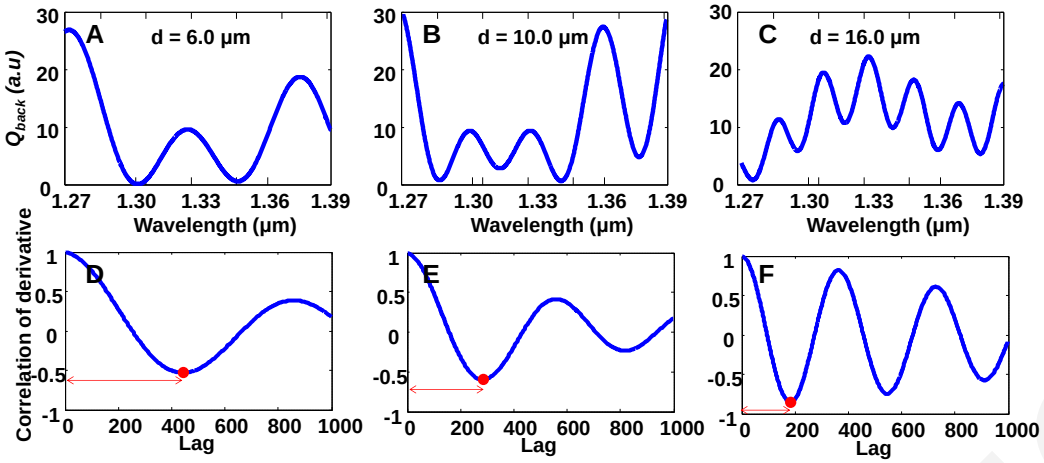

Figure 3.5. Backscattering Mie Spectra for (A) 6 μm, (B) 10 μm and (C) 16 μm scatterers with medium and sphere refractive indices set at 1.47 and 1.59 respectively. The parameters for the calculations were chosen according to the specifications of the light source and the microsphere samples used in the experiments. Graphs D-F show the Correlation of the Derivative (COD) with the red dot indicating the first minimum and the red arrow indicating the bandwidth of the COD [173].

Mie theory can be used to derive the relationship between the scatterer size and the COD bandwidth. The Mie-derived curve (Figure 3.6, blue line) exhibits a strong and nearly monotonic relationship between the two parameters for diameters larger than 4 μm. Therefore, this relationship can be used to estimate the scatterer size from the COD bandwidth of an OCT spectroscopic image. However, reliable scatterer estimates using the proposed method can only be performed for scatterers above 4 μm (e.g. for cell nuclei but not for mitochondria). For practical purposes, especially during the experimental verification process, the 4th order approximation of this curve (Figure 3.6, red line) was used to estimate the scatterer diameter corresponding to each spectrum. It must be mentioned that the COD bandwidth and the scatterer size relation depend on the wavelength and the spectral range of the light source and also the refractive indices of the medium and scatterer.

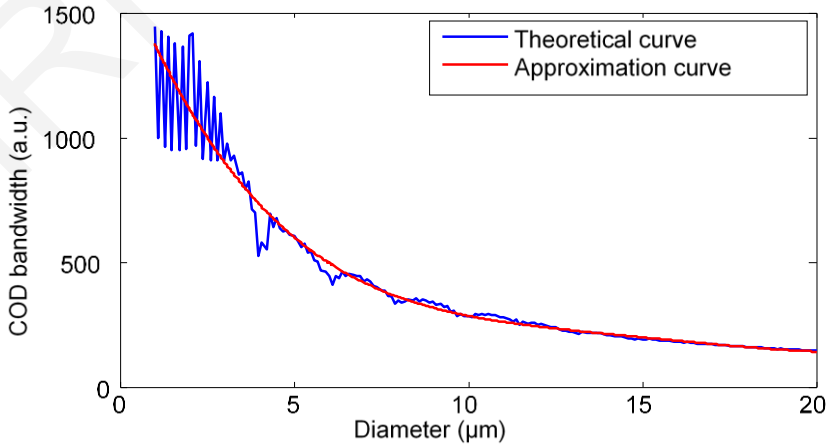

Figure 3.6. Correlation of the Derivative (COD) bandwidth as a function of scatterer size. The blue line is the theoretical curve from Mie theory and the blue line the 4th order approximation curve. Reliable scatterer estimation can be performed only in the region above four μm (solid red line) [173].

Spectral processing

A short time Fourier transform (STFT) of a moving Gaussian window is used in order to extract the depth resolved spectrum from the OCT images. This window separates the portion of the signal that corresponds to the observed region and decreases the side-lobes of the resulting FFT peaks (compared a rectangular window). Then, the depth resolved spectra are divided by the source spectra (taken from an OCT mirror image) to get the backscattering profile of the sample at each corresponding spatial region. Also median and low pass (LPF) filtering are used for spectra smoothing to avoid noise amplification during the differentiation process. Furthermore, the spectrum edges, which are more susceptible to noise than the central part since the borders of the source spectrum are lower in intensity compared to the center spectral region, are removed. An important factor that must be considered is noise since it can be very detrimental to scatterer estimation. It can affect, the estimation of the first minimum of the autocorrelation of the derivative by up to half a period which is an error of 20-60% on scatterer size depending on the slope of the curve of Figure 3.6. Differentiation is performed by obtaining the difference between adjacent values in the spectrum.

It is important to note that the position of the Gaussian window with respect to the scatterer may have an impact on the spectrum. When the window is depth-displaced, it affects the intensity but does not affect the spectrum. The Gaussian window can be applied at different depths. Regardless of the window location in the axial direction, as long as the Gaussian width includes the interface between the scatterer and the matrix, the spectrum will have the same shape. When the window includes the entire axial length of the scatterer and the interface at both the upper and lower sides, the signal results in a spectrum of the highest intensity (Figure 3.7). However, there is a more important dependence of the depth resolved specta on shifts in the lateral direction (Figure 3.8). The maximum intensity spectra appear when the spatial window is in the center of the scatterer and as the window shifts to adjacent positions, the intensity falls off and also the waveform shape changes. This is an expected outcome because as the beam is shifted laterally only a part of the sphere is in the focal volume, and so the beam crosses a smaller effective diameter. To deal with this problem an intensity threshold (5 dB above the noise floor) is applied, below which the spectra are ignored, or compare three adjacent spectra and assign to each position the spectrum with the highest intensity.

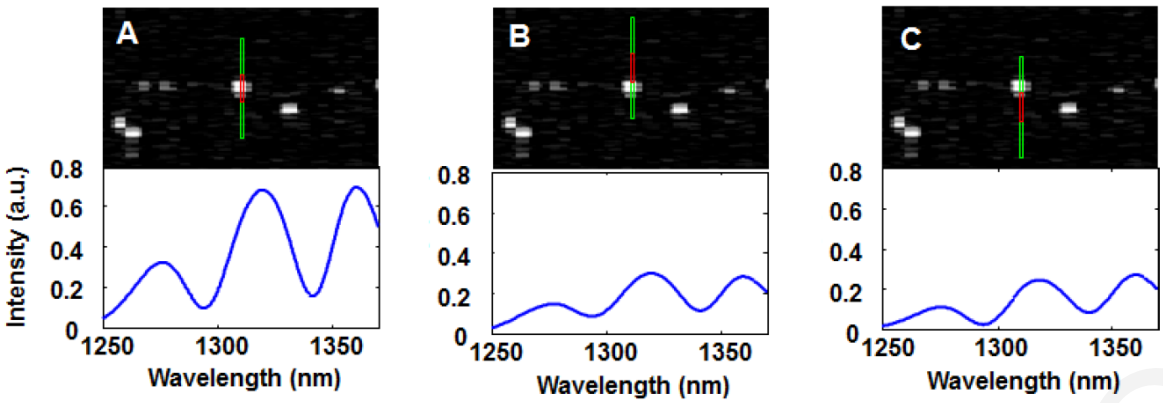

Figure 3.7. Backscattering spectra dependence on the axial location of the Gaussian window. On the top are regions of OCT images of a phantom with 10 μm diameter microspheres and at the bottom are the resulting backscattering spectra. Centering on (A), above (B), and below (C) the microsphere only affects the intensity but not the shape of the spectrum [173].

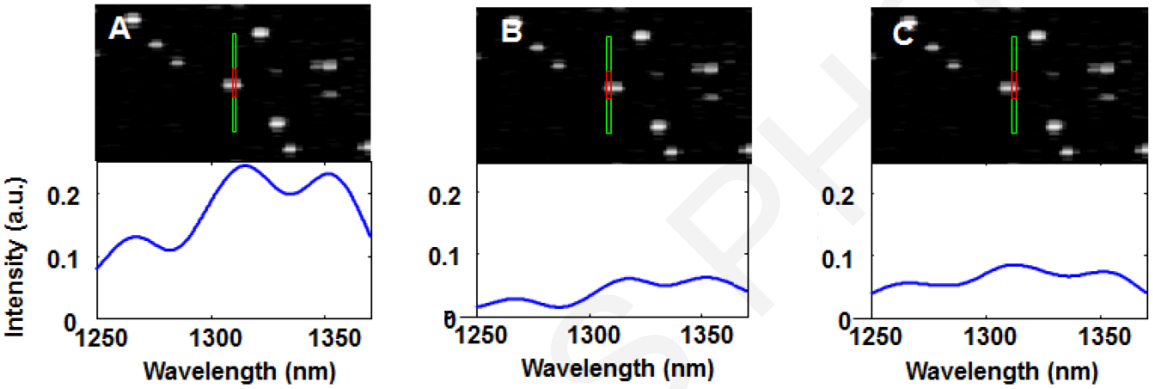

Figure 3.8. Backscattering spectra dependence on the lateral location of the Gaussian window. On the top are regions of OCT images of a phantom with 10 μm diameter microspheres and at the bottom are the resulting backscattering spectra. Centering on (A), left (B), and right (C) of the microsphere affects both the intensity and the shape of the spectrum [173].

3.7 Features for OCT image classification

Feature extraction and selection are important procedures for OCT imaging classification. A good feature selection should have effective and discriminating features that could lead to accurate classification results. However, simply combining the most significant features will not necessarily result in best performance. The goal of feature extraction and selection is to identify the best discriminating performance of the feature group. Generally, the most important features for classification using OCT images are the intensity and structural based features which can be texture, morphological and/or fractals. Extraction and selection of effective features is crucial and the general guidelines for selecting significant features mainly include four considerations: discrimination, reliability, independence and optimality.

3.7.1 Texture features

Textures are complicated intensity patterns or sub patterns that have characteristic properties (brightness, color) and can be seen as a similarity grouping in an image [174]. Local sub pattern properties give rise to important characteristics like lightness, uniformity, density, roughness, smoothness, etc., of the texture [175]. There are four main steps in texture analysis. First, feature extraction to estimate various characteristics of an image able to describe its texture properties. Texture discrimination to divide a textured image into portions, each matching to a particular homogeneous texture. Texture classification to specify to which of a pre-defined set of classes a segmented texture portion belongs and, finally, texture shape in order to be able to rebuild the surface (3D) geometry from texture information.

Different methods of texture analysis include structural, statistical, model-based and transform approaches. Structural approaches [175], [176] use texture and hierarchy of spatial arrangements of different primitives. To represent the texture, the primitives and rules concerning placement must be defined. The selection of a specific primitive and the probability of it located at a particular position can be a function of the position or the primitives near the position. The resulting symbolic description of the image of the structural approach offers several advantages, though, this method is more applicable for synthesis rather than analysis. These complicated descriptions can be weak for natural textures because of the variability of the different structures (micro and macro) and no clear separation between them. In medical image analysis, Serra et al, and Chen et al, proposed a tool, based on mathematical morphology, useful for bone image analysis detecting bone microstructures [177], [178].

Statistical approaches do not attempt to understand explicitly the hierarchical structure of the texture as the structural methods do. As an alternative, they identify the texture indirectly by the non-deterministic properties of the distributions and relationships between the image's grayscale intensity levels. Various techniques based on second order statistics (by pairs of pixels) were reported to have very good discrimination results [179]. Julesz et al, examined for the first time human texture discrimination in terms of the texture statistical characteristics [180]. They reported that the textures in gray scale images are distinguished spontaneously only if they vary in second order statistical moments in contrast to third-order moments that require much extra effort. This could provide an indication that statistics up to the second order could be more significant for automatic processing as well [181]. Significant second order statistical features for texture analysis can be extracted from

the co-occurrence matrix proposed by Haralick in 1979. Many studies have confirmed that those features are very effective for texture discrimination in medical images. Also, research based on multi dimensional co-occurrence matrices was shown to surpass wavelet packets when applied to texture classification [182], [183].

Model based texture analyses [184] [185], try to define an image texture by generative image and stochastic models using fractal and stochastic approaches. The calculated parameters of the model are then utilized for image analysis. In such analysis, the biggest problem is the computational complexity arising from the estimation of stochastic model parameters. Fractal models have initially been shown to be applicable to natural texture, modelling. Nevertheless, they have weak orientation selectivity and are not applicable to describing local image morphology when applied to texture analysis and discrimination [186], [187].

Transform techniques for texture analysis, like Fourier, Gabor [188] and wavelet transforms [189], identify the image in a space whose co-ordinate system has an interpretation that is tightly connected to the properties of a texture (such as frequency or size). Techniques based on the Fourier transform perform weakly in practice, because of its lack of spatial localization. Gabor filters provide the means for better spatial localization, but their usefulness is poor in practice due to the fact that there is usually no single filter resolution at which one can localize a spatial structure in natural textures. Wavelet transforms appear to have several advantages compared to the Gabor transform. First, they can represent of textures at the most suitable scale by varying the spatial resolution and, also, there is a wide range of wavelet functions so that one can choose the most appropriate for texture analysis for each specific application. These advantages make the wavelet transform attractive for texture segmentation. However, it is not translation invariant, which is a significant limitation [190].

Histogram based features (first order)

The intensity-based histogram is a function displaying the number of pixels in the image having a specific intensity level. It is a brief and simple summary of the statistical information enclosed in an image. Calculation of the gray level histogram contains single pixels and, hence, the histogram incorporates the first-order statistical information of the image. By dividing the intensity values with the total number of pixels in the image, the approximate probability density of occurrence of the intensity levels can be extracted. The shape of the histogram gives various clues as to the character of the image. For example, a

narrowly distributed histogram indicates a low contrast image. A bimodal histogram often suggests that the image shows an object with a narrow intensity range against a background of differing intensity. Various important features can be extracted from the histogram to quantitatively describe the first-order statistical characteristics of the image such as mean, variance, skewness, kurtosis, energy and entropy. These features can provide valuable texture information and can by calculated using the equations below, where *p(i)* is the probability density of occurrence of the intensity levels:

Mean: $$\mu = \sum_{i=0}^{G-1} ip(i) \quad (3.\ 11)$$

Variance: $$\sigma^2 = \sum_{i=0}^{G-1} (i-\mu)^2\, p(i) \quad (3.\ 12)$$

Skewness: $$\mu_3 = \sigma^{-3} \sum_{i=0}^{G-1} (i-\mu)^3\, p(i) \quad (3.\ 13)$$

Kurtosis: $$\mu_4 = \sigma^{-4} \sum_{i=0}^{G-1} (i-\mu)^4\, p(i) - 3 \quad (3.\ 14)$$

Energy: $$E = \sum_{i=0}^{G-1} [p(i)]^2 \quad (3.\ 15)$$

Entropy: $$H = -\sum_{i=0}^{G-1} p(i) \log_2 [p(i)] \quad (3.\ 16)$$

The mean is the central moment that gives the average intensity level of the image or texture being examined, while the variance indicates the variation of intensity around the mean. Skewness is an indication of symmetry. It is zero if the histogram is symmetrical about the mean. Otherwise, it is either positive or negative depending whether the distribution is skewed above or below the mean. Kurtosis is a measure of flatness of the histogram and entropy is an indicator of histogram uniformity. Other possible features, derived from the histogram, the minimum, maximum, range and median values. In case of natural images, the mean and variance do not really carry the information about the texture. They rather represent the image acquisition procedure, such as the average lighting conditions or the gain

of a video amplifier. Using images normalized against both the mean and variance can provide superior texture discrimination accuracy than using the actual mean and the actual variance as texture parameters [190] [191].

Co-occurrence matrix

The most significant advantage of using the texture statistics is their simplicity. Nevertheless, they cannot entirely characterise texture. Studies have shown that for a large class of textures, no texture pair can be distinguished if they agree within their second-order statistics [180]. Even though examples opposite to this conjecture were demonstrated, the signifigance of the second-order statistics is unquestionable. Thus, statistical techniques, utilized in texture analysis, nearly rely on the definition of the joint probability distributions of pairs of pixels.

Haralick et al. in 1979 proposed a the second-order histogram known as the co-occurrence matrix $hd\theta(i,j)$. When the matrix is divided by the total number of neighbouring pixels $R(d,\theta)$ in the image, it is then serves as the estimate of the joint probability, $pd\theta(i,j)$, of two pixels, a distance d apart along a given direction θ, having the particular (co-occuring) values i and j. There are two forms of the co-occurrence matrices: One symmetric where pairs separated by d and $-d$ for a direction θ are included, and another no symmetric where only pairs separated by a distance d are used. Typically, given the image $f(x,y)$ with a number of G discrete intensity levels, the matrix $hd\theta(i,j)$ is determined such that its (i,j)th entry is equal to the number of times that

$$f(x_1, y_1) = i \text{ and } f(x_2, y_2) = j$$

where

$$(x_2, y_2) = (x_1, y_1) + (d\cos\theta, d\sin\theta) \qquad (3.17)$$

This produces a square matrix of dimension equal to the number of intensity levels in the image, for each distance d and orientation θ. Because of the large number of computations required, often only the distances $d = 1$ and 2 pixels with angles $\theta = 0°, 45°, 90°$ and $135°$ are considered as suggested by Haralick. If the pair of pixels in the image are highly correlated, the entries in $hd\theta(i,j)$ are clustered along the diagonal of the matrix. The cooccurrence matrix calculation is shown in Figure 3.9 (d=1). The classification of thin textures requires small values of d, whereas coarser textures require large values of d. Reduction of the intensity levels number, by quantizing the image to fewer levels of intensity, increases the speed of computation but, at a loss of textural information.

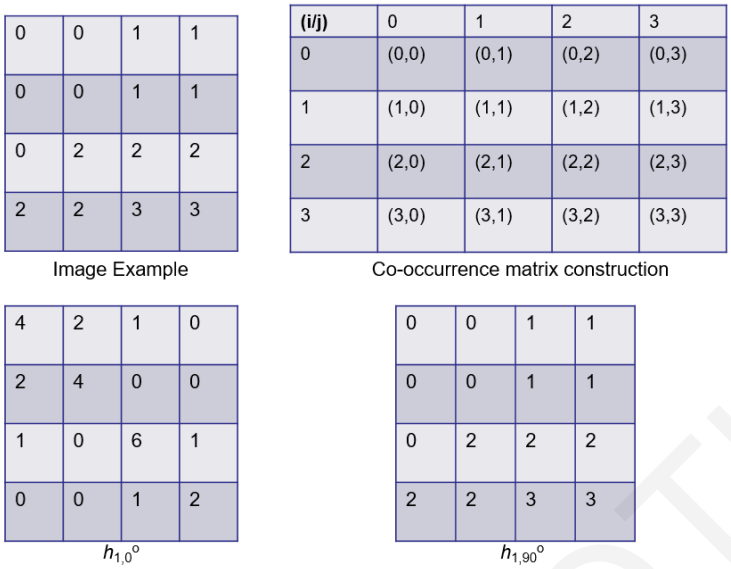

Figure 3.9. Spatial co-occurrence Haralick calculations.

The co-occurrence matrix involves G^2 components which too large for texture analysis with a reasonable computational time. For this reason, a number of new features can be calculated using the co-occurrence matrix [176], [191]. Angular second moment (energy), correlation, inertia, absolute value, inverse difference, entropy and maximum probability are some of these features defined by the equations that follow:

Energy: $$\sum_{i=0}^{G-1}\sum_{j=0}^{G-1}[p(i,j)]^2 \quad (3.18)$$

Correlation: $$\sum_{i=0}^{G-1}\sum_{j=0}^{G-1}\frac{ijp(i,j)-\mu_x\mu_y}{\sigma_x\sigma_y} \quad (3.19)$$

Inertia: $$\sum_{i=0}^{G-1}\sum_{j=0}^{G-1}(i-j)^2 p(i,j) \quad (3.20)$$

Absolute value: $$\sum_{i=0}^{G-1}\sum_{j=0}^{G-1}|i-j|\,p(i,j) \quad (3.21)$$

Inverse difference: $$\sum_{i=0}^{G-1}\sum_{j=0}^{G-1}\frac{p(i,j)}{1+(i-j)^2} \quad (3.22)$$

Entropy: $$-\sum_{i=0}^{G-1}\sum_{j=0}^{G-1}p(i,j)\log_2[p(i,j)] \quad (3.23)$$

Maximum probability: $$\max_{i,j}\,p(i,j) \quad (3.24)$$

where μx, μy and σx, σy are the mean and standard deviations of the row and column sums of the matrix, respectively (associated to the marginal distributions $px(i)$ and $py(j)$).

Grey-Tone Difference Matrix

The Grey-Tone Difference Matrix (GTDM) is a column vector involving G components proposed by Amadasun in 1989 in an effort to introduce texture measures associated with human perception of textures. Its values are calculated based an estimation of the difference between the intensity level of a pixel and the mean intensity calculated over a shifting square window centered at the pixel [192].

There are five main features extracted from the GTDM to quantitatively describe perceptual texture properties. Coarseness which is described by the size of texture primitives, contrast, which dependents on the intensity change between neighboring pixels, busyness, defined by high spatial frequency of intensity differences, complexity, which dependents on the number of different primitives, and mean intensities and texture strength associated with clearly visible primitives. The analytical definition of each is given below:

Coarseness:
$$C_{\cos} = \left(\varepsilon + \sum_{i=0}^{G-1} p_i s(i) \right)^{-1} \quad (3.25)$$

Contrast:
$$C_{con} = \left[\frac{1}{N_t(N_t - 1)} \sum_{i=0}^{G-1} \sum_{j=0}^{G-1} p_i p_j (i-j)^2 \right] \left[\frac{1}{n} \sum_{i=0}^{G} s(i) \right] \quad (3.26)$$

Busyness:
$$C_{bus} = \frac{\sum_{i=0}^{G-1} p_i s(i)}{\sum_{i=0}^{G-1} \sum_{j=0}^{G-1} | ip_i - jp_j |}, p_i \neq 0, p_j \neq 0 \quad (3.27)$$

Complexity:
$$C_{com} = \sum_{i=0}^{G-1} \sum_{j=0}^{G-1} \frac{|i-j|}{n(p_i + p_j)} [p_i s(i) + p_j s(j)], p_i \neq 0, p_j \neq 0 \quad (3.28)$$

Texture strength:
$$C_{str} = \frac{\sum_{i=0}^{G-1} \sum_{j=0}^{G-1} (p_i + p_j)(i-j)^2}{\varepsilon + \sum_{i=0}^{G-1} s(i)}, p_i \neq 0, p_j \neq 0 \quad (3.29)$$

Texture analysis has not been performed on OCT images until the early 2000s'.Now many studies argue for the importance of texture feature identification in OCT images.

Gossage et al., and Gao et al., used the spatial gray level dependence texture features (SGLDMs) and texture features derived from the two dimensional discrete Fourier transform (DFT) of mouse OCT images and OCT images of human skin, respectively, for tissue classification. SGLDM is the spatial histogram of an image that represents the distribution of gray scale levels and permits the calculation of the statistical textural features for the selected area including correlation, homogeneity, energy, entropy and contrast (inertia). Furthermore, texture analysis of OCT images has provided very promising results for OCT images from different gastrointestinal tract tissues [81], [193], [194]. These studies were based on the hypothesis that the morphological structure loss as the normal histological organization as a result of dysplastic tissue architecture transformation, is reflected in the texture features, such as lightness, uniformity, density and roughness of OCT images. Hence, these features could be used for tissue identification and diagnosis. Alternatively, image feature extraction, utilizing the two-dimensional discrete Fourier transform (DFT),was proven to be a reliable tool for tissue classification, since DFT features could distinguish texture periodicity and orientation. The DFT feature values represent the percentage of signal in a specific range of spatial frequencies. Images with big homogenous areas, such as normal areas of esophageal tissue, have large DFT feature values within the lower spatial rings. In contrast, images with small inhomogeneous regions, like the crypt-like glandular structures in Barrett's esophagus, have large DFT feature values within the higher spatial frequency rings [193], [194].

Furthermore, other studies report on the use of the center symmetric autocorrelation method (CSAC) [81]. To estimate the local center symmetric pattern covariance, utilizing two local center-symmetric auto-correlations is needed, linear and rank-order (SAC and SRAC), together with a related covariance measure (SCOV) and variance ratio (SVR), within pair variance (WVAR) and between pair variance (BVAR) [81]. In contrast to the SGLDM features, the specific are rotation invariant measures [195].

The textural properties of malignant tissue have been a significant analysis criterion for disease diagnosis. Textural heterogeneity of OCT, represented by the variance of intensity [196], was utilized to identify various abnormalities. Authors reported that OCT can distinguish gastric cancer [84], [197] , [198]. Automated textural analysis for different ophthalmologic pathologies is a well established, including OCT image segmentation, quantification, and separation of layers for diagnostic purposes [199] [200]. Analogous processing has been used to discriminate different types of skin dysplasia [201], ovarian cancer [73], esophageal malignancies [202] and coronary artery diseases [203].

3.7.2 Morphological features

In general, morphology uses various simple rules and shapes, like squares, circles, diamonds, cubes and spheres, to investigate and process the architecture of tissue in images. The main goal is to identify important features in images in order to perform high-level inspection functions. Examining and assessing complex objects begins with 'anchor point' characteristics, determined by object morphology. In contrast to texture features estimated from the regions of interest (ROIs), morphological features emphasize different local characteristics of the image, such as the shapes and borders.

In a study of gastrointestinal tissue disease classification using OCT images, Garcia-Allende et al. applied morphological assessment using intensity distributions of different image regions. For each image, regions were created based on intensity measure segmentation using the *k*-means algorithm to separate different data points into *k* clusters in an iterative procedure [196]. Figure 3.10 (A and B) illustrates examples of intensity and PR images consisting of four clusters. Marvdashti et al. [204], in their study of Bacal Cell Carcinoma (BCC), extended this morphological analysis by incorporating the positional information associated with pixels within each image region in both the lateral and the axial directions. The traditional and extended analysis were carried out on both intensity and phase retardation data. The shape and spatial extent of the regions correlated with the histology-based classification of the B-scan. For both image types, they calculated morphological features by segmenting the data within the binary ROI into two through six regions and then calculated statistics for each region such as: mean, normalized mean, absolute deviation, relative size, standard deviation, skewness, kurtosis.

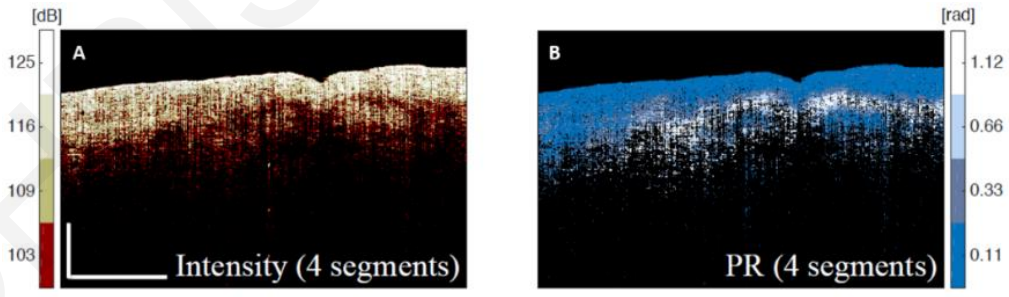

Figure 3.10. Examples of four (A) intensity and (B) PR image regions calculated using k-means algorithm for morphological analysis. The scale bars represent 500 µm × 500 µm. [204]

Various morphological shapes and borders of tissue are very important for OCT image analysis. For example, OCT can accurately image the morphological characteristics

of skin tissue microstructure, i.e., stratum corneum, epidermis, dermis, hair follicles, eccrine sweat ducts, and sebaceous glands (Figure 3.11) [205].

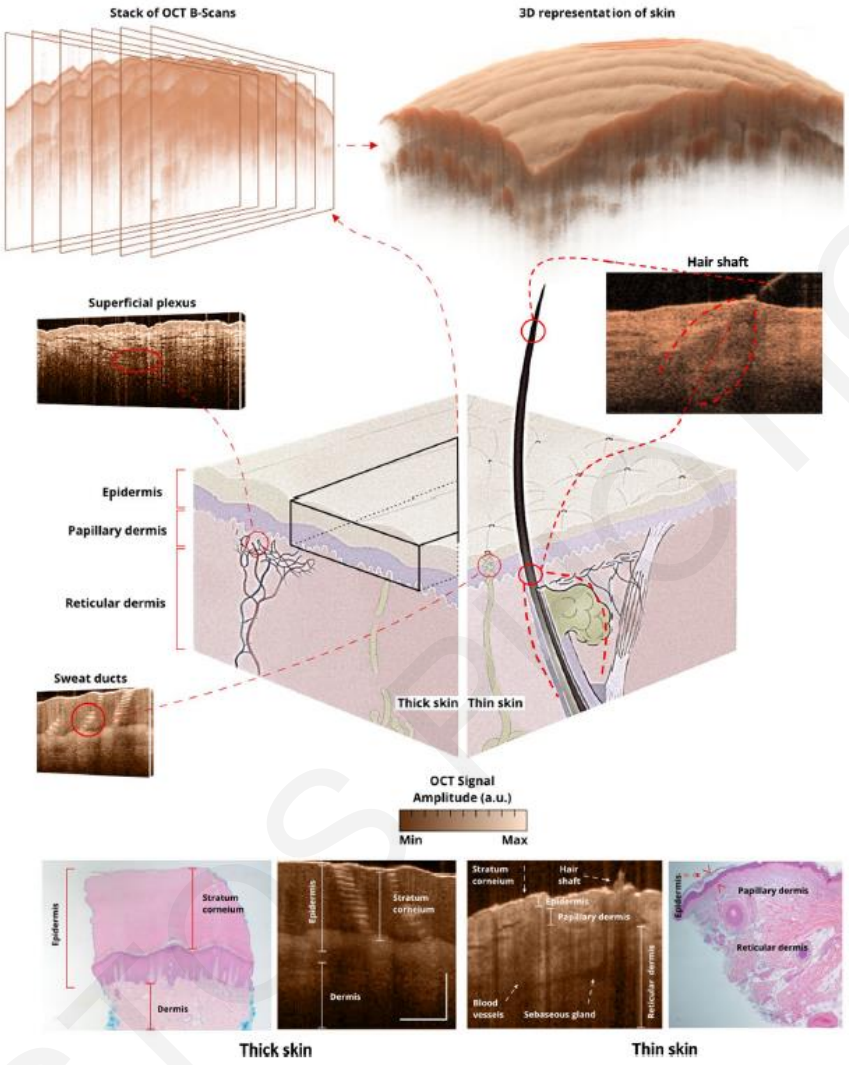

Figure 3.11. Sequential images obtained by OCT (top left), and the 3D OCT representation of the skin (top right). The center illustration demonstrates several skin structures and their corresponding appearance on OCT. The bottom images demonstrate thick skin and thin skin, and annotated structures, their corresponding equivalent histology, and OCT images. The scale bar in OCT images is 400 μm. [205]

Luo et al., [51] explored morphological feature analysis classification (MFAC) to distinguish stomach malignant tissue. The stomach region of interest (ROI) was examined only to a depth of 1.2mm in every image. Normal stomach tissue is a regular structure and every layer is homogeneous. Malignant stomach tissue is heterogeneous with alternating high and low backscattering crypts that obscure the normal features. Therefore, three quantitative features to represent the stomach OCT image characteristics were proposed: the standard deviation at the ROI 40th-pixel depth line, the standard deviation of the intensity line of 0.25 × 20th + 0.5 × 40th + 0.25 × 60th, and the standard deviation of all 100 contour depth lines. The results showed that the three extra morphological features adequately

represent the layered structures and are markedly different in OCT images of normal and cancerous stomach. (Figure 3.12**,** Figure 3.13)

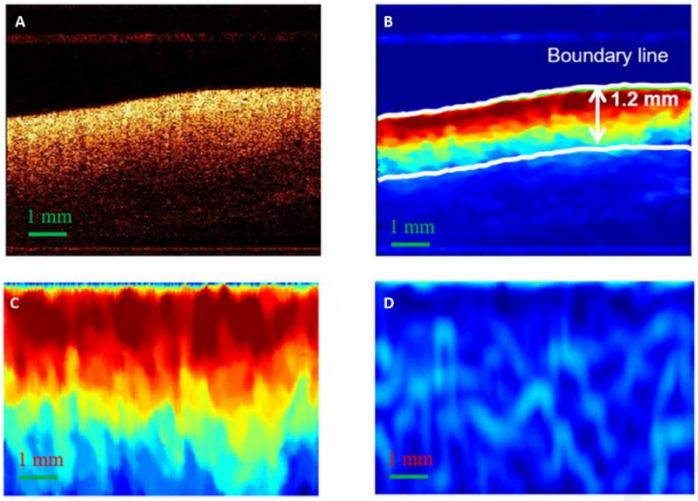

Figure 3.12. The image processing of the normal OCT images. (A) The original OCT image; (B) the image of preprocessing; (C) ROI image; (D) the image of local standard deviation. (Scalar bar: ~1 mm.). [51]

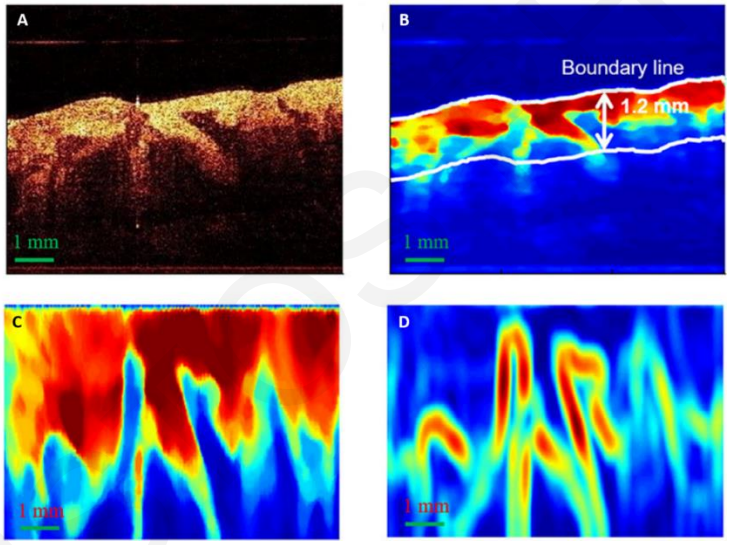

Figure 3.13. The image processing of the cancerous OCT images (A) The original OCT image; (B) the pre-processing image; (C) ROI image and (D) the local standard deviation. (Scalar bar: ~1 mm.). [51]

Morphological features have also been applied to esophageal OCT images, in an effort to distinguish different grades of dysplasia in Barrett's esophagus (BE) using endoscopic OCT (EOCT). The morphological features appeared to play an important role in tissue classification. A characteristic of dysplasia in Barrett's images was reduced scattered intensity, probably resulting from the transformed optical properties of the dysplastic region. Dysplasia progressed through different stages and was mainly characterized by cellular alterations (size, shape and density of nuclei within the layer of epithelium) (Figure 3.14). These alterations influenced the scattering by the tissue. The profile of each A-scan in the EOCT image was associated to the backscattered power as a depth function and the optical

characteristics of the tissue. Qi et al., reported another visible characteristic of EOCT images, distinguishing dysplasia in BE, is the lack of the stripe-like patterns that can be seen in Barrett's images without dysplasia (Figure 3.15). These patterns rarely appeared in dysplastic EOCT images. Even though the reason these stripes appear was not determined, they proved to be a very useful feature for tissue classification [81], [206] , [207].

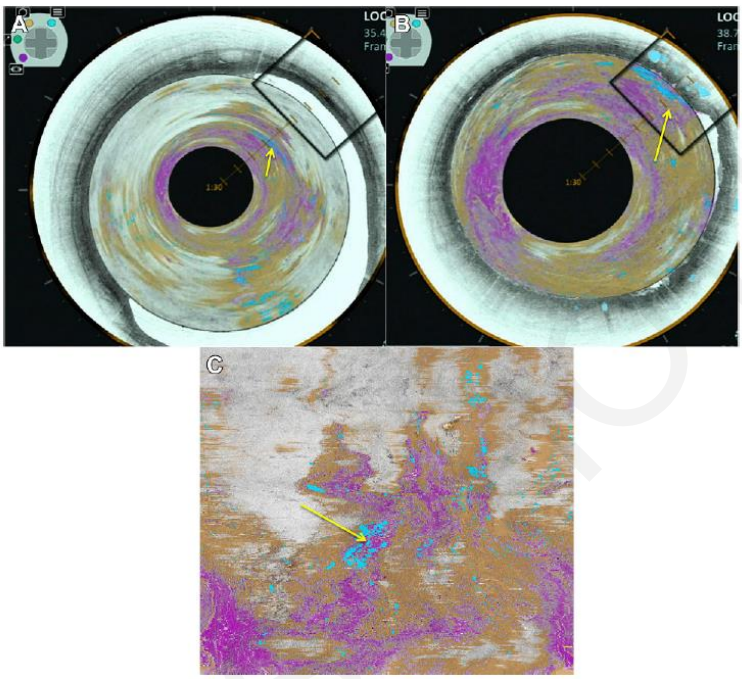

Figure 3.14. Esophagus image of the OCT showing a luminal en face view of an area of overlap (yellow arrow) between the 3 features of dysplasia (orange is lack of layering, blue is glandular structures and pink is a hyper-reflective surface). (A) A view looking down from the proximal esophagus. (B) A view closer to the suspected area of dysplasia. The en face view is also shown (C). [207]

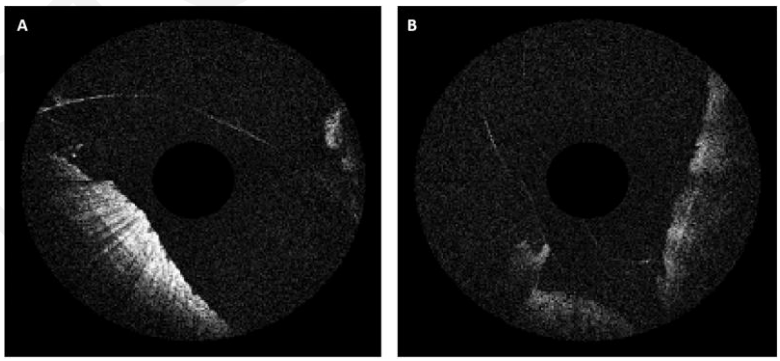

Figure 3.15. (A) Shows the obvious stripe pattern within a non-dysplastic BE EOCT image. (B) Shows no obvious stripe pattern within a high-grade dysplastic BE EOCT image. [81]

3.7.3 Fractal features

Fractal analysis

Mandelbrot in 1967 proposed fractal geometry and the concept of the fractal dimension (FD), to show the self-similar pattern, when he estimated the length of the coastline of the United Kingdom [208]. He noticed that the total length of the coastline varied when he changed the ruler's size to calculate the coastline length. Hence, he used the FD as a scale that was applied to the ruler. The scale could be utilized as a pointer to characterise the roughness of a surface such as the coastline. Because of this description, complicated objects can be assessed using the FD. Higher values of the FD imply higher roughness of the surfaces. Thus, mathematics can be applied to nature, but nature can also be used to create new mathematical areas. Fractals are everywhere, from lightning bolts to vegetables.

In Euclidean theory, various structures consist of basic Euclidean geometries such as lines, circles and cubes. A simple straight line has one dimension, while a plane has two and a cube has precisely three dimensions. These basic shapes of integer dimensions are known as topological dimensions. A fractal curve has dimensions between a straight line and a plane (one to two), and a fractal surface has dimensions between a plane and a cube (two to three). To calculate the FD of complicated structures, numerous definitions of FD were used. A simple definition of the FD is the Hausdorff dimension, which can be defined as follows:

$$FD = \lim_{r \to 0} \frac{\log N_r}{\log(\frac{1}{r})}, \tag{3. 30}$$

where N_r is the number of sets of cells (a ruler used to measure map coastlines) and $1/r$ is the magnification factor that used to decrease the cell in every spatial direction. An example of a geometric structure with a non-integer dimension is the Koch curve (Figure 3.16). The straight line E_0 is the initiator and has a length of one. The middle third of the line E_0 is substituted two lines that each has the same length (1/3) as the remaining lines on either side. Therefore, the length of the line E_1 is now 4/3. This form determines a rule that is used to make other new forms. Consequently, the curve E_0 is used as the initiator, and the curve E_1 as a generator for creating the Koch curve. Each line is replaced by four lines, each 1/3 the length of the initial one. Thus, the lengths of the lines E_2, E_3, and F are 16/9, 64/27, and 256/81, respectively. As shown in Figure 3.16, the total length of the curve rises with every

step and leads to an infinite length. By using equation 3.29 the FD could be calculated as $ln4 / ln3 = 1.26$.

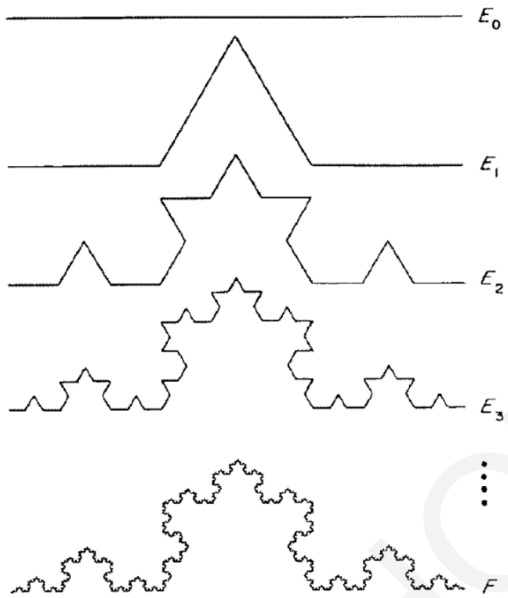

Figure 3.16. Koch curve. Initiator (E_0) and generator (E_1) are used for constructing the Koch curve. Curves E_2, E_3, and F are levels 2, 3, and 4 in the construction of the Koch curve, respectively. [209]

Additionally, the estimation of the coastline FD could be estimated as the Koch curve, using a box counting method. In the measurement of the coastline, the number of scaled ruler is also counted as well as the size of the cell. Equation 3.29 is utilized in the estimation of the FD. Note that the cell is a box shaped cell (a square) for two-dimensional objects and that the cell is a cube for three dimensional objects (Figure 3.17). The box counting method is the most common technique to calculate the FD in different fields because of its ease to use. Nevertheless, the box counting method was found to miscount the number of boxes (cells), something that leads to erroneous calculations of the FD [210], [209].

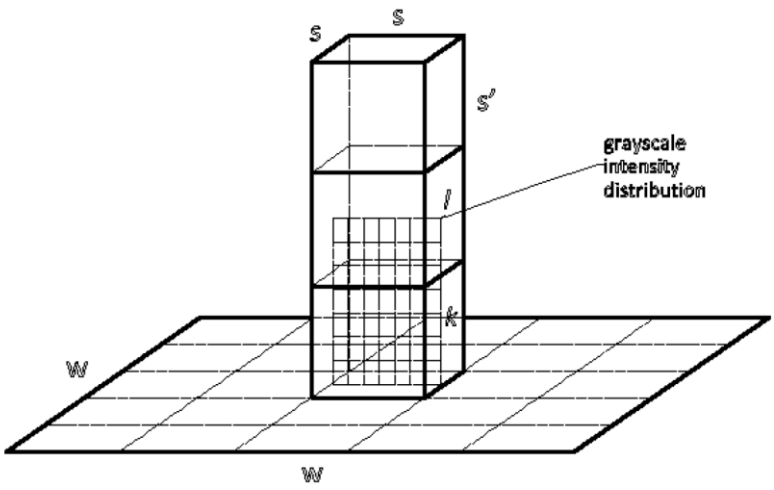

Figure 3.17. Sketch of determination of the number of boxes by the differentiate box counting method. [210]

Fractal analysis of OCT images

The above method can be adapted to estimate the FD of OCT images. If a grayscale OCT image is used in cartesian coordinates (x,y,z), the coordinates (x,y) represent a 2D location on the image plane, and the coordinate (z) indicates the intensity value. Using the 2D differentiate box counting technique, the image plane is wrapped by the non overlapping grids. Assuming the gray scale image size is $W \times W$, then the non-overlapping grid size is $s \times s$ and $W/2 \geq s \geq 2$. If G is the number of gray levels, the value s' (in z dimension) can be obtained from: $s' = Gs/W$. Therefore, the size of the box that is used to cover the 3D spatial surface is $s \times s \times s'$ (Figure 3.17). Assuming that the minimum and maximum gray level in the (i, j) grid were in the box number k and l, respectively, the number of the boxes covering the surface in the grid (i, j) is: $nr\ (i, j) = l - k + 1$. Summing the contributions across all grids, we have

$$N_r = \sum_{i,j} n_r(i, j), \qquad (3.\ 31)$$

where N_r is counted for different values of r. Then, the fractal dimension of 2D OCT image can be estimated from the least square linear fit of log (N_r) divided by log ($1/r$) as in equation 3.29. [210].

The FD has been used in the analysis of OCT images to examine the structural variations of biological tissues. Fluearu et al. utilized the box counting method to calculate the FD for porcine arterial tissue characterization [211]. Sullivan et al. used the same technique to calculate the FD for breast malignancy classification [212] (Figure 3.18). Furthermore, human skin studies reported that melanomas had a larger FD than basal cell carcinomas and benign melanocytic nevi when two fractal techniques were used in the calculations. The results could be explained by the fact that melanomas appeared to have heavily disorganized vessels with confusing branching. Both the FD and the differential box counting dimension could be utilized as an index to discriminate melanomas from the basal cell carcinomas and the benign melanocytic nevi [213].

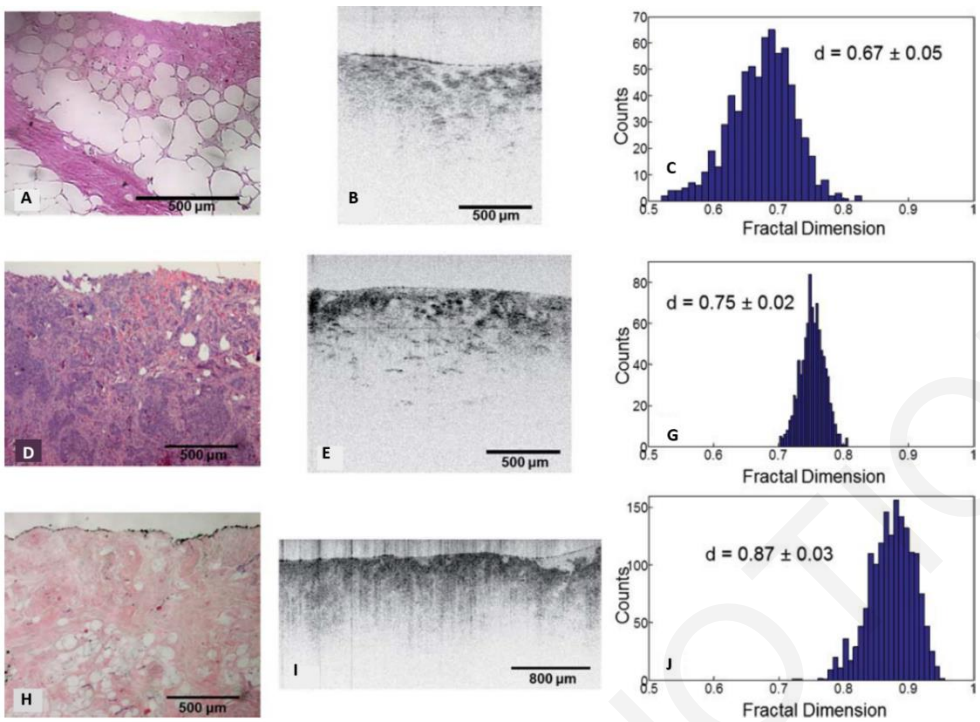

Figure 3.18. Microscopy images of breast tissue [(A), (D), and (G)], along with the corresponding OCT images [(B), (E), and (H)], and distributions of fractal dimension values [(C), (F), and (I)] for the entire region. The tissue classifications for these regions are adipose [(A)–(C)], cancer (invasive ductal carcinoma) [(D)–(F)], and stroma [(G)–(I)]. Stromal regions within the adipose tissue (A) and adipose cells within the cancer (D) and stromal tissues (G) are heterogeneities that may broaden the measured fractal dimension distribution. [212]

In ophthalmology, researchers evaluated the fractal properties of the retinal vasculature for diagnostic purposes. Most of them have used variations in the FD to distinguish and diagnose eye disease [214], [215]. Generally, an overall measure characterizing the whole branching pattern of the retinal vascular network has been proposed as a unique parameter. Fractal analysis of OCT images has also been used to quantify photoreceptor rearrangement and vision restitution, recognize glaucomatous impairment at early stage in the retinal nerve fiber layer and as an indicator of other pathological syndromes. Furthermore, it has been applied to discriminate normal healthy eyes from diseased eyes with early neural loss in multiple intraretinal layers (multiple sclerosis) using a local approach through segmentation of the numerous cellular layers of the retina and representation of texture features on OCT images [216]. Somfai et al., [217] employed a power spectrum approach to perform fractal analysis of the layered retinal tissue to diagnose diabetic retinopathy. This study applied fractal analysis on each A-scan of the segmented regions. Hence, only the irregularity or roughness lengthways the A-scan contributed to the 1D fractal analysis and all other directions were unknown.

3.8 Medical Imaging Classification

3.8.1 Introduction

Machine learning (ML) is a field of Artificial Intelligence that solves real world problems by equipping computers with learning skills. It emerges from the combination of statistics, which seek to discover relationships in data, and computer science, while concentrates on efficient computing algorithms. This relation, originating from the computational challenge of building statistical models from massive data sets, which can include enormous amount of data points. ML is divided into two main categories: supervised and unsupervised learning. Supervised learning aims to predict a known output or target. In contrast, in unsupervised learning there are no known outputs to predict, but instead, the aim is to find recurring patterns or groups within the data [218].

ML is extensively used for biomedical signal and image processing. Since the understanding of biological systems is not complete, there are important features and information in biological data that are not readily obvious. In addition, the interactions between different subsystems are not easily recognizable. Biological data are also characterized by substantial variability, caused either by internal mechanisms or by external stimuli. Associations between the different parameters can be too complex to be solved with classic techniques. ML methods can help model the nonlinear relationships that exist in these data, and extract parameters and features which can improve diagnosis and management of disease [219], [220], [221].

The main machine learning applications in medicine are smart electronic health records, drug discovery, biomedical signal and image processing and disease identification and diagnosis. In most cases of disease identification and diagnosis, the development of ML systems is considered as a trial to imitate the medical experts' knowledge in the recognition of disease. ML permits computer programs to learn from data, develop a model to recognize common patterns and make decisions based on collected knowledge and, in addition, work with the incompleteness of medical data sets. Computer medical image analysis systems can be very valuable to the medical diagnosis process. The goal is to enhance the clinician’s ability to find disease regions while decreasing the need for intervention, and enhancing the capability for precise diagnosis [222]. The need for more efficient techniques of early detection of disease by computer assisted medical diagnosis systems is obvious [223].

3.8.2 Machine learning in medical imaging

During the last decades, increasing amounts of data are extracted from various biomedical imaging systems, requiring ML methods that can be applied to growing volumes of information and detect more complex patterns than human medical experts in the healthcare domain can process [224]. ML models are trained to facilitate the assessment of medical images and enhancement of medical diagnosis procedures. There are various established models which depend, for example, on employing pixel level morphological procedures for tumor edges extraction [225], cell geometric characteristics for cell recognition [226], texture analysis using different ML methods such as Naïve-Bayes (NB), Neural Networks (NN), Decision Trees (DT),etc., [227], [228], [229]. However, identification and classification of early disease changes in human tissue in medical images is very difficult due to the complicated architecture and structural morphology and the subtlety of early stage abnormalities. Abnormal or diseased tissues are regularly diffused with weak contrast. Furthermore, the majority of human tissues have different size and shape characteristics and require computational models with advanced plasticity and capacity in contrast with nature based models [230]. Lately, novel models have reported enhanced results in various medical image analysis fields such as brain tumor discrimination [231], knee cartilage segmentation recognition [232], diagnosis of muscle diseases using muscle ultrasound [233]. Still, the application of ML methods to medical image classification remains problematic having critical limitations in terms of utility and applicability.

Recently, several biomedical imaging systems and various ML methods have been utilized for different tissue detection applications. Du et al., [227] evaluated unsupervised ML algorithms (k-means, Expectation Maximization (EM), threshold-based segmentation, and Global Minimization of the Active Contour (GMAC) model) for segmentation of three types of fluorescent cellular images from fluorescence microscopy. The process included images of synthetic cell, nuclei images, and brain cell images. They concluded that k-means clustering, threshold-based segmentation, and GMAC had better performance than EM that only had a better sensitivity. In addition, in another study showed that the Decision Tree algorithm had the best accuracy result compared to ANN's, association rule-based classifier, NB classifier, SVM, logistic regression, and Bayesian networks on breast tumor features from mammograms [228]. In other studies, hybrid models for brain tumor recognition from MRI [234], rank error-based learning on contrast-enhanced MRI (CE-MR) images and a mixture of rough set and support vector machine (MRS) models [235] were also used. Feature selection and extraction were also addressed by practicing Rough Set Theory to

eliminate unnecessary features [236] and unsupervised feature extraction methods with a *K*-SVM model that hybridizes a *k*-means algorithm with an SVM on breast cancer datasets [229]. This model delivered the best accuracy (97.38%) and the best computational time on a public dataset of breast cancer when compared with different feature selection methods with a heuristic approach. Ensemble learning is another trend that has been proposed to disease identification by gathering base models.

Besides these conventional ML procedures, some special learning structures were also proposed for medical image processing. The first example is stream data learning. Usually, the training of ML algorithms is performed by utilizing static datasets. However, new patients and new data present continuously described as online or real-time data, incremental data or stream data. When new data sets arrive, if an ML algorithm is completely trained again on the updated batch dataset (the batch dataset is updated by adding the new into the prior data), the model keeps ignoring old patterns or patterns with insufficient representation, something that is also known as unlearning. For this reason, an incremental learning model is used to deal with the unlearning problem. Molina et al., introduced an augmented ensemble learning algorithm applied for prostatic cancer identification [237]. In that study, the new augmented learning algorithm was learning from new incoming data without ignoring the prior patterns.

Recently convolutional neural networks (CNNs) for tissue segmentation and classification using a Deep-Learning approach have become very popular. Research includes application to GI tract and dental images, noise removal tasks, brain tumour segmentation, breast cancer, thyroid cancer and retinal diseases recognition [238], [239], [240], [241], [242]. CNNs are deep artificial neural networks that are used primarily to classify images, cluster them by similarity and perform object identification within scenes [243], [244], [245], [246], [247]. They are algorithms that can identify faces, tumours or any other aspect of visual data. The strength of CNNs arises from their deep structure which allows the extraction of features from various abstraction layers [248], [249], [250], [251]. Basically, all CNNs are made of a series of layers defined by a specific number of filters or kernels that mainly have the role of feature detectors from a set of input images. Sliding the filters on the input images and calculating the convolution of these filter matrices and input image matrix produces a set of convolved features. The meaning of learning in a CNN is to train the CNN architecture with the values of these convolutional operations [252] [253], [254].

3.8.3 OCT image classification

Experts using OCT images of different tissues, usually try to perform disease diagnosis manually expending valuable effort and time. Sommerey et al., tried to identify the fat, thyroid, parathyroid, and lymph using OCT with manual assessment, which attempts to correlate the image findings to the corresponding histology [35].

Image assessment with morphological methods is a common processing method and is utilized for OCT image analysis as shown by Macedo et al. [255]. The results of these approaches are extremely sensitive to image properties such as noise and intensity variations. The performance of morphological methods is also restricted to images with small dimensions and not very complex patterns. For large images with more complicated patterns, these operations require a lot of computational time while, at the same time their performance is limited, due to the image variations.

OCT image assessment using ML has been recently introduced, especially in volumetric images, which pose numerous challenges pertaining to classification, discrimination and segmentation. A well known process to implement medical image segmentation is the development of different shape models like statistical shapes [256] and deformable [257] and level-sets models [258]. Studies also demonstrate that pixel/portion classification methods can reach encouraging performance while at the same time be less influenced by image characteristics like noise and artifacts for segmentation tasks [259].

Nam et al. demonstrated an automatic recognition paradigm of vessel lumen and stent struts utilizing a classic feature extraction approach [260]. In this study, an OCT system was used with a catheter able to scan the inner structure of blood vessels and gather OCT images [255]. Image preprocessing and feature extraction steps were performed during the feature-based ML procedure. Since OCT images suffer from speckle noise and also other artifacts, the success of the procedure was limited [261]. Aggressive preprocessing for speckle noise elimination and artifact correction are crucial for successful feature extraction leading to accurate diagnosis as shown by Baghaie et al. [259].

Fuller et al. and Garvin et al. introduced ML with SVMs applied to semi-automatic segmentation and examination of a graph-theoretic segmentation of retinal layers' for human intraretinal layer segmentation [261], [262]. Also, Liu et al., utilizing Principal Component Analysis (PCA), Local Binary Pattern (LBP) and SVMs, demonstrated a ML method to distinguish normal macula and multiple macular diseases [263]. The algorithm

was tested on 326 OCT scans from 136 patients. An energy-decreasing active contour approach for intra-retinal layer detection using OCT data collected from 7 rats was also proposed by Yazdanpanah et al. [264]. In addition, Xu et al. used a boosting model for glaucoma detection by grouping adjacent pixels to a super pixel [265]. Lu et al., resorted to a Decision Tree (bagged) classifier for stent struts recognition in human coronary and Anantrasirichai et al., utilized PCA and SVM algorithms for glaucoma discrimination based on texture analysis [266] , [267]. Multi-scale Histogram of Oriented Gradients (HOG) descriptors as features were used by Srinivasan et al., to achieve retinal pathology recognition with the utilization of an SVM algorithm [268]. The constructed OCT dataset from their study was utilized later by various researchers [269], [252].

Another study from Lenz et al., demonstrated the application of *k*-means clustering on Short Time Fourier Transform (STFT) features to detect brain healthy and malignant regions [270] (Figure 3.19). LBP and HOG techniques were used together by Alsaih et al. for feature extraction and were also evaluated with an SVM algorithm for diabetic macular edema automatic recognition [271]. Moreover, Wang et al., introduced a study of the application of Linear Configuration Pattern (LCP)-based features and Sequential Minimal Optimization (SMO) which resulted in a very good outcome for retinal pathologies detection [272].

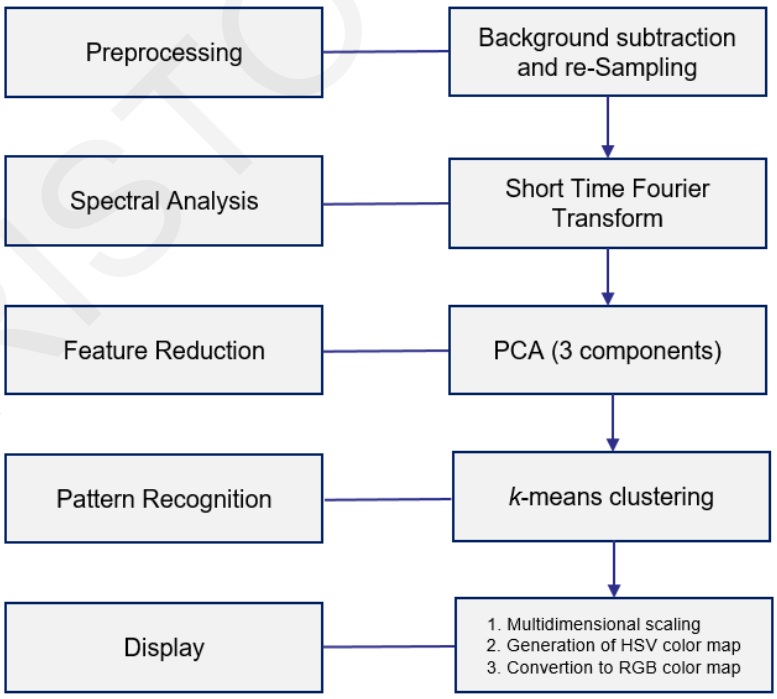

Figure 3.19. Processing model for ex vivo brain tumour classification. [270]

Luo et al., developed a classification method based on morphological feature analysis (MFAC), in combination it with ML, to identify stomach cancer. They, first, extracted five quantitative morphological features from OCT images using the structured analysis. Then, they evaluated five ML classifiers for the classification process (SVM's, the *K*-nearest neighbor, random forest, logic regression, and conventional threshold method). The results showed that features specifically created for stomach malignancies were significantly better than the classic morphological image features with over 95% accuracy for all five classifiers [51]. Allende et al., also applied morphological analysis of OCT images for automated classification of gastrointestinal tissues using several types of ML methods with sensitivity values up to 99.97%, specificity up to 99.85% and accuracy up to 99.88% depending on the features selected for classification [196].

Qi et al., developed computer-aided diagnosis algorithms for dysplasia in Barret's esophagus classification using an endoscopic OCT system (EOCT). They evaluated the performance of four types of multivariate analysis for discriminating dysplasia in BE: linear and quadratic discriminant analysis (LDA & QLA), K-nearest neighbor (*k*-NN), two types of neural networks (NNs) (single-hidden-layer NN (SLNN) and learning vector quantization (LVQ) network), and classification trees. The results indicate that their CAD system has the potential to detect accurately the presence or absence of dysplasia for surveillance of Barrett's esophagus with an accuracy of 84% for the classification of non-dysplastic vs. dysplastic BE tissue [81]. In addition, Ughi et al. created a method for automated segmentation and characterization of the esophageal wall *in vivo* using a segmentation and classification algorithm. Their procedure could effectively describe the diseased esophageal wall with an A-Scan line classification accuracy of 94% with a sensitivity and specificity of 94% and 93%, respectively (Figure 3.20, Figure 3.21) [273].

Another study examined the texture and optical features of the OCT images of human breast tissue at different resolutions, and created computational methods for differentiation of major tissue types found in OCT images, such as adipose and malignant lesions. Relevance vector machine (RVM), a Bayesian frame work of support vector machine, was used to perform classification on adipose tissue against solid type of tissue, and invasive ductal carcinoma (IDC) against normal stroma tissue with an overall accuracy of 84%, sensitivity of 89% and specificity of 71% [68].

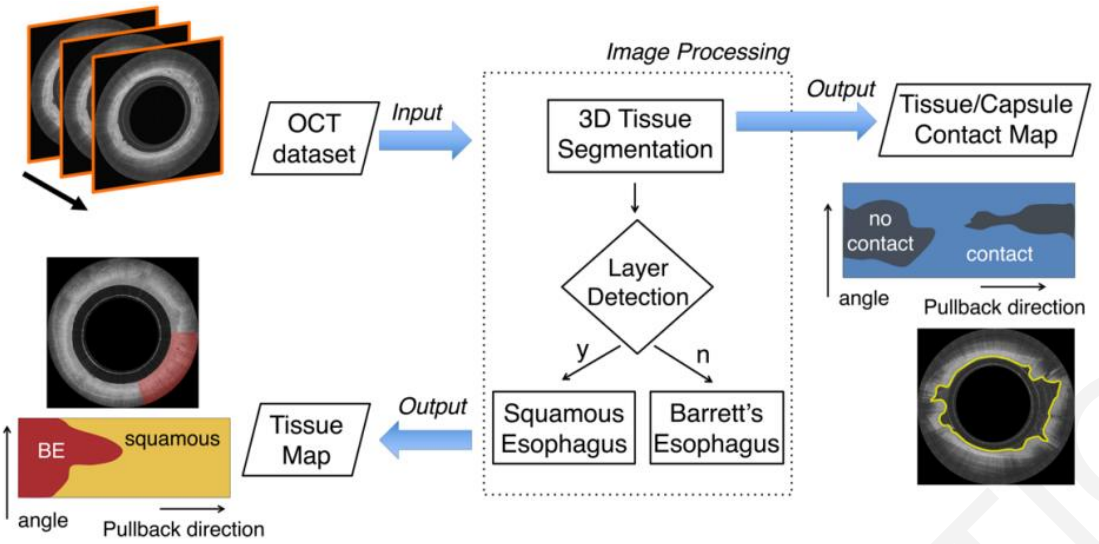

Figure 3.20. Flowchart of the entire automated processing framework used for esophageal wall characterization. [273]

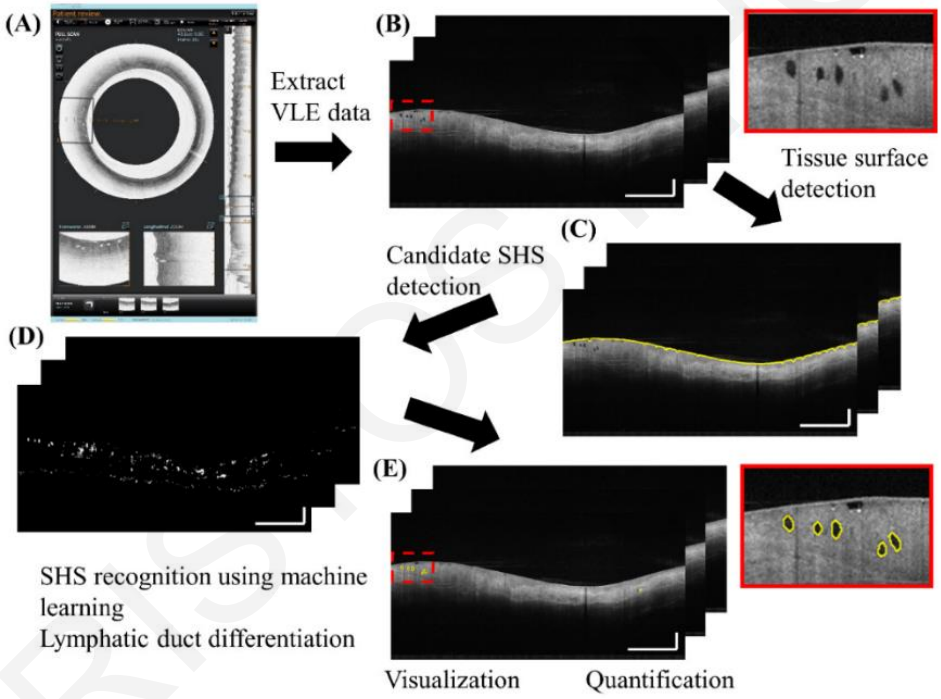

Figure 3.21. Fully automated algorithm for dysplasia detection in BE and quantification. Inset: zoomed-in view.(Scale bars: 1 mm. [273]

Table 3-1 summarizes ML research applied to OCT images for different tasks. It is clear that the majority of these ML studies are related to ophthalmological pathologies. The majority of the approaches before 2017 applied feature-based ML techniques with image classification. Since 2017, convolutional neural networks (CNNs) are more routinely used for the most tasks.

TABLE 3-1. MACHINE LEARNING STUDIES USING OPTICAL COHERENCE TOMOGRAPHY

Study	Clinical Application	Method	ML Algorithm
Qi 2006 [81]	Detection of dysplasia In Barret's Esophagus	Image classification	PCA Classifier
Fuller 2007 [261]	Retinal layers segmentation	Voxel classification	RBF Kernel
Lingley 2008 [274]	Urinary bladder cancer	Image classification	Decision Trees
Liu 2011[263]	Macular diagnosis	Image classification	RBF Kernel
Lu 2012 [266]	Stent struts detection	Image classification	Boosted Decision Trees
Ding 2013 [275]	Retinal fluid segmentation	Image classification	Graph cut, Split Bregman, Random Forest
Xu 2013 [265]	Glaucoma detection	Pixel classification	Logit Boost
Lang 2013 [276]	Retinal layers segmentation	Pixel classification	Random Forest
Albarrak 2014 [277]	Macular Degeneration diagnosis	Image classification	Linear SVM
Yoshida 2014 [278]	Glaucoma detection	Image classification	Random Forests
Srinivasan 2014 [268]	Retinal diseases recognition	Image classification	SVM
Xu 2015 [265]	Retinal fluid segmentation	Voxel classification	KNN
Kafieh 2015 [279]	Retinal pathologies recognition	Boundary localization	Complex K-SVD

TABLE 3-1. MACHINE LEARNING STUDIES USING OPTICAL COHERENCE TOMOGRAPHY

Study	Clinical Application	Method	ML Algorithm
Miri 2015 [280]	Segmentation of optic disc	Pixel classification	Random Forest
Bogunovic 2015 [281]	Retinal layers segmentation	Voxel classification	ANN
Gao 2015 [213]	Skin cancer	Image classification	ANOVA followed by Newman–Keuls post-hoc analysis
Marvdashti 2016 [204]	Skin Bacal cell carcinoma	Image classification	Linear SVM) , *k*-nearest neighbor
Nam 2016 [260]	Coronary stent strut detection	Image classification	ANN
Lenz 2016 [270]	Brain classification	Clustering	K means clustering
Wang 2016 [272]	Macular Degeneration diagnosis	Image classification	Sequential minimal optimization
Gan 2016 [282]	Atrial tissue classification	Image classification	Relevance vector machine
Alsaih 2016 [271]	Diabetic macular edema recognition	Image classification	SVM
Lu 2017 [266]	Stent struts detection	Image classification	Ada Boost
Lu 2017 [283]	Retinal fluid segmentation	Pixel classification	Random Forest
Fang 2017 [284]	Retinal layers segmentation	Image classification	CNN
Karri 2017 [269]	Retinal diseases detection	Image classification	CNN
Breger 2017 [285]	Retinal fluid segmentation	Image classification	Random forest, ANN
Lee 2017 [286]	Macular edema segmentation	Pixel classification	CNN

TABLE 3-1. MACHINE LEARNING STUDIES USING OPTICAL COHERENCE TOMOGRAPHY

Study	Clinical Application	Method	ML Algorithm
Moiseev 2018 [287]	Segmentation of tumors	Pixel classification	Random Forest
Gholami 2018 [251]	Recognition of ocular pathologies	Image classification	Meta Learning
Gessert 2018 [288]	Instrument pose tracking	Regression	ANN
Kolluru 2018 [250]	Voxel plague detection	Voxel classification	Decision Trees
Devalla 2018 [249]	Optic nerve classification	Pixel classification	CNN
Rong 2018 [252]	Retinal discrimination	Image classification	CNN
Sawyer 2018 [289]	Cancer of the ovaries	Image classification	Active contour
He 2018 [248]	Retinal layers segmentation	Pixel classification	CNN
Aslam 2018 [290]	Macular Degeneration diagnosis	Regression	ANN
Zhang 2018 [240]	Classification of thyroid tissue	Image classification	Deep convolutional networks(DCGAN,WGAN)
Lu 2018 [239]	Segmentation of thyroid tissue	Image classification	Weighted CNN
Palomar 2019 [247]	Multiple sclerosis detection	Image classification	Decision trees, SVM Multilayer Perceptron

TABLE 3-1. MACHINE LEARNING STUDIES USING OPTICAL COHERENCE TOMOGRAPHY

Study	Clinical Application	Method	ML Algorithm
Butola 2019 [42]	Breast cancer detection	Image classification	CNN
Abbasi 2019 [241]	Image noise removal	Unsupervised	CNN
Dubey 2019 [246]	Breast cancer detection	Image classification	Ensemble Learners
Fang 2019 [291]	Detection of macular pathologies	Image classification	CNN
Rong 2019 [252]	Eye pathologies evaluation	Image classification	CNN
Li 2019 [253]	Image segmentation of Esophagus	Image segmentation	U-net
Li 2019 [254]	Retinal pathologies recognition	Image classification	Transfer Learning
Lu 2019 [292]	Retinal fluid segmentation	Pixel classification	Random Forest, U-net
Christopher 2020 [245]	Glaucoma Detection	Image classification	Deep CNN
Salehi 2020 [242]	Dental caries classification	Image classification	CNN
Hossbach 2020 [243]	Angiography evaluation	Image classification	U-net
Lee 2020 [244]	Plaque characterization	Image classification	Hybrid CNN

CHAPTER 4
USING SPECKLE TO MEASURE TISSUE DISPERSION IN OCT

4.1 Summary

This chapter proposes a new technique for estimating the dispersion using the image speckle to calculate the *psf* degradation and does not rely on distinct and strong reflections. Since speckle is present in most biological samples, this technique is applicable to any tissue and can be implemented *in vivo* and *in situ*. The proposed method was verified *ex vivo* with Group Velocity Dispersion (GVD) values comparable to methods described in the literature. Further more, its applicability to cancer diagnosis was evaluated on a small set of gastrointestinal (GI) normal and adenocarcinoma OCT image resulting in with 93% sensitivity, 100 % specificity and 96 % accuracy. These promising results indicate the potential of the proposed method to become an important diagnostic tool, but it should be further investigated to elucidate its advantages and limitations [293].

4.2 Theory

The methods of dispersion measurement from OCT images, described in section 3.2.1, are not suitable for *in vivo* measurements and are limited only to particular applications where clear and strong, single, reflections are present. A new novel method is proposed here that can be applied in the absence of such reflectors. It is based on the estimation of the point spread function (PSF) which is extracted from the dispersion-induced variation of the speckle pattern.

In addition to other image features, OCT speckle is also affected by dispersion. The induced change in the speckle size can be used to estimate the image PSF broadening and, subsequently, to calculate the GVD. However, speckle variations, given the randomness of the speckle signal, are difficult to estimate. The approach proposed here is to compare small portions of an OCT image (of the order of twice the width of the system resolution), denoted as $i_s(z)$, which contain mainly speckle. Such a section from the surface of the sample, $i_s(0)$, where there is no dispersion-induced broadening, and one at a depth z, $i_s(z)$, where the effects

of dispersion are visible. The two images are related by a depth-dependent speckle-degrading impulse response, *sdf(z)*, such that

$$i_s(z) = sdf(z) * i_s(0) \tag{4. 1}$$

where the * denotes the convolution of the two terms and *z*, in the solution presented here, takes the values of $z=d_0, 2d_0, \ldots, L$. To obtain an estimate of *sdf(z)*, in a practical and accurate manner, a Wiener-type minimization can be used [294]. For that purpose, the following least mean square error function, $\varepsilon(z)$, is defined

$$\varepsilon(z) = E\left\{\left|i_s(z) - sdf(z) * i_s(0)\right|^2\right\} \tag{4. 2}$$

where *E* denotes expectation. Minimizing the error function, $\varepsilon(z)$, using a Wiener deconvolution approach, results in an estimate for *sdf(z)*. In analogy to *sdf(z)*, there exists another impulse response, *rdf(z)*, of a similar form, which describes the dispersion-induced degradation of the system resolution. For calculating the GVD, it is not necessary to explicitly derive the *rdf* since only its width is required, which can be estimated from

$$d_{rdf}(z) = d_o \frac{d_{sdf}(z)}{d_{sdf}(0)} \tag{4. 3}$$

where d_0 is the system resolution and $d_{sdf}(z)$ is the width of the *sdf* at depth *z*. The result of the convolution of the *rdf* with the OCT image is a degraded image with resolution width $d_d(z)$ given by

$$d_d(z) = \sqrt{(d_0)^2 + (d_{rdf}(z))^2} \tag{4. 4}$$

since the convolution of two Gaussians, the point spread function (*psf)* and the *rdf*, results also in a Gaussian with a width that is the root mean square of the widths of the two original functions. Given this width, d_d, the GVD can be calculated using equation (3. 2).

4.3 Experimental methodology

4.3.1 *Ex vivo* verification of image speckle Method

In order to validate the speckle-based technique, pure collagen gel, porcine muscle and adipose tissue samples were imaged *ex vivo*. The GVD was estimated both using the novel proposed method as well as the standard PSF degradation method, described in section

3.2.1 which served as a reference for verification of the results. The pure collagen samples served the purpose of initially testing the proposed methodology using a sample of known dispersion under well-controlled conditions. In addition, the *ex vivo* tissue samples served as an initial test of the applicability of the technique to highly scattering biological material. A swept source OCT system, with a center wavelength of 1300 nm and a resolution of 12 μm in air, was used to image sample sections placed over a reflector (microscope slide) which also served as a reference for the actual thickness and system resolution measurements. Eight images were taken from each different type of sample.

For each image, the Gaussian width without dispersion (d_0) was measured from the free-space portion of the reflector (i.e. the portion not covered by the sample). The broadened Gaussian width (d_d) was estimated from the width of the reflector below the tissue. Using the location of the glass surface, the actual thickness of the sample (L) was also calculated as the distance from the top surface to the extension of the free-space reflector line (Figure 4.1). Given these parameters, the GVD was estimated using equations (3. 2) and (3. 3). In addition, the index of refraction was also calculated, as described in the literature [110]. The thickness of the sample, L, and the additional optical path length delay L', calculated from the OCT images (Figure 4.1), were used to get the index of refraction based on the equation (3. 10. These values were used for verification of the results.

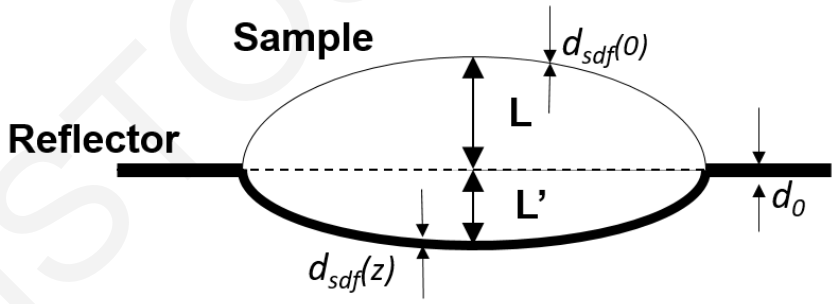

Figure 4.1. Values measured for verification purposes

The GVD was also estimated using the speckle-based technique as described above in 4.2. Given the randomness of the speckle and the noise in its width estimate, d_{sdf} was estimated at various depths and the broadening was calculated from the slope of a linear fit to those values (Figure 4.2). The median of the GVD from 250 individual A-Scans from each image as well as the standard deviation of the median GVD for all images of each sample type were used to compare the results and evaluate the accuracy of the both methods.

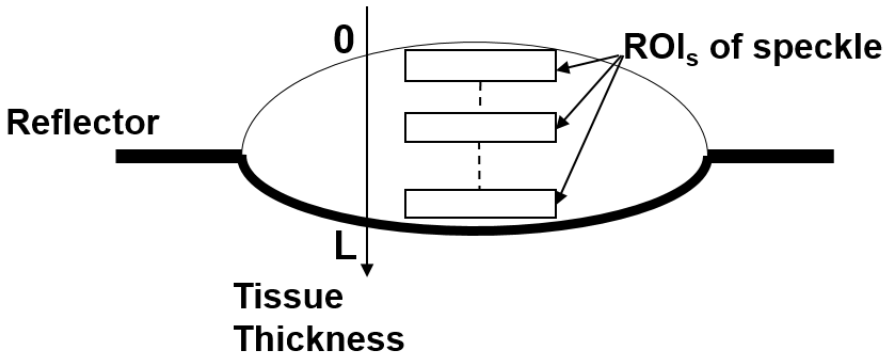

Figure 4.2. The novel presented technique was applied to regions of interest (ROI_s) of speckle at various depth within the sample

4.3.2 Application to GI images

To demonstrate the applicability of the novel speckle-based method to human tissue, the technique was applied to OCT images of normal and cancerous colon obtained from patients who were scheduled for surgical excision of their tumors. Eleven normal and fourteen abnormal images were included in this preliminary study. Since the actual tissue thickness could not be measured, it was estimated from the distance measured by OCT in air divided by an average index of refraction of 1.4 (which, despite being an approximation, it does not deviate more than 5% from the range reported in the literature). The GVD was estimated up to a depth of approximately 0.5 mm (as measured in air) for 500 A-Scans per image. Using the statistics of these GVD measurements (such as mean, standard deviation, and other moments.) the samples were classified as normal or abnormal using Linear Discriminant Analysis (LDA) and leave-one-out-cross-validation (LOOCV).

4.3.3 Results

The new proposed method was verified *ex vivo* using the same samples. Examples of the images collected are shown in Figure 4.3, Figure 4.4 and Figure 4.5.The median GVD for each type of sample as well as the standard deviation between the images of each type were calculated as described in section 3.2.1, 4.2 and are shown in Table 4-1.

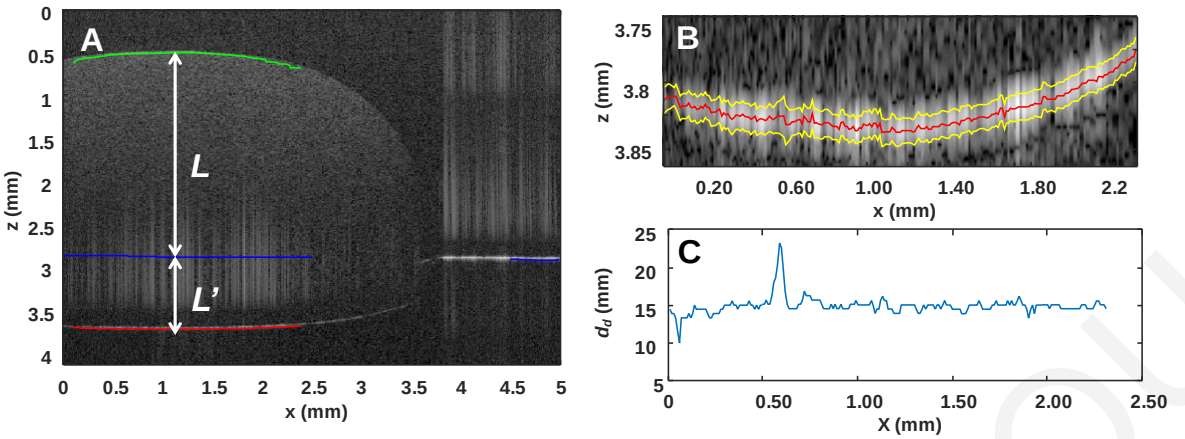

Figure 4.3. (A) OCT image of a pure collagen gel placed over a reflector (green line: top surface, red line: bottom surface, blue line: reflector, L: tissue thickness at that particular location). (B) Zoomed portion of the bottom surface (red) with the FWHM (yellow). (C) The FWHM of the reflector calculated at each of 250 A-Scan.

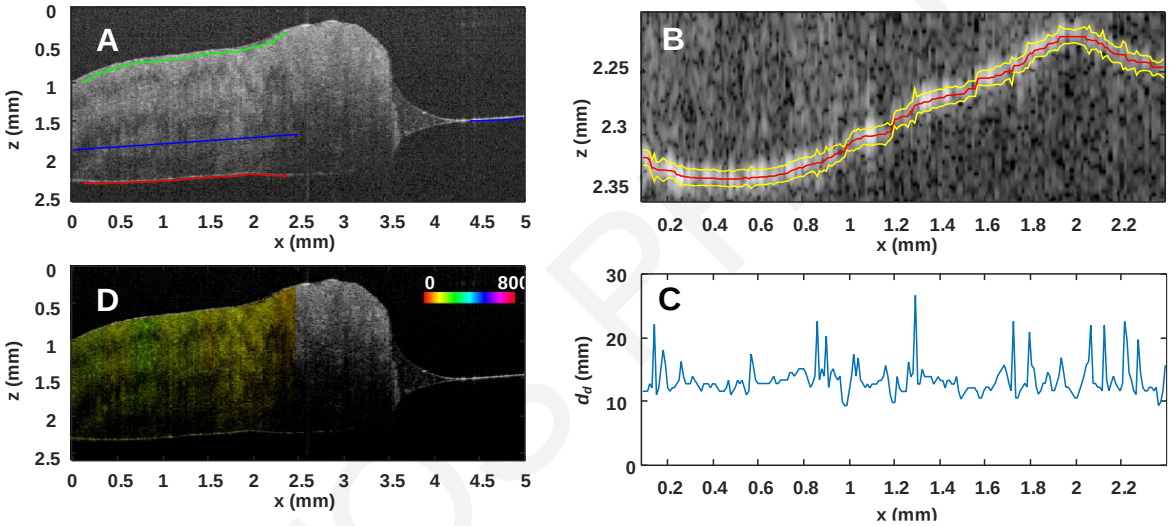

Figure 4.4 (A) OCT image of porcine muscle placed over a reflector (green line: top surface, red line: bottom surface, blue line: reflector). (B) Zoomed portion of the bottom surface (red) with the FWHM (yellow). (C) The FWHM of the reflector calculated at each of 250 A-Scan. (D) The OCT image with the GVD overlaid in a pseudo-color hue scale

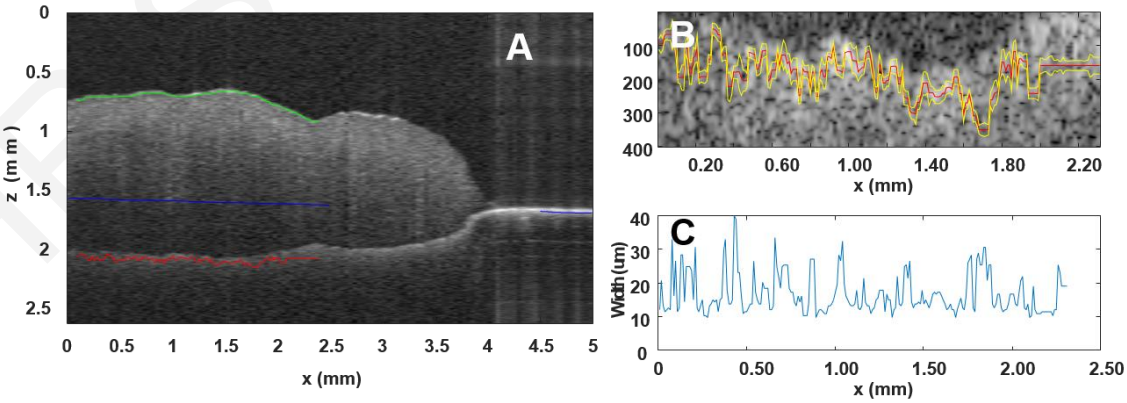

Figure 4.5. (A) OCT image of adipose tissue placed over a reflector (green line: top surface, red line: bottom surface, blue line: reflector). (B) Zoomed portion of the bottom surface (red) with the FWHM (yellow). (C) The FWHM of the reflector calculated at each of 250 A-Scan.

The implementation of the speckle-based approach included the division of each OCT image in smaller strips (twice the width of the system resolution), containing mainly

speckle (Figure 4.6 A and B), and estimating the *sdf* (Figure 4.6 C) with a Wiener-type deconvolution as described before. The width of the *sdf* for all A-Scans was measured and the mean calculated (Figure 4.6D). The process was repeated as a function of depth Figure 4.6 E). The dispersion-degraded image resolution width, d_d, was, then, estimated from a linear fit of *sdf* mean width (Figure 4.6 F). This technique was applied to the same samples as the standard method (Figure 4.7) and the results were compared to experimentally validate the new methodology.

TABLE 4-1. GVD MEASURED WITH THE PSF DEGRADATION AND SPECKLE-BASED METHOD AND MEAN INDEX OF REFRACTION MEASUREMENTS

	PSF degradation method			**Speckle-based method**			**n**		
	Median (fs^2/mm)	**Std (fs^2/mm)**	**Std (%)**	**Median (fs^2/mm)**	**Std (fs^2/mm)**	**Std (%)**	**Median**	**Std**	**Std (%)**
Collagen	135.72	5.77	4.25	135.62	12.70	9.36	1.369	0.003	0.24
Muscle	136.86	16.79	12.14	133.08	13.59	10.21	1.427	0.032	2.25
Adipose	249.90	28.65	11.25	267.20	55.60	20.81	1.630	0.128	7.70

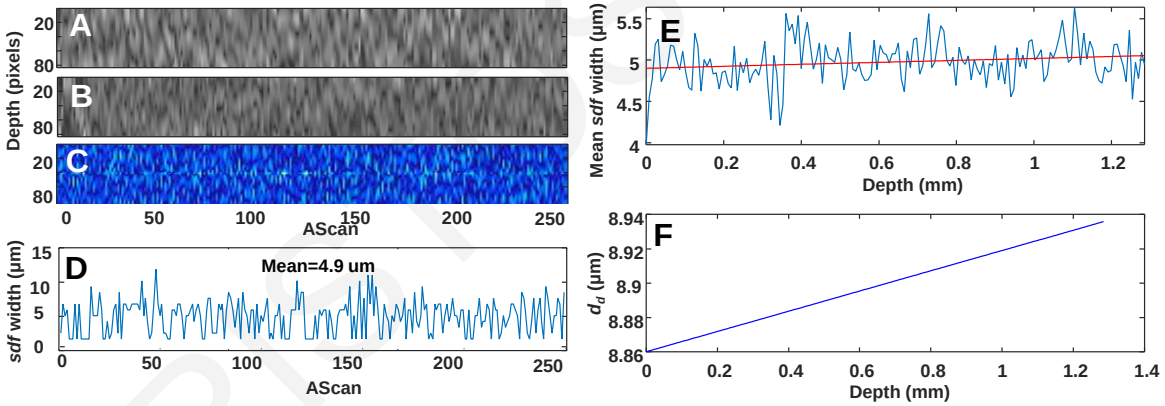

Figure 4.6. (A) Portion of the image (80x250 pixels) containing mainly speckle from just below the top surface (z = 0) of the sample of Figure 4.3. (B) Similar portion from just above the bottom surface (z = L). (C) The SDF resulting from the deconvolution. (D) The width of the SDF for the 250 A-Scans in (C). (E) The mean SDF width as a function of depth with a linear fit (red line) illustrating the increase as a function of the depth. (F) The degraded width of the PSF as a function of depth calculated from the linear fit in (E).

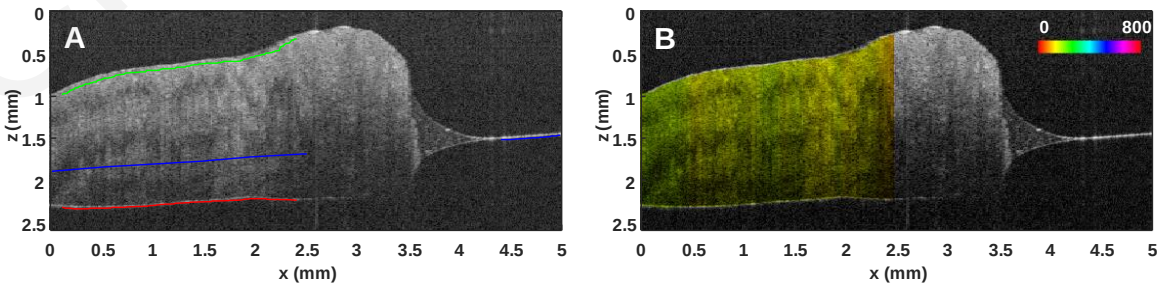

Figure 4.7. (A) OCT image of Fig. 1. (D) The OCT image with the GVD, calculated using the speckle-based method, overlaid in a pseudo-color hue scale.

The comparison between the standard resolution (PSF) degradation method and the proposed speckle based technique is shown in Table 4-1. The median GVD values agree within < 7% although the resolution (PSF) degradation method appears to be slightly more robust with standard deviation of measurements varying between 4-12 % vs. 9-21 %.

In addition, the GVD was also estimated for the normal and abnormal colon tissues using the speckle-based method (Figure 4.8). For each image, the moments of the distribution of the GVD values were calculated. Several of these parameters exhibited statistically significant differences with the most significant being the median with a p- value of 0.0007 (Figure 4.9). A recombination of these parameters using one-way Multivariate Analysis of Variance (MANOVA) applied for comparing the multivariate means. The resulting canon (C1), i.e. the linear combination of the original variables that has the largest separation between groups, produced the maximal statistical difference in the two populations. In addition, using the first six statistical moments of the GVD values and Linear Discriminant Analysis (LDA) with leave-one-out-cross-validation (LOOCV), the samples were classified with 93% sensitivity and 100 % specificity (96 % correct classification).

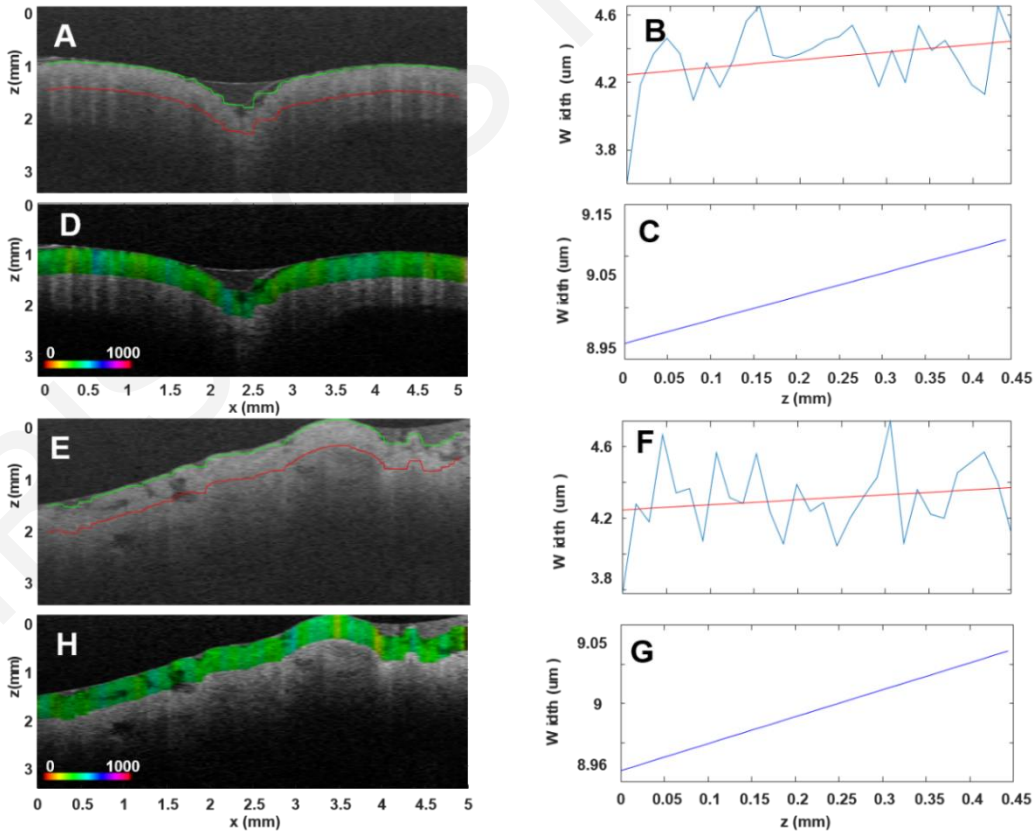

Figure 4.8. (A) OCT image of normal colon tissue (green line: top surface, red line: 0.5 mm depth). (B) Mean *sdf* width as a function of depth for (A). (C) Degraded Gaussian width, d_d, as a function of depth calculated from (B). (D) Overlay of the OCT image (gray scale) and the GVD for each A-Scan in a pseudo-color hue scale. (E-H) The same as before for colon adenocarcinoma.

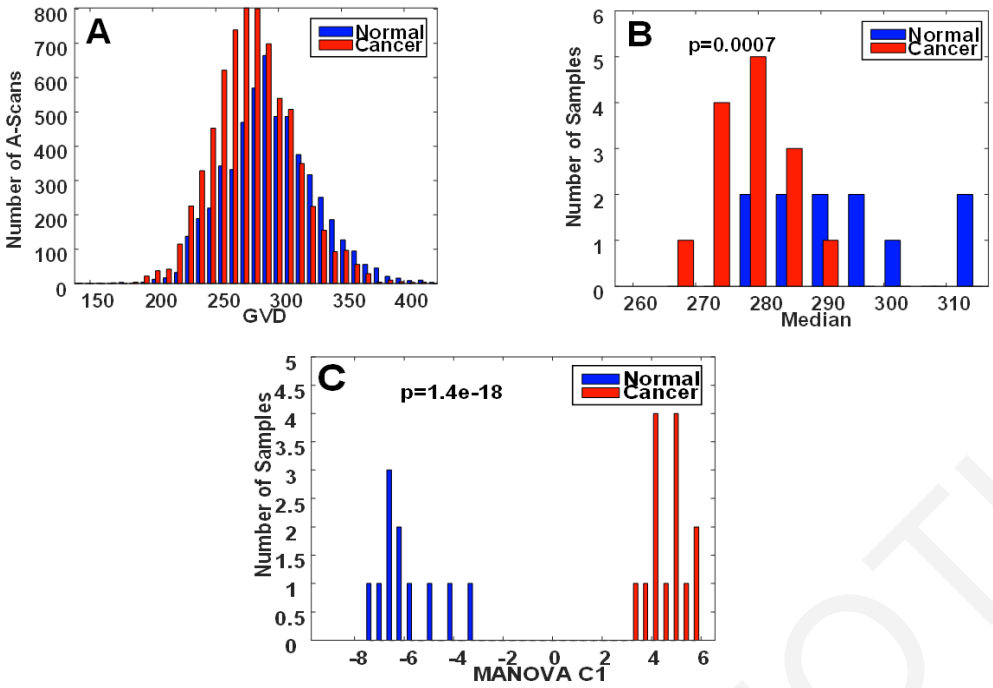

Figure 4.9. (A) Distribution of GVD values from normal and abnormal colon. (B) Distribution of the median of the GVD for each image exhibiting statistically significant differences. (C) Recombination of the statistical moments of the GVD values using MANOVA, exhibiting maximal statistical separation.

4.4 Conclusions

The GVD variations that exist between normal and malignant tissues could be useful in the detection of changes associated with early disease leading to an improvement of the diagnostic utility of OCT. However, most standard techniques to estimate sample dispersion rely on strong and distinct, single, reflections from which the width, shift or phase can be determined. Unfortunately, it is very rare to have such reflections in biological tissues. The new technique, proposed here, can estimate the *psf* degradation from the speckle pattern and is, thus, far more appropriate for *in vivo* imaging. This novel approach was shown, experimentally, to be effective in estimating the GVD with results comparable to the standard technique described in the literature for both low and highly scattering samples. In addition, it is sensitive enough to discriminate dispersion changes between normal and cancerous tissues. The success of these preliminary results indicates that further investigation is warranted, which should include both *ex vivo* and *in vivo* validation on a wider range of samples, to further elucidate the advantages and limitations of the proposed technique.

CHAPTER 5
MEASURING TISSUE DISPERSION USING THE CROSS CORRELATION OF HALF - SPECTRUM OCT IMAGES

5.1 Summary

In this chapter, another novel technique is proposed for estimating tissue dispersion by calculating the cross-correlation of images acquired at different center wavelengths to estimate the shift between their features. This shift, also known as walk-off, is then used to calculate the dispersion. Since a distinct reflector is not required, this method is applicable to any sample and can even be implemented *in vivo* and *in situ* in human tissue. The proposed technique was verified *ex vivo* resulting in Group Velocity Dispersion (GVD) values comparable to those obtained from estimating the walk-off from a mirror, as described in the literature. Furthermore, the method applicability to cancer diagnosis was evaluated on a small set of gastrointestinal normal and cancer OCT images. Using the statistics of the GVD estimates, tissue classification resulted in 100% sensitivity, 81% specificity and 92% accuracy. The success of these preliminary results indicates the potential of the proposed method, which should be further investigated to elucidate its advantages and limitations [295].

5.2 Theory

5.2.1 GVD measurement using speckle cross-correlation method

When dispersion is present, different wavelengths perceive varying path-lengths as they propagate through tissue. The result is an apparent shift in the structures of OCT images taken at different center wavelengths. This, so-called, walk-off can be measured from the images using methodology shown in section 3.2.1 and so the GVD is calculated by equation 3.5. Due to the absence of distinct reflectors in tissues, it is practically impossible to implement the technique described above in vivo and in situ. However, the walk-off between two images, acquired at different center wavelengths, can be estimated from the cross-correlation of A-Scans from corresponding regions of the two images. As described in section 3.2.1, for Fourier Domain OCT images, each interferogram can be split into two

halves, forming two half-spectrum images at different center wavelengths (Figure 5.1 A). The cross-correlation of corresponding A-Scans is calculated and the first peak in the cross-correlation is detected. The walk-off is estimated from the distance of the peak from the zero lag location (Figure 5.1 B&C) and the GVD is calculated using the equation 3.5.

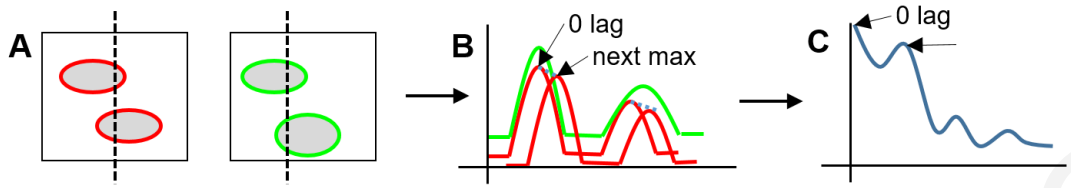

Figure 5.1. (A) Images reconstructed from the half spectra (red and green). (B) Corresponding A-Scans from the two half spectra images (red and green) indicating the lag at which there is a correlation peak. (C) The cross-correlation of the corresponding A-Scans

5.3 Experimental Methodology

5.3.1 *Ex vivo* GVD measurement based on the walk-off method

A swept source OCT system was used to image samples of porcine muscle, collagen gel and adipose tissue sections placed over a reflector which served as a reference for measuring the actual sample thickness and the resolution. Eight images were taken from different regions of each type of sample. Each interferogram was split into two halves (Figure 5.2) and two, half-spectrum, images were formed corresponding to different center wavelengths. To measure the walk-off, the shift of the reflector located behind the tissue was measured by locating its peaks in each image (Figure 5.2C, red and green lines). Using the location of the mirror, the actual thickness of the sample was also calculated as the distance between the top surface (Figure 5.2A, green line) and the extension of the mirror line (Figure 5.2A, blue line to the left). Based on these measurements, the GVD was estimated as the median of 250 measurements from individual A-Scans of each image. The standard deviation of the GVD of all images of each type was used as an estimate of the accuracy.

5.3.2 Application of the cross-correlation method to GI images

To demonstrate the applicability of the novel cross-correlation method to human tissues, the technique was applied to images from normal and cancerous colon obtained from patients who were scheduled for surgical excision. Eleven normal and fourteen abnormal images were included in this preliminary study. Since the actual tissue thickness could not be measured, it was estimated from the distance measured by OCT in air divided by an average index of refraction of 1.45 (error < 5%). The GVD was estimated up to a depth of approximately 0.5 mm (as measured in air) for 500 A-Scans per image (Figure 5.6). Using

the statistics of these GVD measurements (such as mean, standard deviation, etc.) the samples were classified as normal or abnormal using Linear Discriminant Analysis (LDA) and leave-one-out-cross-validation (LOOCV).

5.4 Results

The new proposed method was verified ex vivo using the same samples as in Chapter 4. Examples of the images collected are shown in Figures Figure 5.2Figure 5.3 and 5.4.

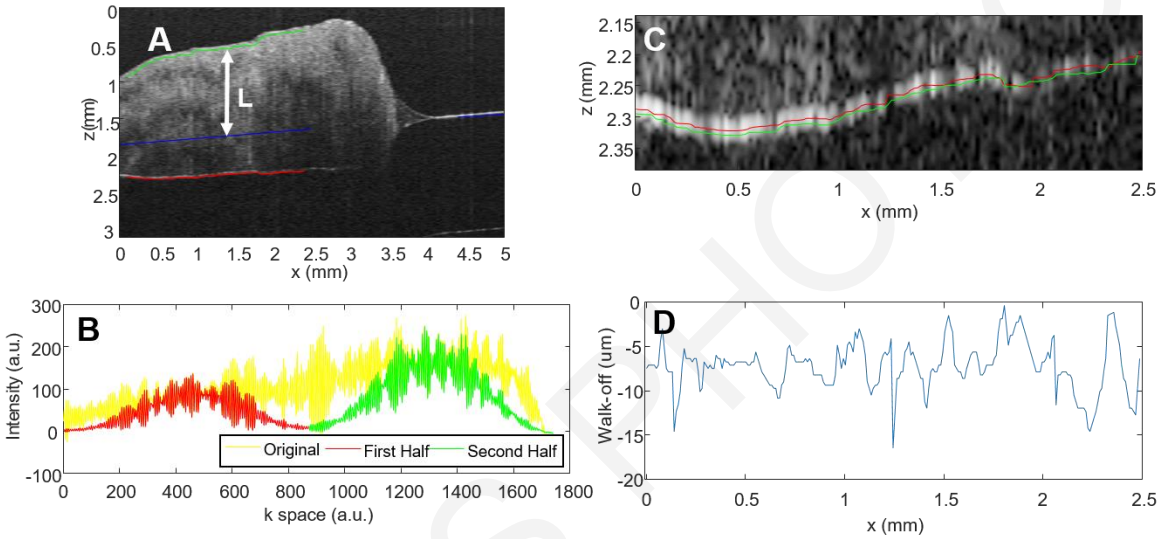

Figure 5.2. (A) OCT image of porcine muscle placed over a reflector (top surface: green, bottom surface: red, reflector: blue line, L: sample thickness). (B) A single interferogram (yellow) split into two halves (red and green). (C) The location of the bottom reflector from each half-spectrum image (red and green lines). (D) The walk-off between the two reflector locations.

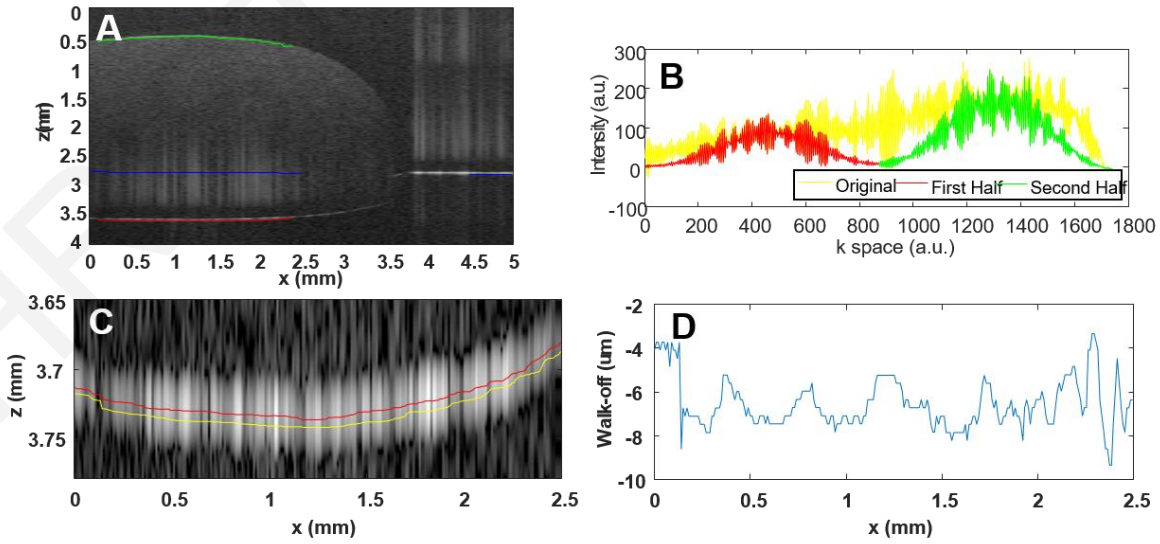

Figure 5.3. (A) OCT image of collagen placed over a reflector (top surface: green, bottom surface: red, reflector: blue line). (B) A single interferogram (yellow) split into two halves (red and green). (C) The location of the bottom reflector from each half-spectrum image (red and green lines). (D) The walk-off between the two reflector locations.

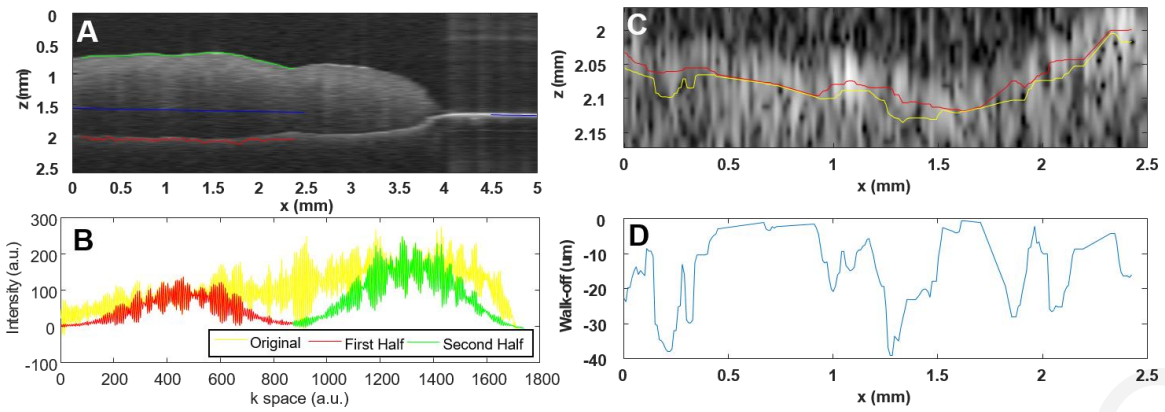

Figure 5.4. (A) OCT image of adipose tissue placed over a reflector (top surface: green, bottom surface: red, reflector: blue line). (B) A single interferogram (yellow) split into two halves (red and green). (C) The location of the bottom reflector from each half-spectrum image (red and green lines). (D) The walk-off between the two reflector locations.

As described in section 5.2.1, for Fourier Domain OCT images, each interferogram can be split into two halves forming two half-spectrum images at different center wavelengths. In the example of Figure 5.5, corresponding regions (just above the bottom of the sample) are selected from each half-spectrum image of Figure 5.2 (Figure 5.5 A&B). The cross-correlation of corresponding A-Scans is calculated and the first peak in the cross-correlation is detected. The walk-off is estimated from the distance of the peak from the zero lag location (Figure 5.5C) and the GVD is calculated using the equation 3.5. The walk-off estimation is more robust when there is enough speckle structure in the images to provide a better cross-correlation approximation. Figure 5.5D shows some typical cross-correlation curves with the arrow pointing to a miscalculation of the walk-off due to a weak cross correlation between A-Scans. This phenomenon is more common in clear samples such as the collagen gel used in the ex vivo experiments.

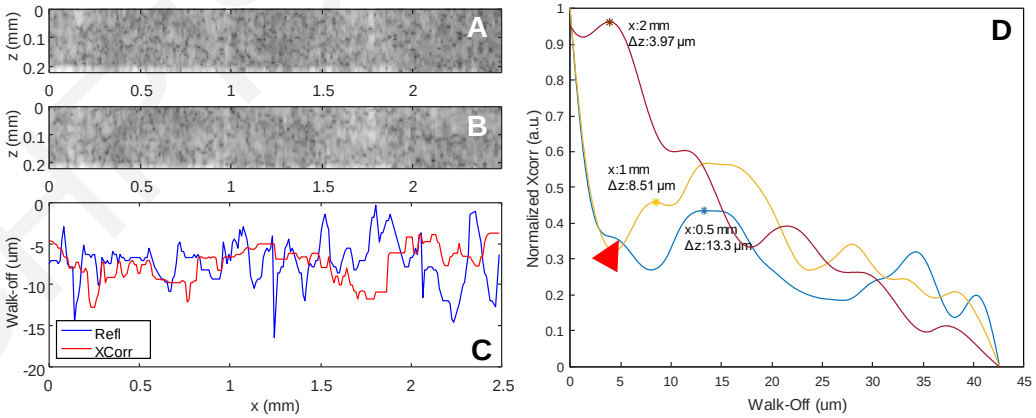

Figure 5.5. (A) Portion of the first half-spectrum OCT image from just above the bottom surface of the sample. (B) Similar portion from the second half-spectrum OCT image. (C) The walk-off for the 250 A-Scans in A & B calculated from the cross-correlation (red line). The blue line is the walk-off from Figure 5.4D. (D) Three indicative cross-correlation curves from different locations (x): 0.5 mm (blue), 1 mm (yellow) and 2 mm (red). The stars indicate the first maximum and the associated walk-off (Δz). The red arrow points to the location where the maximum should occur, which was missed due to weak cross correlation, a cause of error in the estimations.

Table 5-1. GVD measured from literature walk-off method and the cross-correlation technique described above. summarizes the results of the GVD measurements using the standard walk-off method from the literature (Section A) and the cross-correlation technique (Section C) described above. The values agree within one standard deviation (10-20 %) experimentally verifying the validity of the proposed technique. The proposed method accurate even for highly scattering tissues (less inter-sample variation) such as the adipose sample used here.

TABLE 5-1. GVD MEASURED FROM LITERATURE WALK-OFF METHOD AND THE CROSS-CORRELATION TECHNIQUE DESCRIBED ABOVE.

	Walk-Off (Reflector)			**Walk-Off Cross-Correlation**		
	Median (fs^2/mm)	**Inter-Sample Std (fs^2/mm)**	**Intra-Sample Std (fs^2/mm)**	**Median (fs^2/mm)**	**Inter-Sample Std (fs^2/mm)**	**Intra-Sample Std (fs^2/mm)**
Collagen	135.19	5.374	3.975	155.92	15.672	10.051
Muscle	136.60	18.64	13.64	139.96	23.484	16.779
Adipose	248.37	48.21	19.41	247.86	49.518	19.978

The GVD measurements from the normal and abnormal GI tissues exhibit statistically significant differences (Figure 5.7A & B). Combining the GVD distribution statistics using MANOVA results in perfect separation of the samples. Using the standard deviation of the GVD values, with LDA and LOOCV, the samples were classified with 100% sensitivity, 82 % specificity and 92% accuracy. One example of the classification scatter plot is shown in the Figure 5.7C).

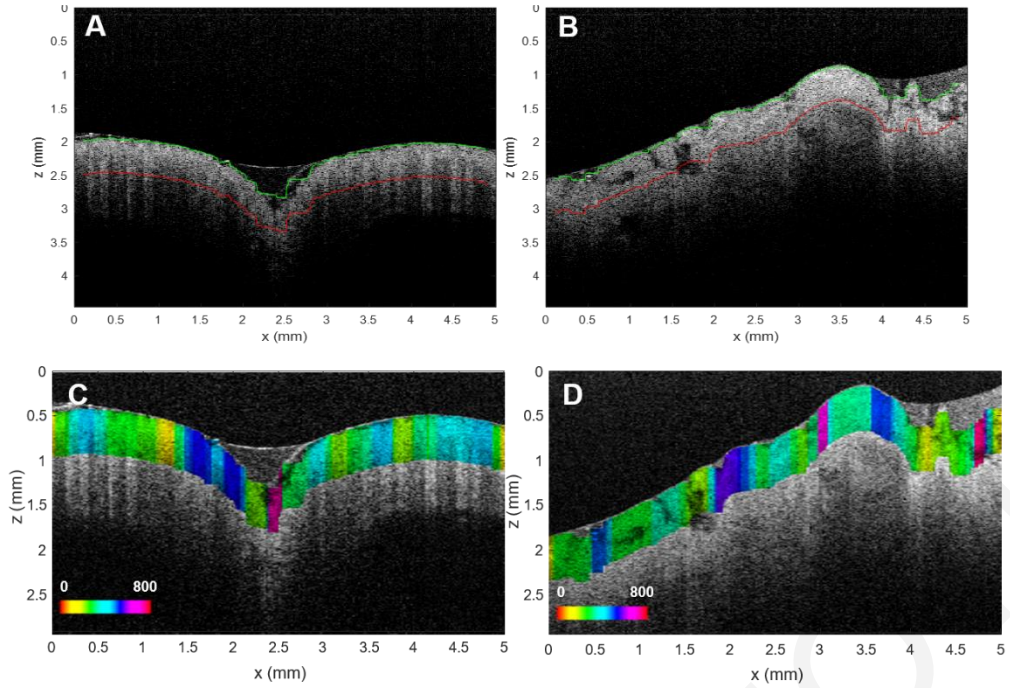

Figure 5.6. Normal (A) and abnormal (B) OCT images of human colon with the portion of the tissue used (green and red lines). Overlay of the images and GVD (pseudocolor hue, 0-800 fs^2/mm) for each A-Scan normal (C) and adenocarcinoma (D).

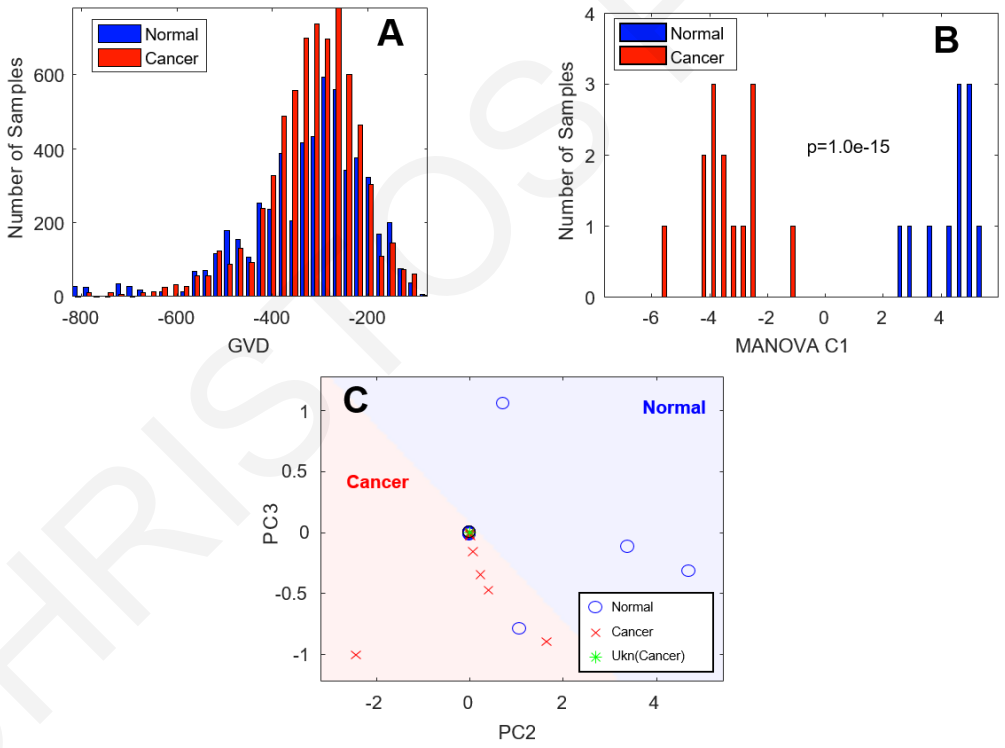

Figure 5.7. (A) Distribution of GVD measured from normal and abnormal colon tissue. (B) Distribution of the combined statistics (using MANOVA) for each sample. (C) LDA and LOOCV classification results. An unknown sample (cancer) was correctly classified.

5.5 Conclusion

Given the results presented above, the GVD can be effectively estimated from the walk-off, using cross-correlation, a technique not requiring distinct reflectors and, thus, applicable to any type of tissue *in vivo* and *in situ*. Such information could also be useful in the detection of tissue changes and could prove diagnostically useful. The success of these preliminary results indicates that further investigation is warranted, which should include both *ex vivo* and *in vivo* validation on a wider range of samples, to further elucidate the advantages and limitations of the proposed technique.

CHAPTER 6
COMPARISON OF TISSUE DISPERSION MEASUREMENT TECHNIQUES BASED ON OPTICAL COHERENCE TOMOGRAPHY

6.1 Summary

Dispersion effects in Optical Coherence Tomography (OCT) images have long been documented. As it was mentioned in Chapter 3, the imbalance of spectral broadening caused by dispersion mismatches in the two arms of the OCT interferometer, can result in significant resolution degradation. Group velocity dispersion (GVD) is also present in tissues and could be used to detect changes and provide useful information for diagnosis. This chapter presents a comparison between the existing methods used to measure the GVD from OCT images and the novel approaches developed as part of this thesis. The existing methods include: (i) the degradation of the point spread function (PSF), (ii) the shift (walk-off) between images taken at different wavelengths, (iii) the changes in the second derivative of the spectral phase (section 3.2.1). The two new methods which do not require a reflector and are applicable in intact tissues, are (iv) the speckle degradation (Chapter 4) and (v) the speckle cross-correlation (Chapter 5) approaches. A systematic, experimental, evaluation of these methods is presented to elucidate the capabilities, the limitations and the accuracy of each technique when attempting to estimate the GVD in scattering samples. The most precise values were obtained from the estimation of the PSF degradation whereas using the phase derivative method was only applicable to minimally scattering samples. Speckle broadening appears to be the most robust method for *in vivo* tissue GVD measurements [296].

6.2 Methodology - Results

For the experimental verification of the results and the comparison of the methods, a swept source OCT system, with a center wavelength of 1300 nm and a resolution of 12 μm in air was used. Samples of various glasses, collagen gel, porcine muscle and adipose tissue sections, *ex vivo*, were placed over a reflector, which served as a reference for the actual thickness and system resolution measurements, and eight images were acquired (5mm x 4 mm) from different regions for each type of sample. The glass samples were chosen so that they spanned a wide range of GVD values. Their well characterized properties were used to

verify the validity of the OCT techniques. The glass dimensions were 12.5 mm diameter and 2 mm thickness in all cases. The biological samples were chosen based on their scattering properties, ranging from minimal scattering (collagen) to very scattering (adipose tissue). The sample thickness varied between 1.5 to 2.5 mm as a result of being manually cut. However, since the actual thickness was measured for each lateral location (equation (3. 10),_ the thickness variation was included in the GVD calculation and did not affect the comparison. In Table 6-1 , a list of all the samples with the values of their index of refraction and GVD, obtained from the literature, is provided.

TABLE 6-1. SAMPLES USED FOR GVD ESTIMATION WITH REFERENCES VALUES FOR INDEX AND GVD

Type	Sample	n	GVD (fs^2/m)	Ref.
Glass	**BaF2 (2 mm)**	1.4724	18.663	[297]
	KBr (2 mm)	1.5506	62.942	[298]
	ZnS (2 mm)	2.3199	284.19	[299]
	ZnSe (2 mm)	2.4569	446.01	[299]
Biological	**Collagen Gel**	1.37 †	136 ‡	
	Porcine Muscle	1.42 †	137 ‡	
	Porcine Adipose Tissue	1.67 †	254 ‡	

† Experimental values measured using the technique of ref. [110].

‡ Experimental values defined as the average off all measurements.

The OCT data were processed in MATLAB. Initially, an automated algorithm detected the top surface of the sample as well as the mirror peak location in free-space and below the tissue. The tissue thickness, index of refraction, and mirror reflection Gaussian widths were subsequently calculated. From those measurements, the GVD was estimated for 250 A-Scans in each image. The GVD of each sample was taken as the median of the 250 values. The standard deviation of the GVD values obtained from the 8 images of each sample, as well as the mean error between the estimated and measured GVD were used as indicators of the precision and accuracy of each of the different methods described above. Furthermore, the standard deviation of the GVD measurements of single A-Scans within an image was used as a measure of each technique's robustness. Given that value, the minimum number of measurements that must be averaged in order to get a GVD estimate with an error, E, of 10% or less with a confidence level, α, of 95% was calculated by

$$n = \left(\frac{Z_{\alpha/2}\sigma}{E} \right)^2 \quad (6.\ 1)$$

where α = 0.05, E = 0.1, σ is the standard deviation, and $Z_{\alpha/2}$ = 1.96 is the critical value of the Normal distribution at $\alpha/2$. The results were compared, to evaluate the precision, accuracy and robustness of each method in the following Sections.

Figure 6.1 shows typical OCT images of the samples utilized in this study. Using the reflector location (blue lines) as reference, the sample thickness and the group index of refraction, at each lateral location, were calculated using the technique described in the literature using equation 3.10 [110].

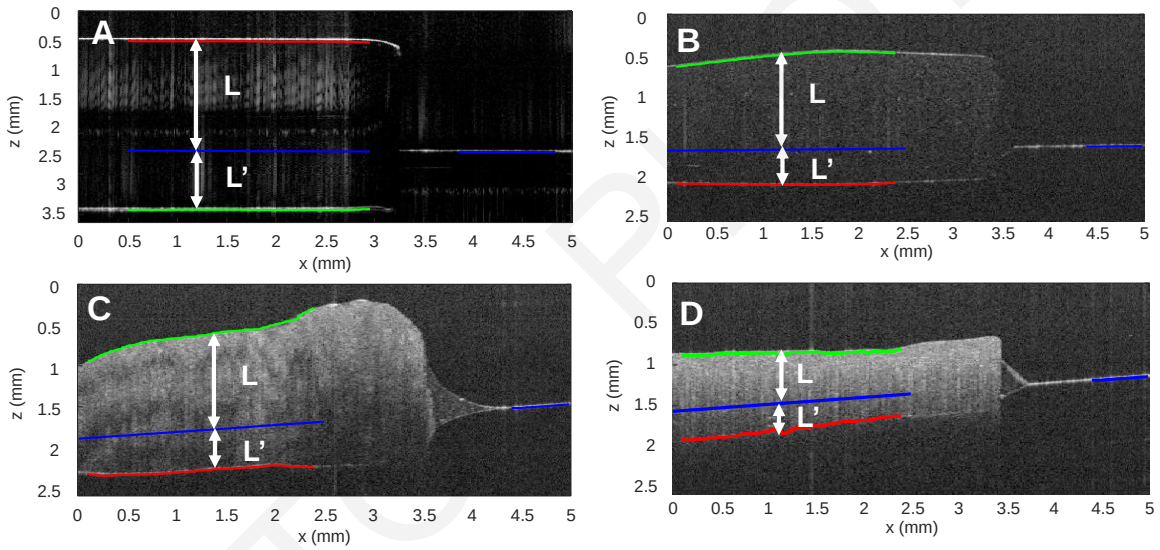

Figure 6.1. Typical OCT images used in this study. KBr glass (A), collagen gel (B), porcine muscle (C) and porcine adipose tissue (D), over a reflector. L is the actual sample thickness, from top surface (green) to the level of the reflector (blue). L' is the path-length difference, relative to air, because of the sample.

6.2.1 PSF degradation

Figure 6.2 is a typical example of how the PSF degradation is used to calculate the GVD. The width of the peak corresponding to a reflector placed below the sample (Figure 6.2A - red line) was measured from each image. The sample thickness, L, was measured from the top surface (Figure 6.2A – green line) to the reflector line extension (Figure 6.2A – blue line). Using equation 3.2, the GVD was calculated and overlaid over the OCT intensity image as a pseudo color hue scale. The same procedure was followed for collagen gel and adipose tissue as you can see in Figure Figure 6.3 and Figure 6.4.

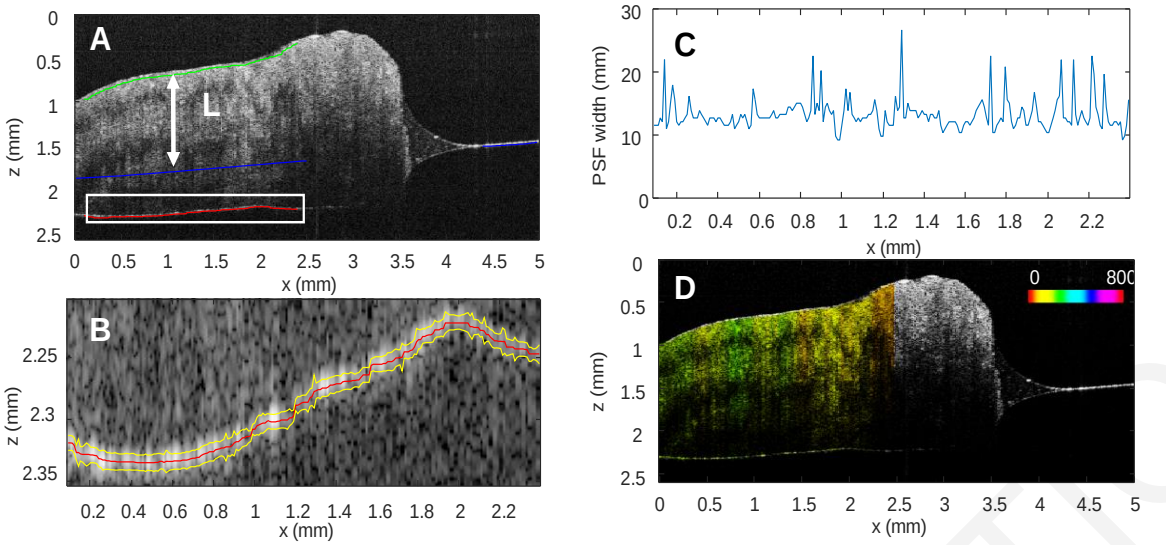

Figure 6.2. GVD estimation using the PSF degradation. (A) OCT image of porcine muscle. The top surface (green), reflector below the sample (red) and reflector (blue) are marked on the image. (B) The bottom surface (red) of the image in (A) with yellow lines marking the PSF width. (C) The PSF width measured from (B). (D) The OCT image of (A) with the GVD overlaid over the OCT intensity image as a pseudo color hue scale (0-800 fs^2/mm).

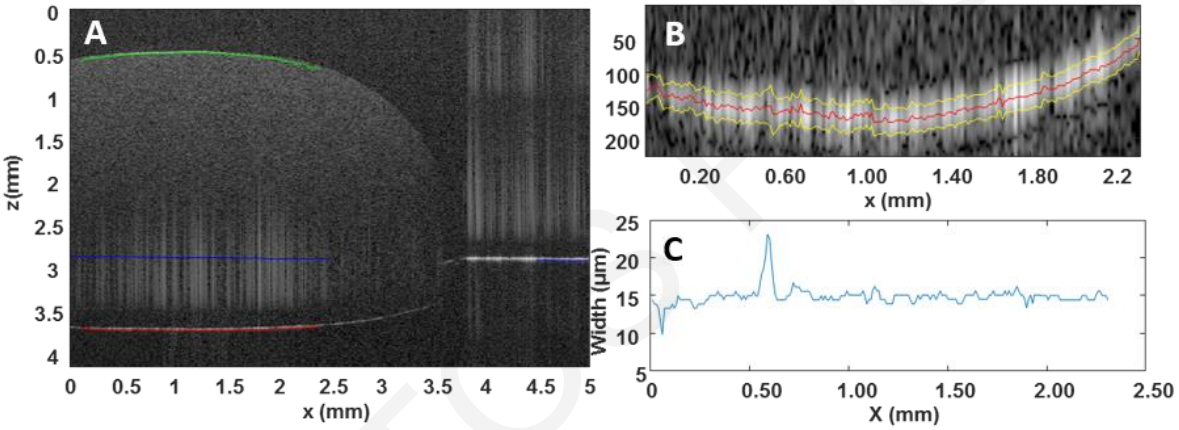

Figure 6.3. GVD estimation using the PSF degradation. (A) OCT image of collagen gel. The top surface (green), reflector below the sample (red) and reflector (blue) are marked on the image. (B) The bottom surface (red) of the image in (A) with yellow lines marking the PSF width. (C) The PSF width measured from (B).

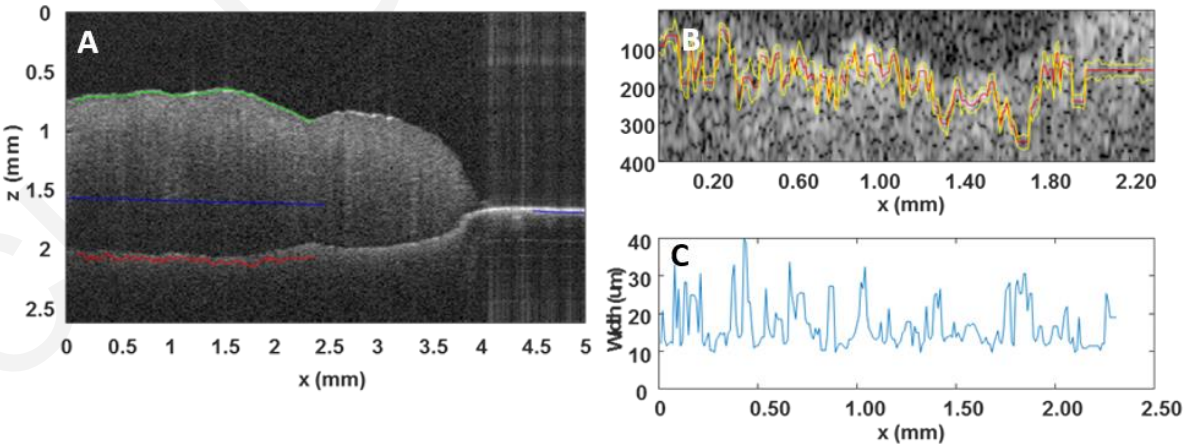

Figure 6.4. GVD estimation using the PSF degradation. (A) OCT image of adipose tissue. The top surface (green), reflector below the sample (red) and reflector (blue) are marked on the image. (B) The bottom surface (red) of the image in (A) with yellow lines marking the PSF width. (C) The PSF width measured from (B).

6.2.2 Walk-Off shift

At first, using the interferogram, the two half spectra were dispersion matched digitally, using non-linear interpolation, to assure that the resolution was the same and there was no walk-off in the absence of a sample, i.e. reflection from a mirror (Figure 6.5).

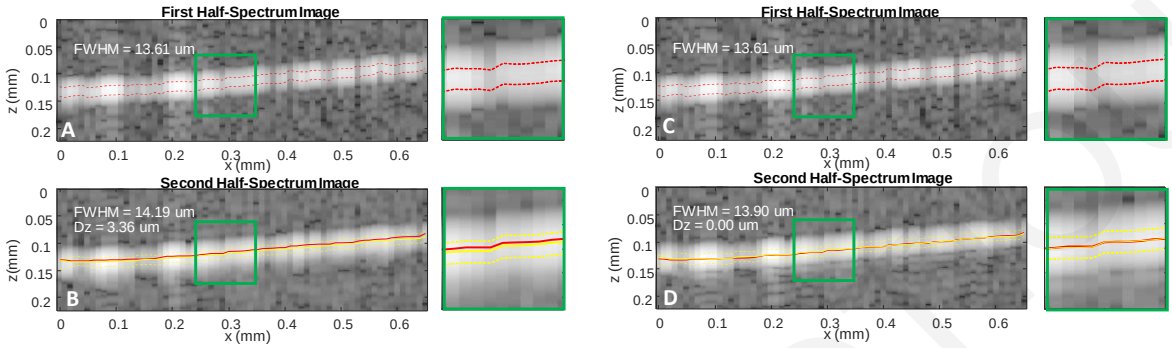

Figure 6.5. Images of a reflector constructed from the first (A) and the second (B) half spectra without digital dispersion compensation. The images to their right are zoomed regions indicated by the green squares. Images of a reflector constructed from the first (C) and the second (D) half spectra with digital dispersion compensation. The images to their right are zoomed regions indicated by the green squares. In all images, the FWHM (dashed lines) and the peak locations (solid lines) are marked for the first (red) and the second (yellow) half spectrum images. The FWHM and walk-off (Dz) are indicated for each case.

Figure 6.6 illustrates how the GVD was calculated experimentally using the walk-off. The interferogram (spectrum) was resampled and linearized and for each A-Scan (Figure 6.6A – green) divided into two parts (Figure 6.6A – red and yellow) by multiplying with Gaussian envelopes. Each half spectrum was used to create a separate OCT image (Figure 6.6 B&C). The walk-off (Figure 6.6 E), measured from the shift in the bottom surface (Figure 6.6 D – red & yellow) of the two images, was used to calculate the GVD from equation 3.5. The same procedure followed for porcine muscle and adipose tissue samples as you can see in FiguresFigure 6.7 Figure 6.8.

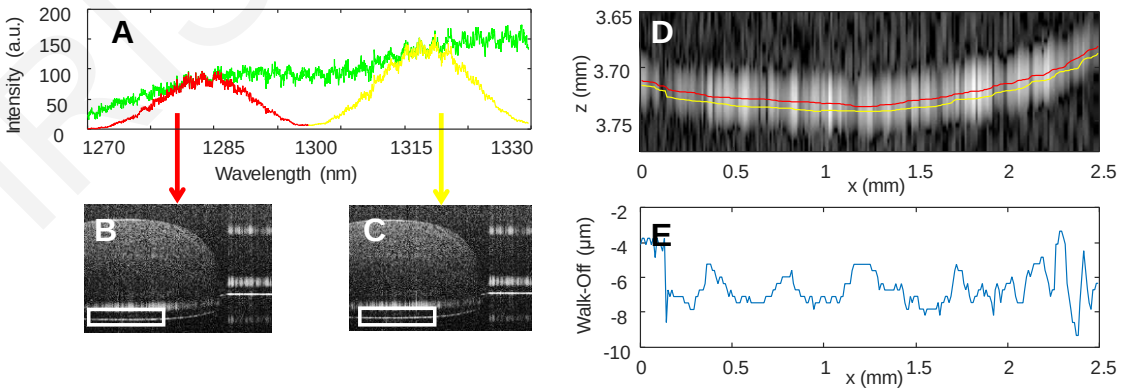

Figure 6.6. GVD estimation using the walk-off. (A) Interferogram from a single A-Scan from an OCT image of gelatin gel. The complete spectrum (green) was split into two halves (red and yellow) by multiplication with Gaussian envelopes. (B) & (C) The two OCT images created from each half spectrum. (D) The bottom surfaces from (B) (red) and (C) (yellow). (E) The walk off width measured from (D).

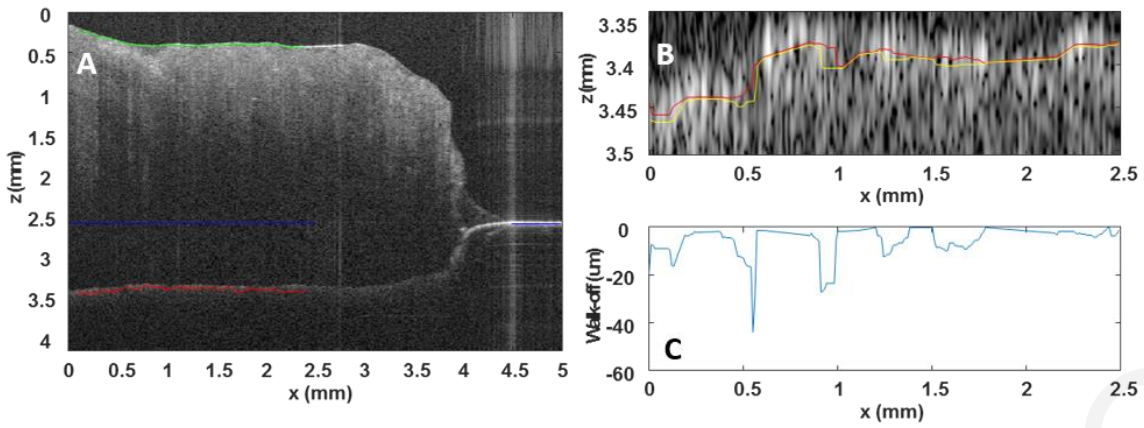

Figure 6.7. (A) OCT image of porcine muscle showing top surface (green), reflector below the sample (red) and reflector (blue) lines. (B) The bottom surfaces from images of different spectrum parts (red and yellow). (C) The walk off width measured from (B).

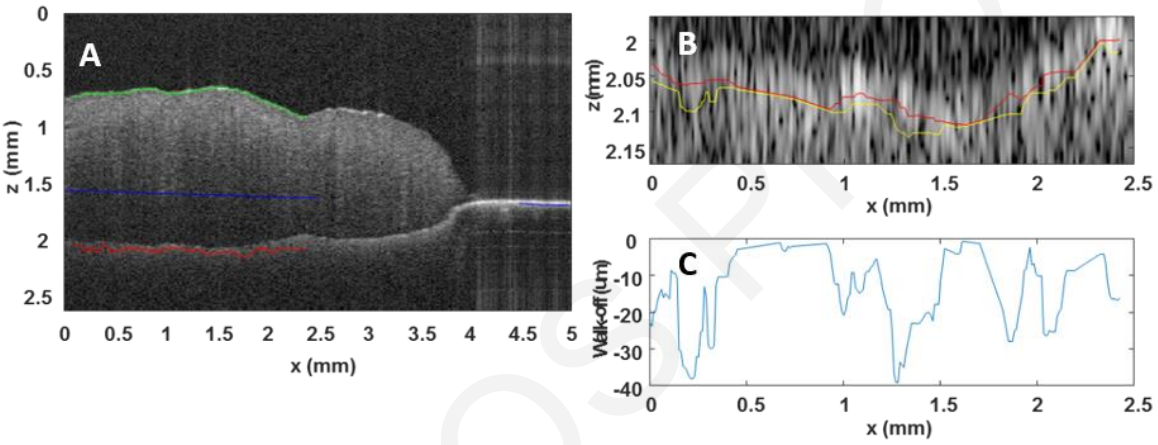

Figure 6.8 (A) OCT image of adipose tissue showing top surface (green), reflector below the sample (red) and reflector (blue) lines. (B) The bottom surfaces from images of different spectrum parts (red and yellow). (C) The walk off width measured from (B).

6.2.3 Phase Difference

Figure 6.9 is an example of the calculation of the GVD using the phase difference method. The real part of the Fourier transform of the interferogram of each A-Scan was used to isolate a single peak from a reflector below the sample (Figure 6.9B). The spectrum of the single peak was obtained from the inverse Fourier transform of the single peak (Figure 6.9C). Using equation 3.9, the GVD was calculated as a function of wavelength (Figure 6.9D).

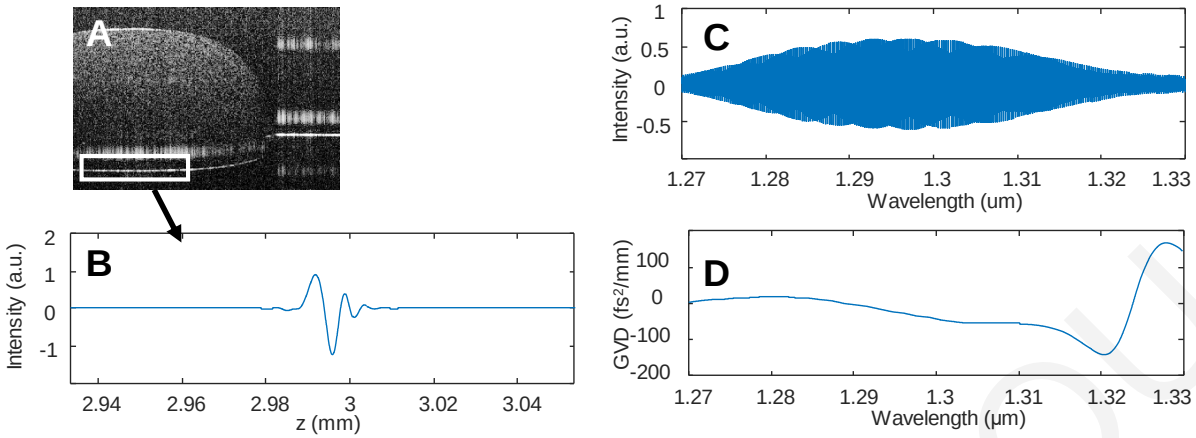

Figure 6.9. GVD estimation from the phase difference. (A) OCT image of collagen gel. The rectangle indicates the peak from a reflector below the sample. (B) The peak from the reflector, of a single A-Scan, isolated from the real part of the Fourier transform of the interferogram of that A-Scan. (C) The spectrum of the single peak obtained from the inverse Fourier transform of (B). (D) The GVD calculated from the second derivative of (C) as a function of wavelength for all A-Scans of (A).

The measurement of the |GVD| based on the phase derivative did not produce accurate results for highly scattering samples. This was due to the presence of strong discontinuities in the phase (Figure 6.10 B&E), as a result of the scattering discontinuities, producing erroneous GVD estimations (Figure 6.10, F). This is consistent with the literature, which predicts minimum and non-minimum phase discontinuities from Mie scatterers [109].

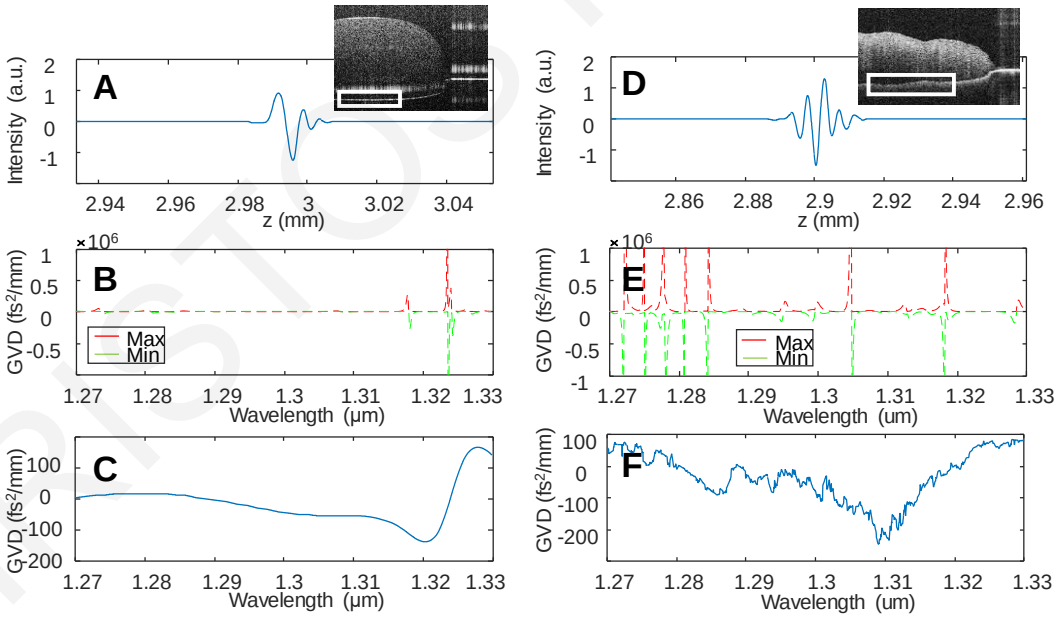

Figure 6.10. GVD estimation from the highly scattering samples resulting in erroneous GVD estimations. (A) OCT image of collagen gel and a single peak isolated from the interferogram of an A-Scan. (B) Max and min values of the GVD estimate indicating discontinuities. (C) The GVD of collagen as a function of wavelength for all A-Scans resulting in an accurate estimate. (D) OCT image of adipose tissue and a single peak isolated from the interferogram of an A-Scan. (E) Max and min values of the GVD estimate indicating discontinuities. (F) The GVD of adipose tissue (highly scattering) as a function of wavelength for all A-Scans resulting in an erroneous estimate.

6.2.4 Speckle width degradation

Figure 6.11 illustrates the application of the speckle-width-degradation-based approach to estimate the GVD from the OCT images. Portions of the image of from just below the top surface (Figure 6.11A – green lines) and just above the bottom surface (Figure 6.11A – red lines) with a width of twice the system resolution are shown as examples in Figure 6.11 A&B. The impulse response, *sdf*, was estimated with a Wiener-type deconvolution (Figure 6.11C) and the width of the *sdf* for all A-Scans was measured (Figure 6.11D). The process was repeated as a function of depth and the mean width, overall A-Scans, was calculated as a function of depth (Figure 6.11E). Subsequently, the dispersion-degraded image resolution width, d_d, was approximated from a linear fit of *sdf* mean width (Figure 6.11F). The GVD was calculated using d_d and equation 3.2.

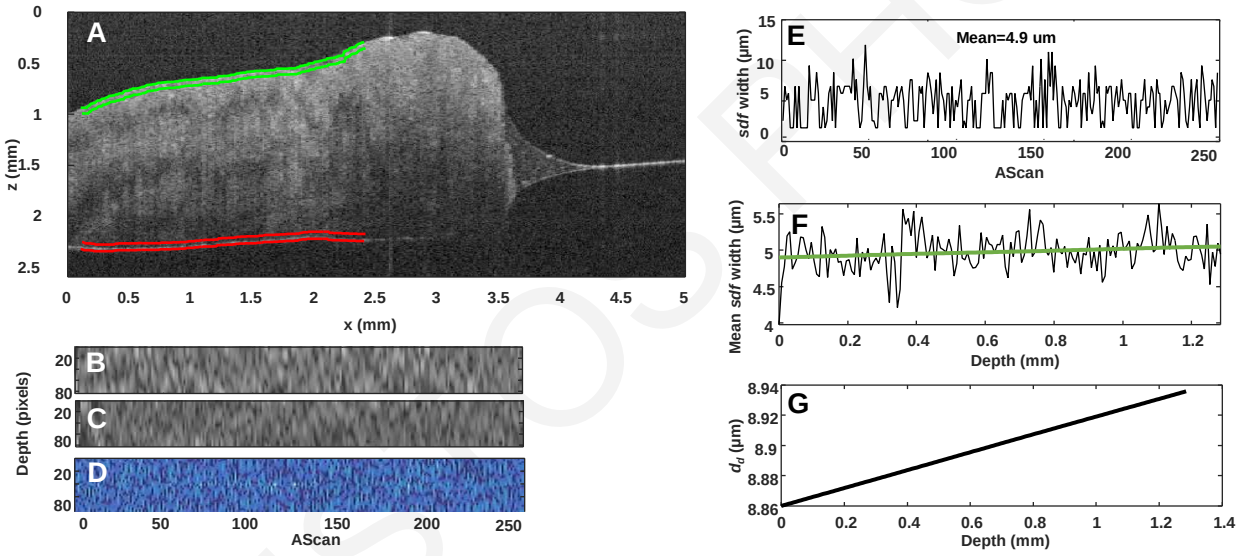

Figure 6.11. (A) OCT Image of porcine muscle. (B) Portion of the image (80x250 pixels) containing mainly speckle from just below the top surface (z = 0, green lines in A). (C) Similar portion from just above the bottom surface (z=L, red lines in A). (D) The result of Weiner deconvolution showing the speckle-PSF. (E) The width of the speckle-PSF for the 250 A-Scans in (D). (F) The mean speckle-PSF width as a function of depth with a linear fit (red line) illustrating the increase as a function of the depth. (G) The degraded Gaussian width as a function of depth calculated from the linear fit in (F).

6.2.5 Speckle cross-correlation

Figure 6.12 is an example of the estimation of the GVD from the walk-off shift of half-spectrum images using the cross-correlation of corresponding A-Scans. Corresponding regions, just above the bottom of the sample (Figure 6.12A – red Lines), were selected from each half-spectrum image (Figure 6.12 B&C). The cross-correlation of corresponding A-Scans was calculated and the first peak in the cross-correlation was detected. The walk-off

shift was estimated from the distance of the peak from the zero lag location (Figure 6.12D) and the GVD was calculated using the equation 3.5. The walk-off shift estimation was more robust when there was sample speckle in the images to provide a better cross-correlation approximation. Figure 6.12E shows some typical cross-correlation curves with the arrow pointing to a miscalculation of the walk-off shift due to a weak cross correlation between A-Scans. This phenomenon is more common in clear samples such as the collagen gel used in the *ex vivo* experiments.

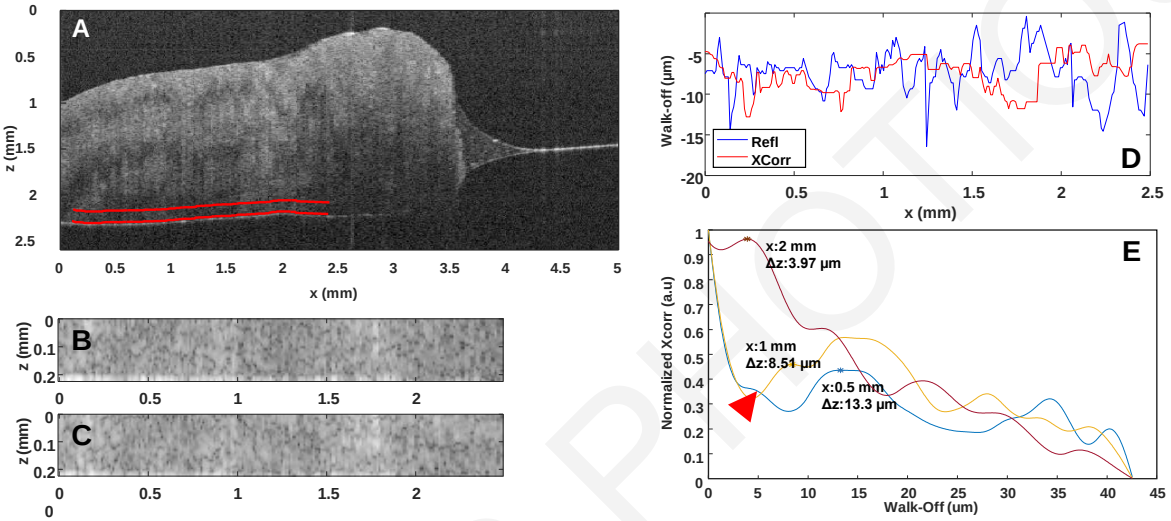

Figure 6.12. (A) OCT Image of porcine muscle. (B) Portion of the first half-spectrum OCT image from just above the bottom surface of the sample (A, red lines). (C) Similar portion from the second half-spectrum OCT image. (D) The walk-off of for the 250 A-Scans in A & B calculated from the cross-correlation (red line). For comparison, the walk off from Section 3.2 is also shown (blue line). (E) Three indicative cross-correlation curves with the walk-off (Δz) marked. The red arrow points to a missed maximum.

Table 6-2 summarizes the results of the GVD measurements using all the techniques described above. The left part of Table 6-2 lists the results of the GVD calculations over entire sample images, estimated from the median of the GVD of 250 A-Scans from each image. The accuracy of each technique (i.e. how close the results are to their expected values) for each different type of sample is evident from the % error difference from the expected values of Table 6-1 . Methods which are inaccurate are highlighted red in Table 6-2 . The precision of each technique (i.e. how concentrated the results are around their mean) is described by the standard deviation of the values of the results from complete images (average of 250 A-Scans). The right part of Table 6-2 lists the standard deviations of the GVD values from the individual A-Scans within each image. Larger values imply that more averages are required to get a good estimate of the GVD of the sample. This is also evident from the minimum number of averages required to get an estimate of the GVD with an error of 10 %, or less, with 95 % confidence which is listed in the last column of Table 6-2. Methods which are not robust are listed in red font. Further discussion of the results follows in the next section.

TABLE 6-2. EXPERIMENTAL AND STATICAL ANALYSIS RESULTS OF EVERY METHOD

		Complete Images (Average of 250 A-Scans)				Single A-Scan		
	Sample	Mean GVD (fs^2/mm)	Std GVD (fs^2/mm)	Std GVD (%)	Error (%)	Std GVD (fs^2/mm)	Std GVD (%)	Min Num of Avgs
PSF Degradation	BaF_2	17.89	0.030	0.166	4.126	3.665	20.483	16
	KBr	57.38	0.012	0.021	8.843	9.324	16.251	10
	ZnS	284.29	0.234	0.082	0.035	52.364	18.419	13
	ZnSe	445.33	0.000	0.000	0.153	47.383	10.640	4
	Collagen	135.72	5.775	4.255	0.206	11.879	8.753	3
	Muscle	136.97	16.621	12.135	0.024	23.747	17.338	12
	Adipose	253.58	31.986	12.614	0.167	58.193	22.949	20
Walk-off Shift	BaF_2	23.83	2.230	9.358	27.695	4.181	17.543	12
	KBr	66.41	5.671	8.539	5.517	16.278	24.509	23
	ZnS	279.03	22.106	7.922	1.817	41.966	15.040	9
	ZnSe	461.63	17.296	3.747	3.503	23.521	5.095	1
	Collagen	135.19	5.374	3.975	0.594	15.230	11.266	5
	Muscle	136.60	18.644	13.649	0.295	61.062	44.702	77
	Adipose	248.37	48.214	19.412	2.218	276.330	111.259	476
Phase Derivative	BaF_2	22.34	0.989	4.425	19.688	81.995	367.077	5176
	KBr	63.69	5.216	8.189	1.188	63.811	100.190	386
	ZnS	292.01	17.133	5.867	2.751	96.048	32.892	42
	ZnSe	454.77	9.633	2.118	1.964	182.321	40.091	62
	Collagen	136.47	6.047	4.431	0.348	386.650	283.315	3084
	Muscle	102.66	36.417	35.473	25.066	2579.897	2513.062	242616
	Adipose	43.61	27.595	63.280	82.831	12868.916	29510.448	33455208
Speckle Degrad.	Collagen	135.62	12.700	9.364	0.276	27.562	20.322	16
	Muscle	133.08	13.594	10.215	2.858	25.938	19.490	15
	Adipose	267.20	55.603	20.809	5.198	60.905	22.794	20
Speckle Walk-off	Collagen	155.92	15.672	10.051	14.650	30.360	19.471	15
	Muscle	139.96	23.484	16.779	2.163	34.716	24.803	24
	Adipose	247.86	49.518	19.978	2.419	81.501	32.882	42

Another important consideration, when calculating the GVD using OCT, is the size of the Fast Fourier Transform (FFT) to be used for the reconstruction of the images. In order to get a precise measurement of the degradation of the PSF or walk off, each peak in the OCT A-Scan must be adequately sampled to avoid sampling errors. The effect of the Fourier transform sampling on the GVD was estimated from the images acquired experimentally, by changing the measurements by ±1 pixel, and is shown in Figure 6.13A. These calculations

indicate that for a small sampling error, FFT sizes of 2^{18} or larger are required. This is further demonstrated by the effect of the FFT size on the actual GVD measurements (Figure 6.13B).

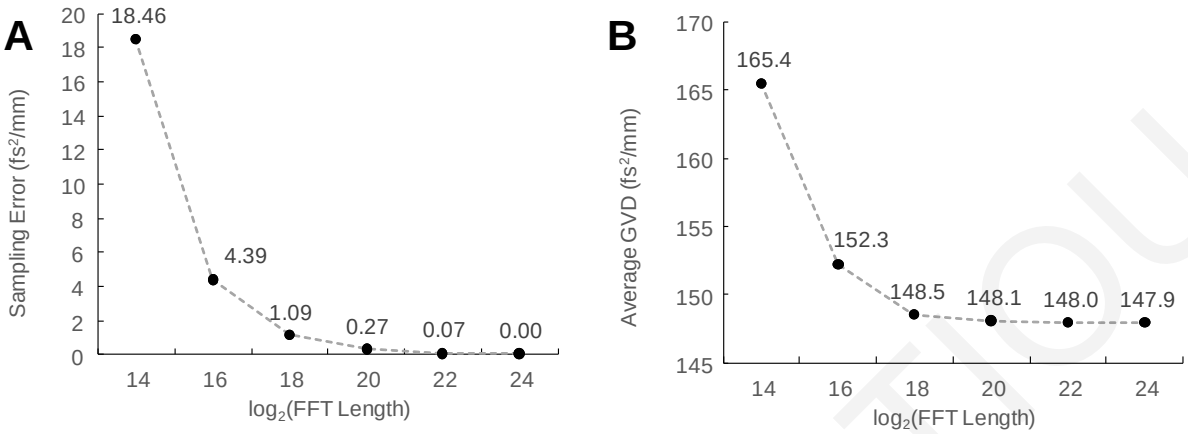

Figure 6.13. Effect of the FFT size on the accuracy of the results. (A) GVD sampling error resulting from the finite FFT size. (B) Accuracy of the GVD measurements as a function of the FFT size.

6.3 Discussion

All three mirror-based techniques performed well in low-scattering and fairly uniform samples, such as glasses or collagen gel, with the exception of BaF_2 which causes very low GVD. Based on these observations, only the PSF degradation method can be used to estimate GVD values below 20 fs^2/mm. The measurements from all gel samples were comparable and exhibited little variation (σ~4-6%). In muscle tissue, which is significantly more scattering, only the PSF degradation and walk-off shift methods produced sufficiently consistent results with σ ~12-14% while the phase derivative resulted in σ ~36%. The measurement of the width and walk-off shift were degraded by the presence of speckle noise. Finally, in adipose tissue, which is even more highly scattering, the PSF degradation and walk-off shift method results were accurate resulting in a σ of ~11-19 % while the phase derivative was completely wrong for the reasons described earlier. In general, the methods that did work were sufficiently accurate with an error always less than 10 %. The speckle based techniques were not as precise as the reflector based methods (σ~10-20%) but they are the only methods applicable to *in vivo* imaging. With the exception of the speckle walk-off method when applied to low scattering samples (collagen gel), the remaining estimates were accurate with an error ~0.3-5 %. In addition to the methods that result in erroneous estimates (described above and highlighted red in Table 6-2, there are other methods that are impractical due to the impractically high number of individual GVD values that must be averaged to get a good estimate of the GVD of the sample (red font in Table 6-2).

6.4 Conclusions

Group Velocity Dispersion (GVD) is present in all tissues and could potentially provide diagnostically useful information. OCT can be used to estimate the GVD and therefore enhance the possibility of early diagnosis of serious diseases such as cancer. Given the results presented above, for *ex vivo* GVD estimation, the PSF degradation method is the best choice since it is more tolerant to disturbances in measurements due to tissue scattering in contrast to the other techniques evaluated. This method performed particularly well for larger GVD's with an error of < 0.3 %. If the GVD is to be used to provide sensitive diagnostic information from highly scattering human tissues *in vivo*, it would be preferable to use the speckle degradation as an estimator of GVD. Given that tissue GVD is usually > 100 fs^2/mm this method is expected to perform well with an error of ≤ 5 %. Whichever the case, the use of the GVD as a disease marker is an exciting prospect which should be further investigated.

CHAPTER 7
DUAL-ANGLE OCT FOR INDEX OF REFRACTION ESTIMATION USING RIGID REGISTRATION AND CROSS-CORRELATION

7.1 Summary

There are many methods to measure the index of refraction, *n*, depending on the utilized imaging system or the experimental setup. Optical coherence tomography (OCT) has also been used in the past to measure the index of refraction especially *ex vivo*. However, the methodologies reported to date are not appropriate for *in vivo* imaging since they require either a mirror below the sample or an otherwise complicated imaging setup and algorithm. In this chapter, we propose a new measurement technique that could be deployed for *in vivo* estimation of *n*. This technique uses two OCT images obtained at different incidence angles. The path-lengths observed, in the sample, are different in the two images and directly depend on *n*. Measuring the path length changes and the incidence angles can provide an estimate of the index. The dual-angle method was validated experimentally using both clear and scattering samples. The resulting measurements of *n* were within a mean of ~1 % of the expected values. These initial results are promising and provide evidence that this method should be further investigated and validated on human tissues so that, in the future, it could be developed into a clinically useful diagnostic tool [300].

7.2 Methods and Results

7.2.1 Theory

The proposed technique is applicable to both scattering, e.g. tissue, and non-scattering, e.g. glass, samples. When a sample, of any kind, is horizontal, the light is incident on its surface perpendicularly and reaches the bottom of the sample without changing direction. The optical path-length (L_1) from the top to the bottom surface of the sample is equal to the sample thickness (d) multiplied by the index of refraction. If the incidence is at an angle, the beam is refracted and, as it passes through the medium, it follows a path-length (L_2) which is longer than that of perpendicular incidence (Figure 7.1A).

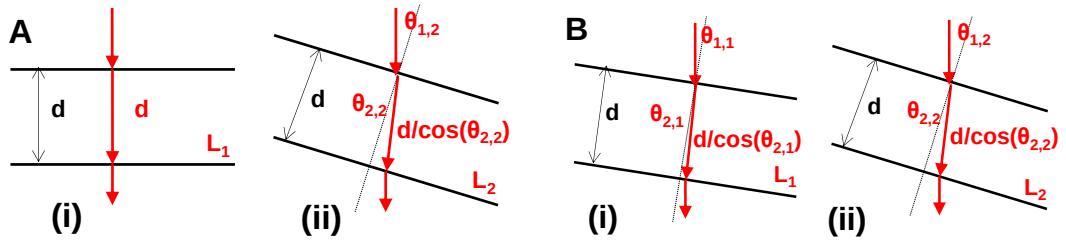

Figure 7.1. Incidence angles and path-lengths of beams perpendicular and at an angle to the samples. (A) Perpendicular (i) and at an incidence angle (ii) incidence on the sample. (B) Two samples with different incidence angles $\theta_{1,1}$ (i) and $\theta_{1,2}$ (ii).

Given that the path-lengths and incidence angles can be measured from the OCT images the index of refraction can be estimated, using Snell's law's, by:

$$\sin\theta_{1,2} = n\sin\theta_{2,2} \Rightarrow n = \frac{\sin\theta_{1,2}}{\sin\theta_{2,2}}$$

$$\left.\begin{aligned} L_1 &= nd \\ L_2 &= \frac{nd}{\cos\theta_{2,2}} \end{aligned}\right\} \Rightarrow \frac{L_1}{L_2} = \cos\theta_{2,2} \Rightarrow \theta_{2,2} = \cos^{-1}\left(\frac{L_1}{L_2}\right) \Bigg\} \Rightarrow$$

$$n = \frac{\sin\theta_{1,2}}{\sin\left(\cos^{-1}\left(\frac{L_1}{L_2}\right)\right)} \qquad (7.\ 1)$$

If the beams in both images are at an angle (Figure 7.1B), the equations become:

$$\left.\begin{aligned} &\sin\theta_{1,1} = n\sin\theta_{2,1} \Rightarrow \sin\theta_{2,1} = \frac{\sin\theta_{1,1}}{n} \\ &\sin\theta_{1,2} = n\sin\theta_{2,2} \Rightarrow \sin\theta_{2,2} = \frac{\sin\theta_{1,2}}{n} \\ &\left.\begin{aligned} L_1 &= \frac{nd}{\cos\theta_{2,1}} \\ L_2 &= \frac{nd}{\cos\theta_{2,2}} \end{aligned}\right\} \Rightarrow \frac{L_1}{L_2} = \frac{\cos\theta_{2,2}}{\cos\theta_{2,1}} = \frac{\sqrt{1-\sin^2\theta_{2,2}}}{\sqrt{1-\sin^2\theta_{2,1}}} \end{aligned}\right\} \Rightarrow \left(\frac{L_1}{L_2}\right)^2 = \frac{n^2-\sin^2\theta_{2,1}}{n^2-\sin^2\theta_{1,1}} \Rightarrow L_1^2\left(n^2-\sin^2\theta_{1,1}\right) = L_2^2\left(n^2-\sin^2\theta_{2,1}\right) \Rightarrow$$

$$n = \sqrt{\frac{L_1^2\sin\left(\theta_{1,1}\right) - L_2^2\sin\left(\theta_{1,2}\right)}{L_1^2 - L_2^2}} \qquad (7.\ 2)$$

The path-lengths (L_1 and L_2) can be measured directly from the images and the incidence angles ($\theta_{1,1}$, $\theta_{1,2}$) can also be measured directly from the angle of the top surface of the sample. This approach was verified by placing samples over a reflector so that the path-

length change could be easily measured and, at the same time, use the same reflector as a reference for estimating *n* with the technique described by Tearney et al, [110].

However, distinct, highly reflective, structures are rarely present in tissue. In order to apply this technique *in vivo*, a different approach is required to estimate the path-length change. This can be achieved by first registering and aligning the two images, with a rigid affine transformation, and subsequently using the cross-correlation of corresponding A-Scans from each image to estimate the path-length change for each A-Scan. Affine registration is an intensity-based linear mapping technique that does not affect points, straight lines and planes. It consists of scaling, rotation and translation and all pixels go through the same transformation. It is, usually, used to correct geometric distortions such as differences in the image size. The affine transformation can be described by:

$$\begin{aligned} x' &= t_x + a_1 x + a_2 y \\ y' &= t_y + b_1 x + b_2 y \end{aligned} \tag{7. 3}$$

where, t_x and t_y refer to the translation vector, x' and y' are the original points and a_1, a_2, b_1, b_2 are the affine transformation parameters [301].

After affine registration, the images are matched in rotation and translation. However, the second image is distorted, in depth, relative to the first, because of the elongation of the path-lengths due to the larger angle of incidence (Figure 7.2B). The cross-correlation is, therefore, expected to have maxima, first, at the 0 lag and then, again, at the lag which depends on the magnitude of this distortion. The path length change, ΔL, is estimated from the lag of this second maximum of the cross-correlation (Figure 7.2C). Since the path length of the second image, L_2, can now be calculated by the path-length change, i.e. $L_2 = L_1 + \Delta L$, the index is, then, calculated equation (7. 2) as:

$$n = \sqrt{\frac{L_1^2 \sin\left(\theta_{1,1}\right) - \left(L_1 + \Delta L\right)^2 \sin\left(\theta_{1,2}\right)}{L_1^2 - \left(L_1 + \Delta L\right)^2}} \tag{7. 4}$$

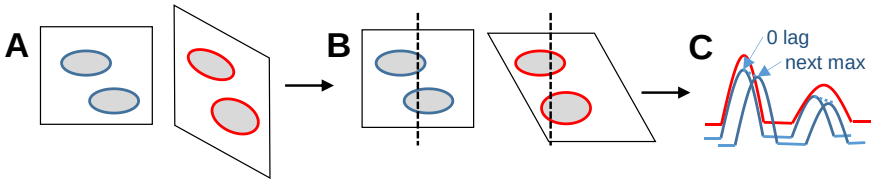

Figure 7.2. Path-length change estimate from two OCT images taken at different incidence angles. The images (A) are first registered and aligned (B). The cross-correlation of corresponding A-Scans from the aligned images exhibit distinct maxima (C).

A swept source OCT system, with 1.3 μm center wavelength and 12 μm resolution in air (Santec IVS 300), was used to image samples of glass, cucumber and rabbit trachea. The system operated at an A-Scan rate of 20 kHz and collected raw interferometric data corresponding to a physical size of 5 x 5 mm (512 x 2018 pixels). Each sample was placed on a vertically mounted rotation stage (0.01^o accuracy) which was rotated manually using a micrometer. For each sample, n and the sample thickness (L) were measured using the Tearney, et al, method [110], which served as the reference value. Subsequently, n was estimated from the path-length difference of the dual-angle images. To verify the technique, the mirror below the sample was initially used to measure the path-length changes. To prove the applicability of the technique to *in vivo* tissue imaging, the index of refraction was also calculated with the cross-correlation lag method. In this case, no mirror reflection was used. All methods were applied to the same sample images to assure that the results were comparable. The applicability of the proposed method was evaluated, first, on uniform, non-scattering, glass and, subsequently, higher scattering samples (cucumber) with more complicated structures and varying thicknesses and angles of incidence. The accuracy of the results was evaluated relative to the reference values. Images of glass, cucumber slices and freshly excised rabbit trachea were acquired at different incidence angles, ranging from 5^o to 20^o, with eight repetitions for each combination. The pivot point was set manually in the middle of the image for each measurement.

7.2.2 Results

Images of glass were acquired at different incidence angles, ranging from 5^o to 20^o, with eight repetitions for each combination, for a total of 48 images (Figure 7.3 A&B). The average results are shown in Table 7-1. When compared to the reference value of the index of the particular glass, n = 1.509, the error was 1.36%. The accuracy and precision of the path-length measurements were also evaluated from the glass measurements.

Imaging of thin cucumber slices followed, in an effort to examine the validity of the method in higher scattering samples (Figure 7.3 C&D). The average results, when using the reflector below the sample to measure the path-lengths, are also shown in Table 7-1. The estimated n, compared to the reference value, exhibited a mean error of ~0.7 % (varying from 0.5% to 2 %). The index of refraction was also determined using the cross-correlation method (Figure 7.4). The results are also shown in Table 7-1. When compared to the reference value, the error was ~1.1 % (varying from 0.1- 3 %). The accuracy and precision of the measurements of angle and distance were also evaluated from the OCT images of

glass. When measuring the angle, from various locations within the same image, the values did not vary by more than a standard deviation of 0.7°. In addition, the measured path length, within the same image, varied by less than 8 μm standard deviation. The accuracy of the measurements was evaluated by comparing to the expected path length, i.e. $L = nd / \cos\left(a\sin\left(\frac{\sin(\theta_1)}{n}\right)\right)$, and was found not to vary by more than 9 μm

TABLE 7-1. INDEX OF REFRACTION ESTIMATIONS USING BOTH METHODS ON SAMPLES WITH DIFFERENT SCATTERING PROPORTIES

	Reference		Path-length Changes Measured Using a Reflector				Path-length Changes Measured Using Xcorr			
	Mean	Std	Mean	Std	Error	% Error	Mean	Std	Error	% Error
Glass	1.509†	N/A	1.530	0.091	0.021	1.36	-	-	-	-
Cucumber	1.369‡	0.015	1.379	0.025	0.009	0.688	1.354	0.024	0.015	1.097
Rabbit Trachea	1.391‡	0.002	1.390	0.001	0.001	0.001	1.392	0.002	0.001	0.001

† Provided by the manufacturer.

‡ Measured using the method of Tearney et al, [110].

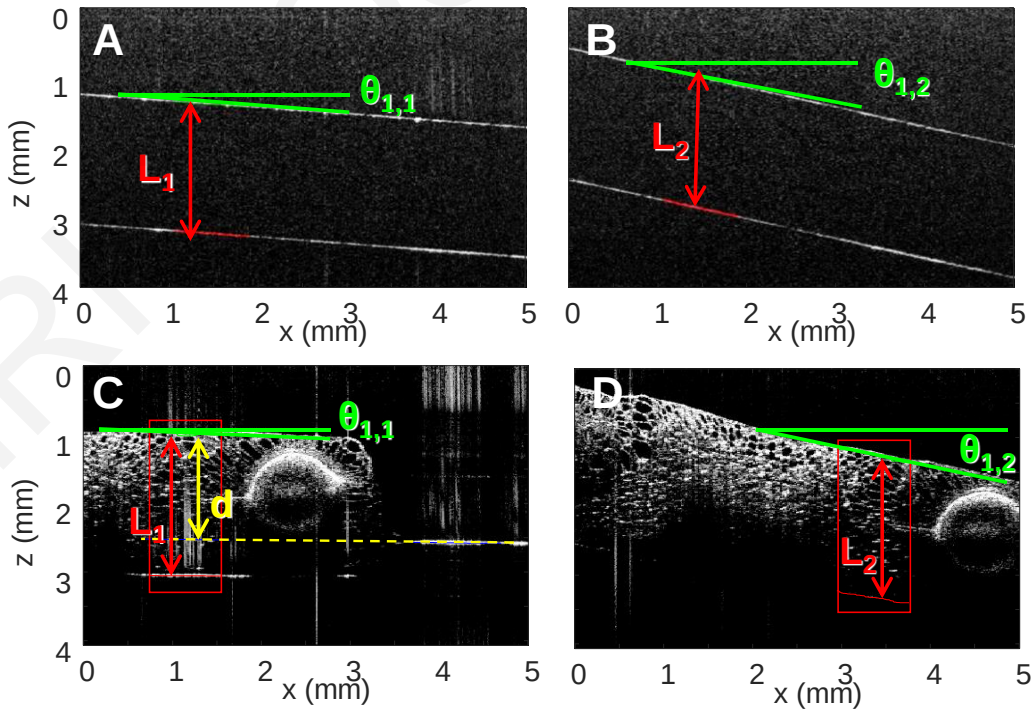

Figure 7.3. Images of glass (A&B) and cucumber (C&D). The angles $\theta_{1,1}$ and $\theta_{1,2}$ for the glass were 4.5 and 11.8 degrees, respectively, whereas for the cucumber, those angles were 0.9 and 12.2 degrees.*d* in (C) indicates the sample thickness.

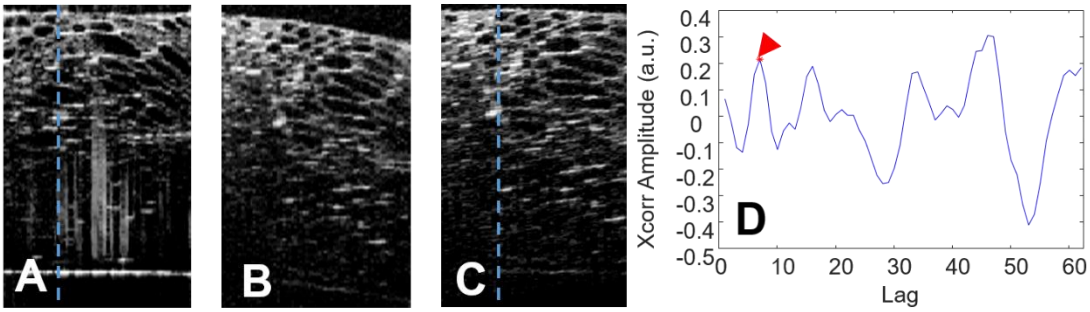

Figure 7.4. (A&B) Portions of the original OCT images of cucumber (Figure 7.3), at different incidence angles. (C) The registration of image B on A using rigid affine algorithm. (D) The cross-correlation of the A-Scans indicated by the dashed lines in A and C. The arrow points to the first maximum after the zero lag (not shown here for better visualization of the peaks).

Finally, in order to validate the applicability of the proposed technique to tissue samples, freshly excised rabbit trachea was imaged. The results are shown in Figure 7.5 and Table 7-1. The proposed methods perform equally accurately are the reference method.

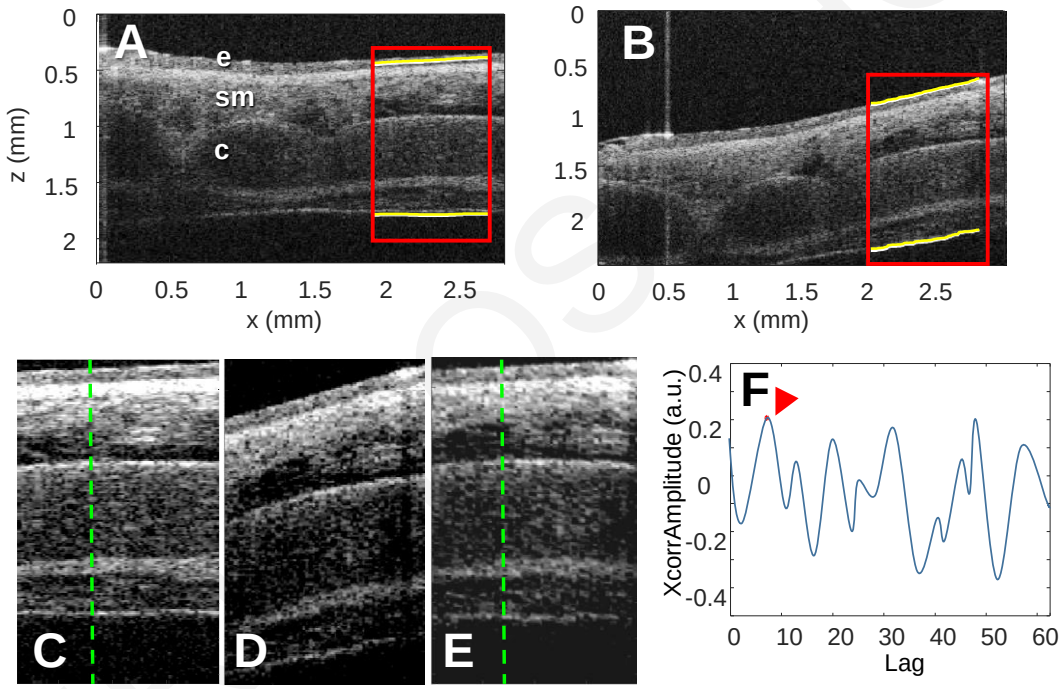

Figure 7.5. (A&B) The original OCT images of freshly excised trachea, at different incidence angles. The labels refer to the epithelium (e), the submucosa (sm) and cartilage (c). (C) The portion of image A. (D) Portion of image B. (E) The registered version of D. (F) The cross-correlation of the A-Scans indicated by the dashed lines in C and E. The arrow points to the first maximum after the zero lag (not shown here for better visualization of the peaks).

The variation in the error, reaching in some cases 3%, is explained by but also exemplifies the most serious limitation of the proposed technique, i.e. image misalignment. Misalignment by as little as ± 10 μm between the two images could lead to up to 5% error, as measured experimentally. This limitation should be taken into account and alignment should be carefully monitored especially when measuring the index of non-uniform samples. Fortunately, angle-resolved OCT systems, which are specifically designed to image the same

sample area under different incident angles, can provide angular and spatial precisions limited only by the precision of the galvanometric scanners. The performance of such systems has been validated for speckle reduction and results indicate that there is no resolution degradation implying negligible spatial shifts [302].

7.3 Conclusions

In this study, we propose a new measurement technique that could be deployed for *in vivo* estimation of *n*. This technique uses two OCT images obtained at different incidence angles and estimates *n* by measuring the path-length changes and the incidence angles. In tissues with no distinct reflectors, the path-length change can be estimated by first registering and aligning the two images, with a rigid affine transformation, and subsequently using the cross-correlation of corresponding A-Scans from each image. Experimental verification produced values of *n* with a mean error of ~1 % compared to the expected values. The main limitation of this technique is the effect of misalignment of the images on the results, which can lead up to 5% error for 10 μm misalignment. However, use of an angular resolved system should provide the precision required for the application of the proposed technique. These initial results are promising and provide evidence that this method should be further investigated and validated on human tissues so that, in the future, it could be developed into a clinically useful diagnostic tool.

CHAPTER 8
CLASSIFICATION OF BARRETS AND DYSPLASIA OF THE ESOPHAGUS USING IN VIVO OCT IMAGES

8.1 Summary

Endoscopic Optical Coherence Tomography (EOCT) systems can perform *in vivo*, real-time, high-resolution imaging of the human esophagus and, thus, play an important role in the earlier diagnosis and better prognosis of esophageal diseases such as Barrett's esophagus (BE), dysplasia and adenocarcinoma. However, the high image throughput and massive data volumes make manual evaluation of the generated information extremely difficult. Unfortunately, the algorithms, developed thus far, have not been able to provide effective computer-aided diagnosis. For the purposes of the thesis an automated algorithm was developed, capable of tissue segmentation and features extraction from regions of the epithelium, from *in vivo* EOCT images. Different machine learning methods for classification of esophageal tissue were also compared. The classification was based on several features, which included intensity-based statistics, group velocity dispersion (GVD) and the average scatterer size (SS) of each A-Scan. The areas of the epithelium were annotated as normal, BE or dysplasia by an expert. The comparison and evaluation of various machine learning (ML) techniques has shown that a neural network based approach provided the best performance, separating BE from dysplasia, for individual A-Scans, with an accuracy of 89% [303].

8.2 Introduction

Barrett's esophagus (BE) is a condition where the normal squamous epithelium of the esophagus transforms to columnar-like, due to gastroesophageal reflux. The frequency of adenocarcinoma in patients with BE is up to 35 times greater than the general population. Furthermore, over the last few decades, the incidence of BE is rapidly increasing in western countries. BE progresses through different stages of dysplasia before developing into esophageal adenocarcinoma thus providing a window for an early detection of the disease, which significantly improves patient prognosis. Patients with confirmed BE undergo

periodic endoscopic surveillance with systematic biopsies. However, this procedure suffers from important limitations. Sampling error can lead to misdiagnosis since only a small proportion of the metaplastic BE epithelium is covered by the biopsies (4-6% of the area) [80], [82]. Furthermore, the size and morphology of the samples obtained can cause diagnostic uncertainty since it limits inter-observer agreement between pathologists and causes delays in the histopathologic processing [304]. Endoscopic Optical Coherence Tomography (EOCT) systems can acquire cross-sectional images of the microscopic structure of the esophageal layers. By analyzing the microstructure of the epithelium in EOCT images, researchers aim to characterize the state of the esophageal tissue, discriminating between normal esophagus and BE with or without dysplasia [305]. Computational methods for the analysis of esophageal EOCT images have recently been demonstrated [81], [273]. In this study, different regions of esophageal EOCT images were classified utilizing a fully automated algorithm for image segmentation and feature extraction. Several ML classifiers were evaluated for accuracy and capability to differentiate normal from abnormal tissues and BE vs. dysplasia from *in vivo* data.

8.3 Methodology

8.3.1 Image and data processing

The OCT images were collected using a swept source EOCT system with a center wavelength of 1300 nm, an axial resolution of 10 μm and an A-Scan rate of 40 kHz. Each catheter rotation produced 2,048 A-Scan, displayed in real-time, and multiple cross-sectional esophageal images were collected as the catheter was manually pulled up from the gastroesophageal junction. *In vivo* data was derived from healthy volunteers and patients with esophageal disease enrolled in a study at Massachusetts General Hospital, approved by the Partner's Internal Review Board (IRB).

For this study, OCT esophageal images from ten patients creating a dataset of 320 images. The annotated regions were 461, of which, 170 normal, 118 BE and 173 dysplastic providing a total of 154066 annotated A-Scans. In order to extract features for image classification an automated algorithm for tissue segmentation and features extraction created and utilized to segment the epithelium. Each image was segmented at three different depths from the top surface of the tissue to investigate the setting for optimal classification results. The depth of segmentation was 0.4, 0.55, 0.7mm (Figure 8.1). The annotated regions were processed to extract features for the training and testing of the ML classifier models.

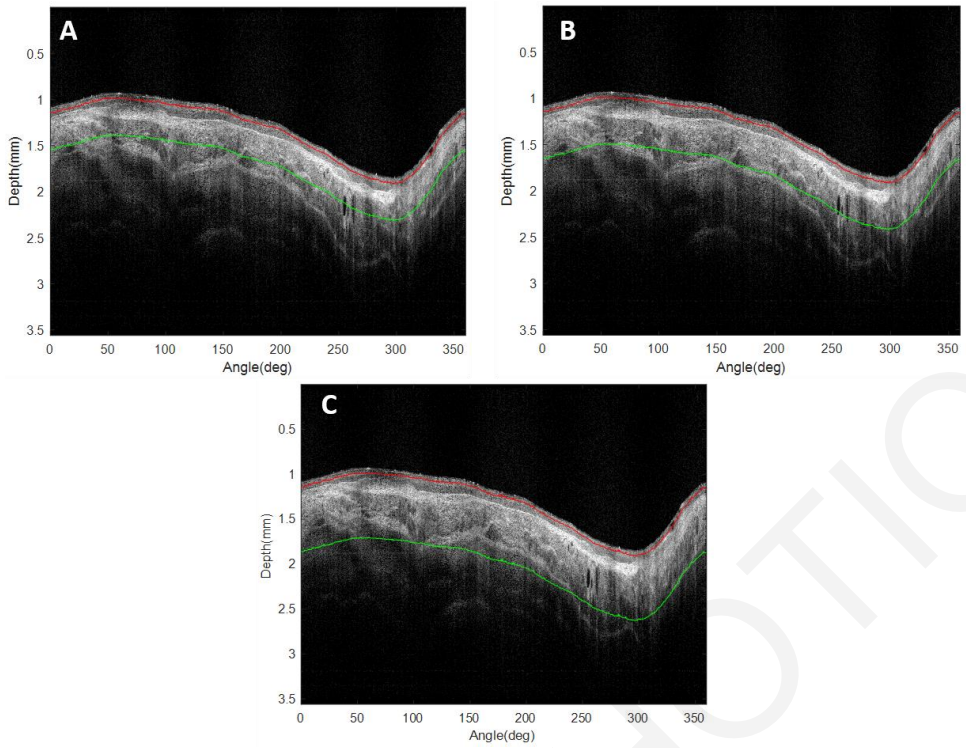

Figure 8.1. Esophagus OCT images in polar coordinates showing segmentation at different sizes of thicknesses (red and green lines). (A) 0.4 mm depth, (B) 0.55 mm depth and (C) 0.7 mm depth.

8.3.2 Feature extraction

The classification of the esophageal tissue was performed using various features extracted from the epithelial portion of the OCT images.

Intensity statistics

The statistics of the intensity of the OCT images were estimated for the portion of the OCT image that was segmented. At first, the statistics were calculated for each A-Scan separately for the upper and lower parts of the region's epithelium and then the region was also divided in three parts in order to more closely estimate the intensity differences between the basal layers and the luminal surface of the epithelium. The calculated statistics included the mean, variance, standard deviation, skewness, kurtosis, median, and the total, minimum and maximum intensities. In addition, the sliding standard deviation of every statistic, an estimate of the variation between the values of adjacent A-Scans, was also included. The result was a total of 36 intensity-based statistics for every A-Scan when the region was divided in half and 54 statistics when the region divided in three parts. The features were calculated separately for the top and bottom layer of the epithelium or alternatively for the top, middle and bottom layers.

Group velocity dispersion (GVD)

As mentioned in section 3.1, studies have shown that tissue dispersion could be used as a biomarker of early disease changes to enhance the diagnostic potential of OCT. Tissue dispersion of each region was estimated using the image's speckle, the technique that was developed and described in Chapter 4. It does not require the presence of distinct reflectors in the imaged tissue and is, therefore, applicable to *in vivo* imaging. This method compares the image speckle from different portions of the segmented area, beginning from the top surface of the epithelium and gradually progressing to the bottom. The GVD is calculated for each A-Scan from the speckle width degradation that is proportional to the point spread function (PSF) degradation.

Scatterer size (SS)

The average scatter size for each A-Scan of the epithelial layer was estimated using the bandwidth of the correlation of the derivative (COD) method. The COD is the new spectroscopic metric (described in section 3.6) that extracts information about the modulation of depth-resolved spectra and can be used to calculate the average scatterer size, as predicted by Mie theory. For each region of the epithelium, the spectrum was extracted using autoregressive spectral estimation. To estimate the scatterer size, the first derivative of the spectrum was calculated followed by its autocorrelation. The lag location of the first minimum of the autocorrelation was used to estimate the scatterer size using a function derived from curve fitting of the expected COD calculated from Mie Theory.

8.3.3 Feature selection and classification

In order to select the features that would yield the best classification results, feature selection and optimization was performed. This process included utilization of a paired t-test and Multivariate Analysis of Variance (MANOVA). Initially, each feature set was evaluated with a pair t-test to determine the p-value between Normal vs Abnormal tissue and BE vs Dysplasia (Table 8-1, Figure 8.2Figure 8.3). Subsequently various combinations of the features were combined with MANOVA to determine which resulted in the best class. After this process, the p-values for Normal vs Abnormal and BE vs Dysplasia were zero.

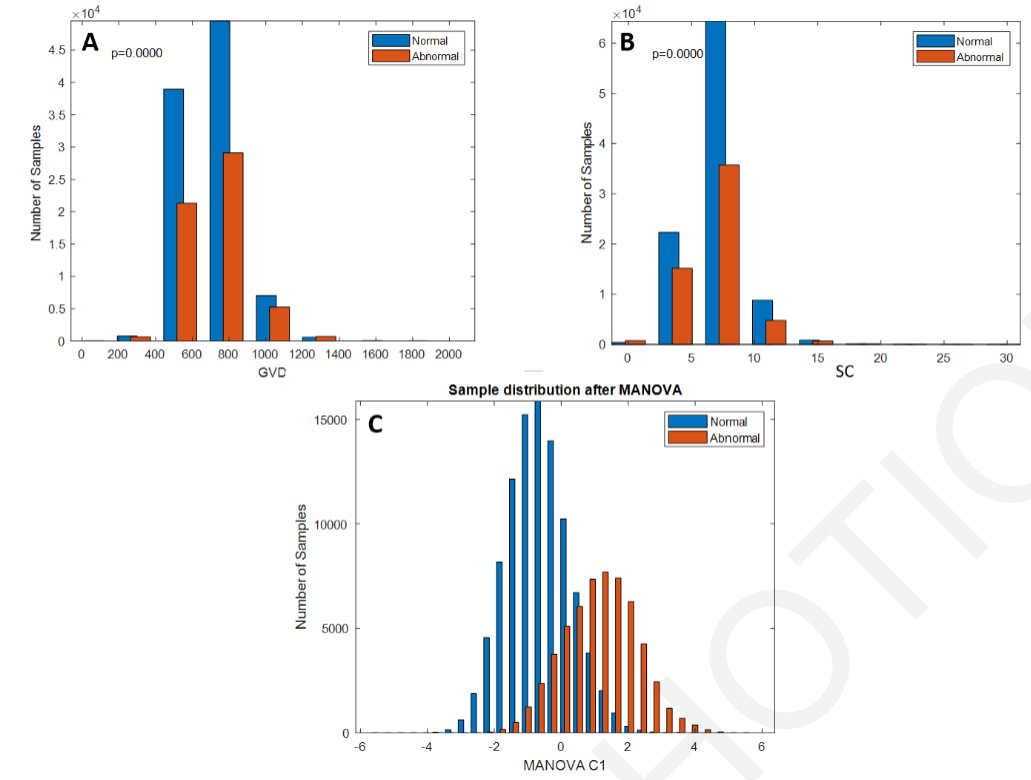

Figure 8.2. (A) and (B) T-test and p-value of group velocity dispersion (GVD) and scatterer size (SC) for Normal vs Abnormal regions classification among with recombination of the features values using MANOVA to represent statistical separation (C) for portion depth ~0.4mm and the region divided in half.

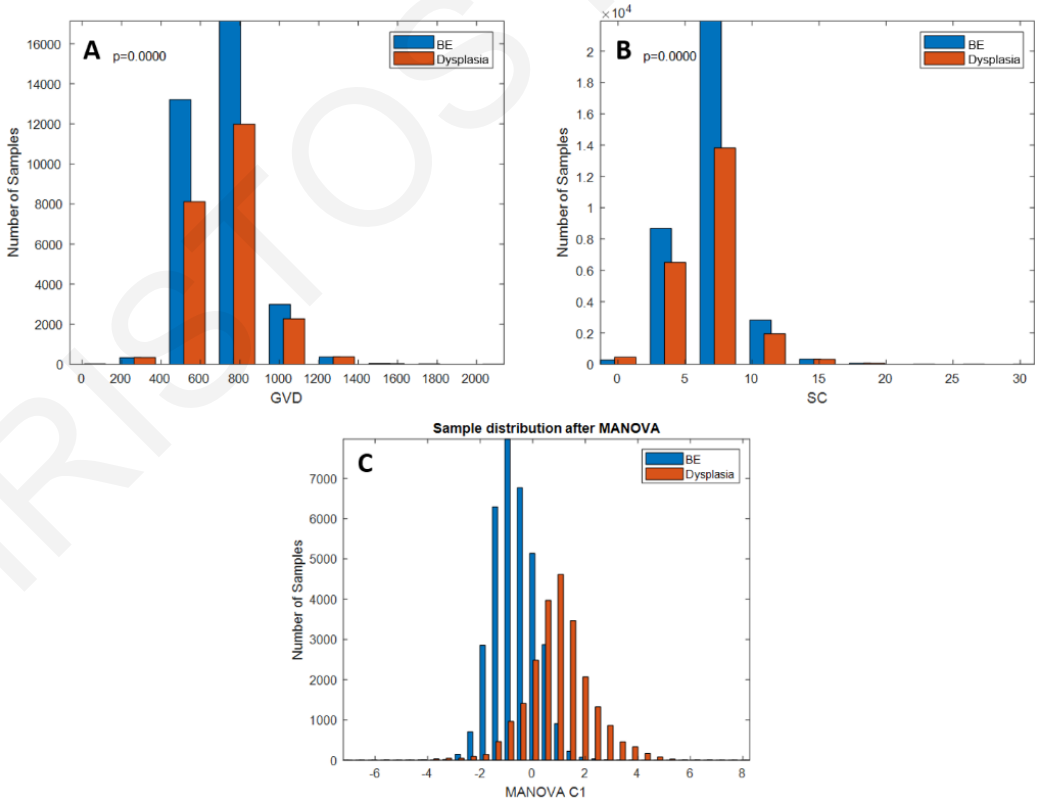

Figure 8.3. (A) and (B) T-test and p-value of group velocity dispersion (GVD) and scatterer size (SC) for BE vs Dysplasia regions classification among with recombination of the features values using MANOVA to represent statistical separation (C) for portion depth ~0.4mm and the region divided in half.

TABLE 8-1. P-VALUES OF THE MOST SIGNIFICANT FEATURES FOR EACH CLASSIFICATION TASK TOP (T), MIDDLE (M), BOTTOM (B) INDICATE THE PART OF THE EPITHELIUM.

Feature	Normal vs. Abnormal	BE vs. Dysplasia
Mean (T)/ Mean (B)	$4.8x10^{-4}$ / $4.34x10^{-4}$	$7.35x10^{-4}$ / $6.2x10^{-4}$
Variance (T) / Variance (B)	$4.94x10^{-4}$ / $2.19x10^{-4}$	$3.42x10^{-4}$ / $2.39x10^{-4}$
Median (T) / Median (B)	10^{-3} / $5.8x10^{-4}$	$2.4x10^{-3}$ / $2.9x10^{-3}$
Sum (T) / Sum (B)	$6.53x10^{-4}$ / $3.09x10^{-4}$	$7.38x10^{-4}$ / $2.72x10^{-4}$
Min (T) / Min (B)	$1.97x10^{-4}$ / $6.76x10^{-5}$	$1.77x10^{-4}$ / $4.09x10^{-5}$
Max (T) / Max (B)	$2.85x10^{-4}$ / $6x10^{-3}$	$1.65x10^{-3}$/ $3.4x10^{-4}$
Skewness (M)	$3x10^{-4}$	$1.13x10^{-3}$
GVD	$2.79x10^{-5}$	$2.59x10^{-4}$
SS	$3.49x10^{-4}$	$3.76x10^{-4}$

For the classification, five classifiers were initially evaluated using all features: Discriminant Analysis (DA), Naïve-Bayes (NB), Decision Trees (DT), *k*-nearest neighbor (KNN) and Ensemble of Decision Trees (EDT). The performance of each classifier model was verified using leave-one-patient-out cross-validation and was, subsequently, applied to entire images and volumes. Subsequently, using Python and Keras, different neural networks (NN) were constructed, varying the number of hidden layers and neurons, and each one evaluated on the same dataset. The optimal NN, consisted of 1 input,1 output and 7 hidden layers with a total of 3,643 trainable parameters. A Rectified Linear Unit (ReLU) was used as an activation function with a learning rate of 0,01 as an optimizer. Each neighborhood of the epithelium was classified first as normal vs. abnormal and, subsequently, the abnormal areas were classified as BE vs. Dysplasia. [306], [307], [308].

8.3.4 Experimental results

Figure 8.4 shows an example of an *in vivo* EOCT image of the esophagus. In real-time, the image is displayed in the standard Cartesian coordinates (Figure 8.4A) that represents more accurately the geometry of the esophagus. However, for processing purposes, the image was kept in polar coordinates (Figure 8.4B) so that individual A-Scans could be processed separately. The regions of the images in this dataset were annotated as normal, BE and dysplasia (Figure 8.4B, yellow boxes). The epithelium was automatically segmented using automatic appropriate morphological operations and thresh-holding, identifying the top and bottom boarders of the epithelium (Figure 8.4B, red and green lines). The segmented regions (Figure 8.4C) were used in the machine learning process.

Table 8-2 and Table 8-3 summarize the performance of all models for Normal vs Abnormal classification and Barrett's vs. Dysplasia, for every segmentation depth and for the region divided in two or in three parts. The performance of each classification scheme was verified using a leave-one-patient-out-cross validation for the same features selected based on t-testing and MANOVA (p-value <0.05). Mean, variance, median, sum, min and max of the upper and lower parts appeared to be the most significant features along with the GVD and SC. Only one feature of the middle area appeared to be significant (skewness) when the regions divided in three something.

Classification was performed utilizing the features of the whole epithelial region but the results where 1-2 % lower than the results when the epithelium was divided into layers. In addition, when median filtering was applied to the estimated class of the classifier the results improved from 0-1%. Furthermore, combining all the classifiers and considering as the class the one with the majority of occurrences did not affect the results significantly.

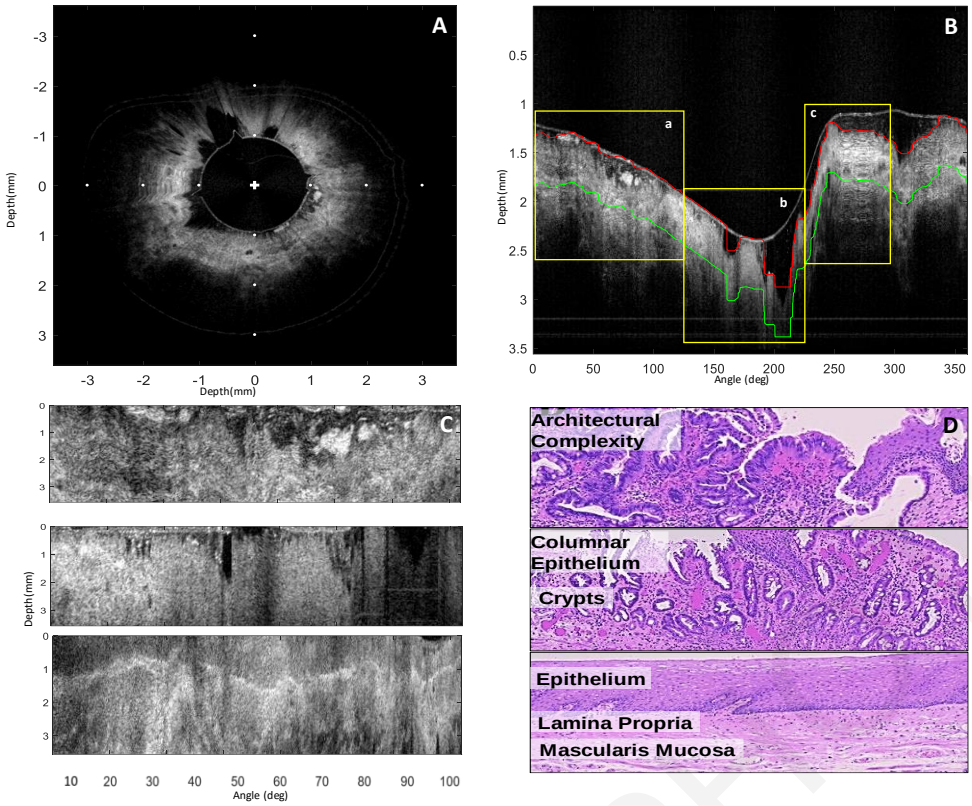

Figure 8.4. (A) In vivo OCT image of the human esophagus in Cartesian coordinates. (B) Same image in polar coordinates with the red and green lines indicating the top and bottom borders of the automatically segmented epithelial region (segmentation depth ~0.55mm). The yellow boxes indicate annotated dysplastic (a), BE (b) and Normal (c) regions. (C) Zoomed regions corresponding (from top to bottom) to the dysplastic, BE and normal annotated areas respectively. (D) Histopathologic sections (from unrelated samples) that illustrate the microstructural and nuclear changes associated with (from top to bottom) dysplastic, BE and normal esophageal tissue.

As it can be seen in Tables 8-2 and 8-3 and the charts in Figures 8.5 and 8.6, the classification results (specifically, sensitivity, AUC and accuracy) were superior when the features used for classification were extracted from each region (top and bottom) for both Normal vs. Abnormal and BE vs. Dysplasia. In addition, Normal vs. Abnormal classification was generally more challenging. Since this is a very preliminary study, improving the accuracy of the classifier was the major focus. The Linear discriminant analysis (LDA) classifier provided very good performance for Normal vs. Abnormal classification when the portion of the image segmented was 0,55mm from the top surface (sensitivity of 76%, specificity of 83%, accuracy of 81% and AUC of 0.80), but the neural network (NN) approach performed best (sensitivity of 67%, specificity of 95%, accuracy of 85% and AUC of 0.82) using 0.7mm segmentation depth. For BE vs. Dysplasia discrimination, which is more important for diagnostic purposes, the neural network (NN) again exhibited the best performance when the epithelium was segmented 0,4mm depth and divided in half with sensitivity of 80%, specificity of 91%, accuracy of 89% and AUC of 0.85. LDA had better sensitivity (81%) when the depth was 0.7mm but specificity, accuracy and AUC were 79%, 80% and 0.8 respectively.

TABLE 8-2. TABLES OF NORMAL VS ABNORMAL CLASSIFICATION RESULTS FOR EVERY SEGMENTATION DEPTH

L=0.4mm regions divided in half

Classifiers	SEN[%]	SPE[%]	ACC[%]	AUC	GM
LDA	75	80	80	0.78	0.78
k-NN	56	74	68	0.65	0.64
NB	63	77	72	0.70	0.70
EDT	60	88	77	0.73	0.72
DT	62	85	75	0.73	0.72
NN	72	92	84	0.78	0.80

L=0.4mm regions divided in three parts

Classifiers	SEN[%]	SPE[%]	ACC[%]	AUC	GM
LDA	70	75	73	0.72	0.72
k-NN	58	68	63	0.63	0.63
NB	69	68	69	0.69	0.66
EDT	67	74	71	0.70	0.70
DT	65	71	68	0.68	0.67
NN	68	86	78	0.75	0.77

L=0.55mm regions divided in half

Classifiers	SEN[%]	SPE[%]	ACC[%]	AUC	GM
LDA	76	83	81	0.80	0.79
k-NN	54	78	69	0.66	0.65
NB	66	79	74	0.73	0.72
EDT	61	88	78	0.74	0.73
DT	59	85	75	0.72	0.71
NN	67	94	84	0.70	0.80

L=0.55mm regions divided in three parts

Classifiers	SEN[%]	SPE[%]	ACC[%]	AUC	GM
LDA	68	74	71	0.70	0.71
k-NN	57	67	62	0.61	0.65
NB	59	72	66	0.65	0.65
EDT	63	74	69	0.69	0.68
DT	60	75	69	0.68	0.67
NN	65	87	77	0.70	0.75

L=0.7mm regions divided in half

Classifiers	SEN[%]	SPE[%]	ACC[%]	AUC	GM
LDA	66	85	78	0.75	0.75
k-NN	52	72	65	0.62	0.61
NB	64	81	75	0.73	0.72
EDT	53	88	75	0.70	0.68
DT	53	84	73	0.69	0.67
NN	67	95	85	0.82	0.80

L=0.7mm regions divided in three parts

Classifiers	SEN[%]	SPE[%]	ACC[%]	AUC	GM
LDA	67	75	72	0.71	0.71
k-NN	58	64	62	0.61	0.61
NB	61	77	70	0.69	0.69
EDT	60	77	69	0.68	0.67
DT	60	74	68	0.67	0.67
NN	79	78	79	0.69	0.79

TABLE 8-3 .TABLES OF BE VS DYSPLASIA CLASSIFICATION RESULTS FOR EVERY SEGMENTATION DEPTH

L=0.4mm regions divided in half

Classifiers	SEN[%]	SPE[%]	ACC[%]	AUC	GM
LDA	70	80	78	0.75	0.75
k-NN	70	70	72	0.70	0.70
NB	51	64	60	0.58	0.58
EDT	64	82	76	0.73	0.72
DT	65	76	73	0.70	0.70
NN	80	91	89	0.85	0.84

L=0.4mm regions divided in three parts

Classifiers	SEN[%]	SPE[%]	ACC[%]	AUC	GM
LDA	68	59	67	0.64	0.63
k-NN	59	54	56	0.56	0.56
NB	50	68	59	0.59	0.58
EDT	60	59	60	0.59	0.59
DT	58	56	57	0.57	0.57
NN	58	88	73	0.70	0.71

L=0.55mm regions divided in half

Classifiers	SEN[%]	SPE[%]	ACC[%]	AUC	GM
LDA	81	75	79	0.78	0.78
k-NN	78	71	74	0.75	0.75
NB	53	70	62	0.60	0.60
EDT	70	83	79	0.77	0.77
DT	67	78	73	0.73	0.72
NN	78	92	86	0.81	0.82

L=0.55mm regions divided in three parts

Classifiers	SEN[%]	SPE[%]	ACC[%]	AUC	GM
LDA	66	62	64	0.64	0.64
k-NN	58	58	58	0.58	0.58
NB	53	57	55	0.55	0.55
EDT	56	65	60	0.60	0.60
DT	56	59	57	0.57	0.57
NN	58	88	73	0.70	0.71

L=0.7mm regions divided in half

Classifiers	SEN[%]	SPE[%]	ACC[%]	AUC	GM
LDA	81	79	80	0.80	0.80
k-NN	81	67	73	0.74	0.73
NB	62	72	68	0.67	0.67
EDT	71	86	80	0.78	0.79
DT	70	76	73	0.73	0.72
NN	72	93	85	0.81	0.82

L=0.7mm regions divided in three parts

Classifiers	SEN[%]	SPE[%]	ACC[%]	AUC	GM
LDA	64	60	62	0.62	0.62
k-NN	56	60	58	0.58	0.58
NB	60	59	60	0.60	0.60
EDT	57	62	60	0.60	0.60
DT	57	56	57	0.57	0.59
NN	66	81	73	0.72	0.73

Figure 8.5. Classification results of Normal vs. Abnormal discrimination when the epithelium was divided in half (Top) and when the epithelium divided in three parts (Bottom) for each classifier and different segmentation depths.

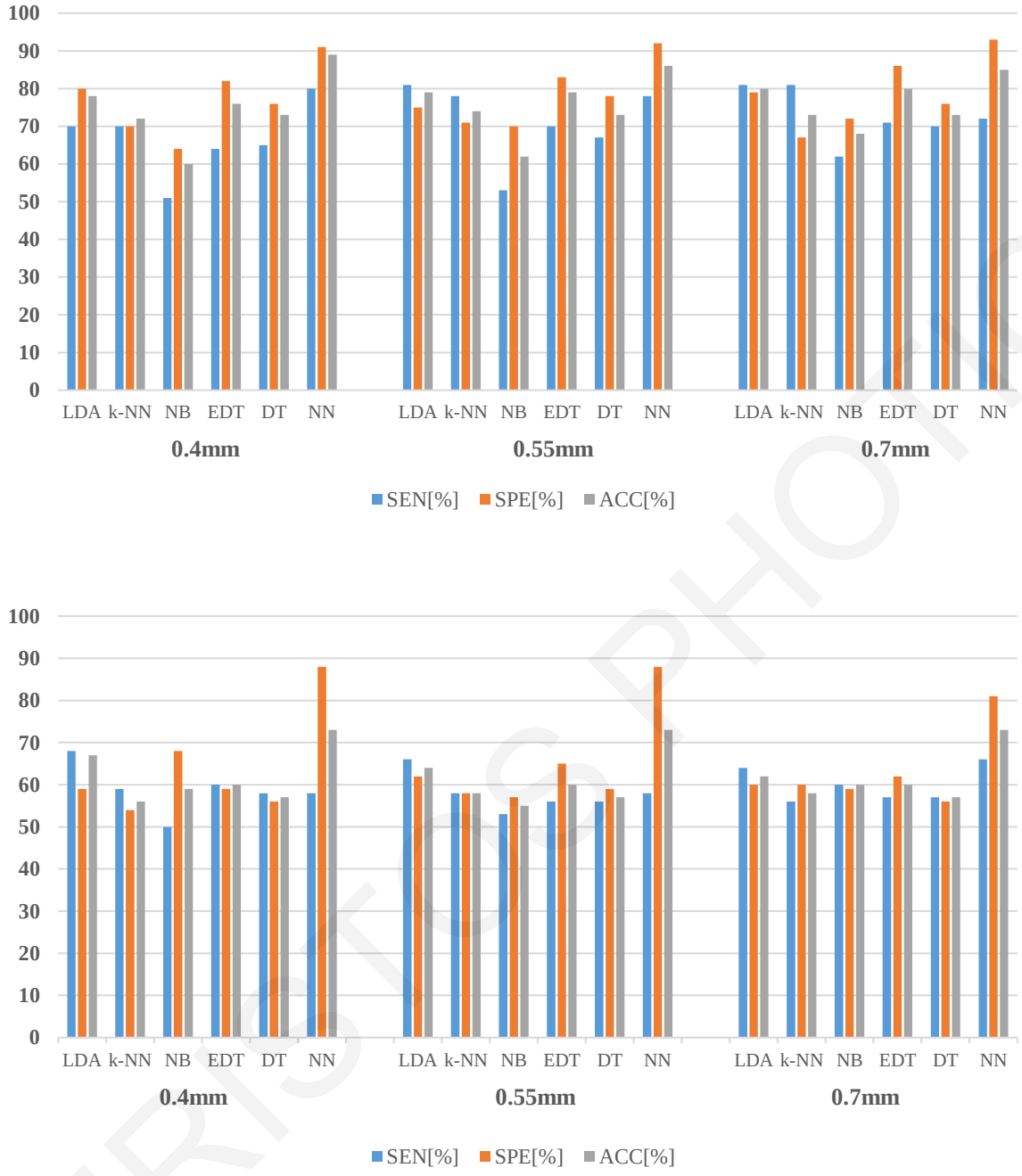

Figure 8.6. Classification results of BE vs. Dysplasia discrimination when the epithelium divided in half (Top) and when the epithelium divided in three parts (Bottom) for each classifier and different segmentation depths.

8.3.5 Conclusions

Given the results presented above, the automated algorithm proposed could be developed to perform *in vivo* EOCT esophageal tissue segmentation and classification. Using machine learning with a neural network, the algorithm could distinguish Barrett's esophagus (BE) from Dysplasia with an accuracy of 89%, sensitivity of 80% and specificity of 92% with AUC 0.85. Segmentation depth of 0.4mm to the esophagus epithelial layer appears to best more appropriate for BE vs. Dysplasia classification and Normal vs. Abnormal. Furthermore, it is clear from the results that the division of the epithelial region in half (top and bottom) during feature extraction led to more effective classification. However, further evaluation is required, with a larger number of images from more patients, to optimize the classifier models and create a system that can be used for effective computer aided diagnosis of EOCT images.

CHAPTER 9
CONCLUSIONS AND FUTURE WORK

9.1 Conclusions

This dissertation concentrated on novel feature extraction from OCT images and Machine Learning (ML) methods for the classification of esophageal malignancies from endoscopic OCT. Novel methods, which can be used to estimate the Group Velocity Dispersion (GVD) and the index of refraction (*n*) of tissues *in vivo* and *in situ* were developed. These and additional features were studied and evaluated for their ability to improve tissue classification, using a variety of ML approaches, to enhance the diagnostic capabilities of OCT.

The GVD variations that exist between normal and abnormal tissues were shown to be important in the detection of changes associated with early disease. However, most existing methods to estimate the GVD from OCT images are not applicable *in vivo*. Two novel techniques proposed in this Thesis could remedy this problem. First, the speckle degradation method that can be used to estimate the resolution degradation from the speckle pattern. This new approach was shown, experimentally, to be very robust in estimating the GVD with results comparable to the standard techniques, described in the literature, for both low and highly scattering samples. In addition, it is sensitive enough to discriminate dispersion changes between normal and cancerous tissues. Furthermore, another promising method was presented to effectively estimate GVD from the walk-off, using the cross-correlation of corresponding A-scans from OCT images created separately from the two spectral halves of the source spectrum. The success of these preliminary results indicates that further investigation is warranted, which should include both *ex vivo* and *in vivo* validation on a wider range of samples, to further elucidate the advantages and limitations of the proposed techniques.

The variations of the index of refraction have also been investigated for diagnostic purposes since they can reflect disease and cell dynamic changes. OCT has been used in the past to measure *n ex vivo*. In this Thesis, a new method was developed, which can be deployed *in vivo* and *in situ*. It utilizes two OCT images obtained at different incidence angles and estimates *n* by measuring the path-length changes and the incidence angles from

the OCT images. It exploits rigid image registration and the cross-correlation of corresponding A-Scans in the two images to do so. The main limitation of this method is the effect of misalignment of the images on the results, which can result in up to 5% error for 10 μm misalignment. However, the use of an angular-resolved system should provide the precision required for the successful application of the proposed technique. These initial results are promising and provide evidence that this method should be further investigated and validated on human tissues so that, in the future, it could be developed into a clinically useful diagnostic tool.

Finally, an automated algorithm for image segmentation, feature extraction and classification of *in vivo* OCT images of the human esophagus was deveoloped. By combining different features, several ML algorithms were compared for their ability to discriminate various regions of the human esophagus as normal, Barret's Esophagus (BE) or dysplasia. The algorithm, using intensity features, GVD and scatterer size, combined with neural networks, resulted in 85% accuracy (67% sensitivity and 95% specificity) in discriminating normal vs. abnormal esophageal tissue and 89% accuracy (80% sensitivity and 91% specificity) in the classification of BE vs. Dysplasia. These results, although very preliminary, indicate that the proposed approach could assist medical diagnosis with improved accuracy.

Compared with other studies, the performance of the classification is equivalent (Table 9-1). Several studies have explored the use of OCT for the diagnosis of Barret's esophagus (BE), dysplasia and esophageal carcinomas. Various characteristics of BE, dysplasia and adenocarcinoma, were evaluated, with promising results. Nevertheless, discrimination of normal glands and BE and tumor glands was very challenging. Bouma et al., performed the first *in vivo* study with 32 patients, who underwent routine endoscopy, and exhibited some characteristics of BE [78]. OCT was also used for detection of BE before and after radiofrequency ablation therapy where OCT was found to distinguish normal glands from buried Barrett's glands only in a small percentage of the patients (7.7%) [53], [79]. Another study showed 81% sensitivity and 66% specificity in the detection of BE, indicating that OCT is presently not as accurate as histology [80]. OCT was further evaluated for the detection of esophageal dysplasia [81], [82]. Dysplasia was identified in OCT images based on reduced scattering and tissue structure changes, which are currently the only available criteria. Adenocarcinomas were also identified in OCT images with neoplastic epithelium containing large pockets of mucin surrounded by fibrotic and hypervascular tumor stroma. Occasionally, infiltration of heterogeneous structures into the muscular layers

was mentioned as a feature of tumor invasion. Asymmetrical shape and crowding of submucosal glands was also indicating of the presence of adenocarcinoma ([80], [83]. Identification of adenocarcinoma, in patients who underwent upper GI endoscopy, at a recognition rate of 95% also showed promise [84].

TABLE 9-1.COMPARISON OF OUR STUDY WITH PREVIOUS STATE-OF-THE-ART STUDIES

Study	Task	SEN[%]	SPE[%]	ACC[%]	AUC	Method	Comments
X.Qi et al., (2006)	Dysplasia in Barret's	82	74	83	-	PCA	106 OCT images from 13 BE patients
Diaz et al, (2015)	Dysplasia in Barret's	86	93	-	-	Naïve Bayes classifier	60 images from 38 patients
Ughi et al., (2016)	Dysplasia in Barret's	94%	93%	94	-	Proposed automated algorithm	4 patients, 50 images
Photiou et al., (2020)	Dysplasia in Barret's	80	91	89	0.85	ML classifiers comparison	Preliminary results with 10 patients
Swager et al., (2017)	Neoplasia in Barret's	90	93	-	0.91	ML classifiers comparison	29 endoscopic resections
Fonolla et al., (2019	Neoplasia in Barret's	95	85	88	0.95	Deep Learning	45 patients (VLE laser-marked ROIs)
Putten et al., (2020)	Neoplasia in Barret's	85	92	-	0.93	Deep Learning	23 patients **(**86 BE, 25 dysplasia regions**)**

In an effort to classify esophageal tissue, Qi et al., developed computer-aided diagnosis algorithms for the classification of dysplasia in Barret's esophagus using an endoscopic OCT system (EOCT). Using principal component analysis (PCA) and leave-one-out-cross validation, the results indicated that their CAD system has the potential to detect accurately the presence or absence of dysplasia for surveillance of Barrett's esophagus with an accuracy of 83%, sensitivity of 82% and specificity of 74%. In addition, Ughi et al. created a method for automated segmentation and characterization of the esophageal wall *in vivo*. Their procedure could effectively describe the diseased esophageal wall with an A-Scan line classification accuracy of 94% with a sensitivity and specificity of 94% and 93%, respectively [273]. Diaz et al. proposed a diagnostic computer algorithm to detect dysplasia in BE regions using discrete wavelet transform to analyze and characterize the local spatial distribution of gray levels in the images. Features extracted from the wavelet components that found to be statistically significant based on a 2- sample t-test were used as inputs to a

Naïve Bayes classifier. Leave-one-out cross-validation applied using an image volume of 60 images from 38 patients for BE vs. Dysplasia classification and resulted to 86% sensitivity and 93% specificity [309].

Swager et al. used 60 images (from 29 endoscopic resections) from BE patients to detect early neoplasia in BE comparing different ML classifiers and using leave-one-out cross-validation method. Three new features were proposed: layering and signal decay statistics, layering, and signal intensity distribution. The first exhibited the optimal performance compared to other features with an AUC, sensitivity and specificity of 91%, 90% and 93% respectively [310]. Furthermore, using Deep Learning approaches, Fonolla et al., trained an ensemble of deep convolutional neural networks to detect neoplasia in 45 BE patients. Their results showed 95% sensitivity, 85% specificity, accuracy of 88% and an AUC of 0.95 [311]. Van der Putten et al. proposed a fully automatic multi-step Computer-Aided Detection (CAD) algorithm that optimally leverages the effectiveness of deep learning strategies by encoding the principal dimension in esophageal data. They trained and tested their algorithm using data from 23 patients to detect neoplastic regions in BE. With the encoded principal dimension, they obtained an AUC of 0.93 with sensitivity and specificity of 85% and 92% respectively [312].

Unfortunately, the above studies have two very important limitations. First, they use leave-one-image-out cross validation method or A-Scan classification that severely biases the results. It is important to perform the classification with leave-one-patient-out cross validation to avoid severely biasing the algorithms when the classifiers are trained and tested with images from the same patient that can be very similar. Furthermore, no study performed Normal vs. Abnormal tissue classification, which is very important for screening procedures where image acquisition is performed without endoscopic guidance.

9.2 Future work

The results of this Thesis provide an initial demonstration of the potential of new features, combined with Machine Learning algorithms, to significantly enhance the diagnostic potential of OCT. However, these results are very preliminary and there is still much to be done to fully reveal and unequivocally prove their potential.

The algorithms proposed are A-Scan based, i.e. they analyze the data one line at a time. However, OCT images and volumes provide 2- and 3- dimensional data, which reflect the spatial variations of the tissue alterations caused by disease. This spatial information has not been considered in this Thesis and could prove very useful in improving the sensitivity and specificity of the diagnosis. Furthermore, several features that have been proposed in the literature have not been integrated in the Machine Learning process. These include fractal, texture and other information, which could improve the classification outcome. In addition, novel features could be extracted from the OCT images, including spectral and morphological characteristics. The latter, in particular, have not been explored in OCT despite the fact that they can reflect microstructural changes, which are the most robust criteria of visual OCT image inspection. As more data becomes available, the classification could be further improved by the introduction of deep learning methods to expand the current neural network approach.

In order for the diagnostic capability of the proposed techniques to be reliably validated, a larger number of patients is required. The larger amounts of data will be crucial in the refinement of the image processing and the classification algorithms. Of course, more patient images will introduce a new set of challenges. The management and standardization of these massive amounts of data is but one of the issues that will have to be resolved. Furthermore, if the data is collected by different operators or even different OCT machines, issues of comparability may appear. Perhaps one of the most taunting challenges will be to obtain accurate and reliable annotation of the data. Given the lack of agreed-upon OCT image criteria for diagnosis, it will be exceedingly hard to obtain annotations even from well trained radiologists. In addition, the annotations will have to repeated by more than one expert in order to reach consensus.

As with any new diagnostic approach, the clinical impact of the proposed methodology must be evaluated. In order for the suggested diagnostic tool to be clinically useful it must provide a significant improvement in the patient prognosis in an effective and efficient manner. These aspects can only be examined in clinical trials, which are much beyond the scope of this, or even the next, Thesis. However, these concerns should always be in the back of the investigators' minds in order to guide their research efforts to the right direction. Finally, it is always useful to consider other applications of the proposed techniques, both in the diagnosis of other diseases as well as in non-medical applications, such as non-destructive material testing.

References

[1] J. G. Fujimoto, C. Pitris, S. A. Boppart and M. E. Brezinski, "Optical coherence tomography: an emerging technology for biomedical imaging and optical biopsy," *Neoplasia (New York, NY),* vol. 2, p. 9, 2000.

[2] P. H. Tomlins and R. K. Wang, "Simultaneous analysis of refractive index and physical thickness by Fourier domain optical coherence tomography," *IEE Proceedings-Optoelectronics,* vol. 153, p. 222–228, 2006.

[3] S. Chang, Y. Cheng, K. V. Larin, Y. Mao, S. Sherif and C. Flueraru, "Optical coherence tomography used for security and fingerprint-sensing applications," *IET Image Processing,* vol. 2, p. 48–58, 2008.

[4] S. Chang, Y. Mao, G. Chang and C. Flueraru, "Jade detection and analysis based on optical coherence tomography images," *Optical Engineering,* vol. 49, p. 063602, 2010.

[5] S. Fuchs, A. Blinne, C. Rödel, U. Zastrau, V. Hilbert, M. Wünsche, J. Bierbach, E. Frumker, E. Förster and G. G. Paulus, "Optical coherence tomography using broad-bandwidth XUV and soft X-ray radiation," *Applied Physics B,* vol. 106, p. 789–795, 2012.

[6] U. Morgner, W. Drexler, F. X. Kärtner, X. D. Li, C. Pitris, E. P. Ippen and J. G. Fujimoto, "Spectroscopic optical coherence tomography," *Optics letters,* vol. 25, p. 111–113, 2000.

[7] J. Fujimoto and W. Drexler, "Introduction to optical coherence tomography," in *Optical coherence tomography,* Springer, 2008, p. 1–45.

[8] W. Drexler, U. Morgner, F. X. Kärtner, C. Pitris, S. A. Boppart, X. D. Li, E. P. Ippen and J. G. Fujimoto, "In vivo ultrahigh-resolution optical coherence tomography," *Optics letters,* vol. 24, p. 1221–1223, 1999.

[9] D. A. Boas, C. Pitris and N. Ramanujam, Handbook of biomedical optics, CRC press, 2016.

[10] E. A. Swanson, J. A. Izatt, M. R. Hee, D. Huang, C. P. Lin, J. S. Schuman, C. A. Puliafito and J. G. Fujimoto, "In vivo retinal imaging by optical coherence tomography," *Optics letters,* vol. 18, p. 1864–1866, 1993.

[11] J. M. Schmitt, "Optical coherence tomography (OCT): a review," *IEEE Journal of selected topics in quantum electronics,* vol. 5, p. 1205–1215, 1999.

[12] Y. Pan, R. Birngruber, J. Rosperich and R. Engelhardt, "Low-coherence optical tomography in turbid tissue: theoretical analysis," *Applied optics,* vol. 34, p. 6564–6574, 1995.

[13] A. F. Fercher, C. K. Hitzenberger, G. Kamp and S. Y. El-Zaiat, "Measurement of intraocular distances by backscattering spectral interferometry," *Optics communications,* vol. 117, p. 43–48, 1995.

[14] J. Schwider and L. Zhou, "Dispersive interferometric profilometer," *Optics letters,* vol. 19, p. 995–997, 1994.

[15] C. S. Seelamantula, M. L. Villiger, R. A. Leitgeb and M. Unser, "Exact and efficient signal reconstruction in frequency-domain optical-coherence tomography," *JOSA A,* vol. 25, p. 1762–1771, 2008.

[16] M. Wojtkowski, A. Kowalczyk, R. Leitgeb and A. F. Fercher, "Full range complex spectral optical coherence tomography technique in eye imaging," *Optics letters,* vol. 27, p. 1415–1417, 2002.

[17] S. Chang, Y. Mao, C. Flueraru and S. Sherif, "Optical coherence tomography: technology and applications," in *2008 International Conference on Optical Instruments and Technology: Optical Systems and Optoelectronic Instruments*, 2009.

[18] R. A. Leitgeb, C. K. Hitzenberger, A. F. Fercher and T. Bajraszewski, "Phase-shifting algorithm to achieve high-speed long-depth-range probing by frequency-domain optical coherence tomography," *Optics letters,* vol. 28, p. 2201–2203, 2003.

[19] A. F. Fercher, W. Drexler, C. K. Hitzenberger and T. Lasser, "Optical coherence tomography-principles and applications," *Reports on progress in physics,* vol. 66, p. 239, 2003.

[20] N. Eladawi, M. M. Elmogy, M. Ghazal, O. Helmy, A. Aboelfetouh, A. Riad, S. Schaal and A. El-Baz, "Classification of retinal diseases based on OCT images," *Front Biosci,* vol. 23, p. 247–64, 2018.

[21] S. G. Karst, M. Salas, J. Hafner, C. Scholda, W.-D. Vogl, W. Drexler, M. Pircher and U. Schmidt-Erfurth, "Three-dimensional analysis of retinal microaneurysms with adaptive optics optical coherence tomography," *Retina,* vol. 39, p. 465–472, 2019.

[22] M. Joner, T. Koppara, R. A. Byrne, M. I. Castellanos, J. Lewerich, J. Novotny, G. Guagliumi, E. Xhepa, T. Adriaenssens, T. C. Godschalk and others,

"Neoatherosclerosis in patients with coronary stent thrombosis: findings from optical coherence tomography imaging (a report of the PRESTIGE consortium)," *JACC: Cardiovascular Interventions,* vol. 11, p. 1340–1350, 2018.

[23] A. Samir and A. ElGuindy, "The role of intracoronary imaging in acute coronary syndromes: OCT in focus," *Global cardiology science & practice,* vol. 2016, 2016.

[24] A. G. Podoleanu, J. A. Rogers, D. A. Jackson and S. Dunne, "Three dimensional OCT images from retina and skin," *Optics Express,* vol. 7, p. 292–298, 2000.

[25] N. V. Iftimia, G. N. Maguluri, J. Park, W. J. Fox and M. Rajadhyaksha, "New advances in RCM-OCT imaging for non-melanoma skin cancer detection and therapy guidance (Conference Presentation)," in *Optical Biopsy XVI: Toward Real-Time Spectroscopic Imaging and Diagnosis*, 2018.

[26] A. Rajabi-Estarabadi, J. M. Bittar, C. Zheng, V. Nascimento, I. Camacho, L. G. Feun, M. Nasiriavanaki, M. Kunz and K. Nouri, "Optical coherence tomography imaging of melanoma skin cancer," *Lasers in medical science,* vol. 34, p. 411–420, 2019.

[27] L. P. Rangaraju, G. Kunapuli, D. Every, O. D. Ayala, P. Ganapathy and A. Mahadevan-Jansen, "Classification of burn injury using Raman spectroscopy and optical coherence tomography: An ex-vivo study on porcine skin," *Burns,* vol. 45, p. 659–670, 2019.

[28] Y. Li, H. Liu, H. Huang, Y. Zhu, H. Deng, J. Yu, S. Luo, L. Huo, L. Lin, H. Xie and others, "Progress of the application of optical coherence tomography in gastrointestinal tumor surgery," *Zhonghua wei chang wai ke za zhi= Chinese journal of gastrointestinal surgery,* vol. 20, p. 716–720, 2017.

[29] H.-C. Lee, O. O. Ahsen, J. J. Liu, T.-H. Tsai, Q. Huang, H. Mashimo and J. G. Fujimoto, "Assessment of the radiofrequency ablation dynamics of esophageal tissue with optical coherence tomography," *Journal of biomedical optics,* vol. 22, p. 076001, 2017.

[30] S. Luo, H. Liu, H. Zhao, X. An, H. Xie and L. Huo, "Gastric and colon cancer imaging with swept source optical coherence tomography," in *2017 Conference on Lasers and Electro-Optics Pacific Rim (CLEO-PR)*, 2017.

[31] P. Struk, S. Bargiel, Q. A. A. Tanguy, C. Gorecki, H. Xie, R. Chutani, N. Passilly and A. Billard, "The SS-OCT endomicroscopy probe based on MOEMS Mirau micro-interferometer for early stomach cancer detection," in *Optical Micro-and Nanometrology VII*, 2018.

[32] S. A. Boppart, W. Luo, D. L. Marks and K. W. Singletary, "Optical coherence tomography: feasibility for basic research and image-guided surgery of breast cancer," *Breast cancer research and treatment,* vol. 84, p. 85–97, 2004.

[33] T. Milner, A. Estrada, A. B. McElroy and N. Katta, "OCT for image-guided therapy and surgery," 2019.

[34] S. J. Erickson-Bhatt, K. J. Mesa, M. Marjanovic, E. J. Chaney, A. Ahmad, P.-C. Huang, Z. G. Liu, K. Cunningham and S. A. Boppart, "Intraoperative optical coherence tomography of the human thyroid: Feasibility for surgical assessment," *Translational Research,* vol. 195, p. 13–24, 2018.

[35] S. Sommerey, N. Al Arabi, R. Ladurner, C. Chiapponi, H. Stepp, K. K. J. Hallfeldt and J. K. S. Gallwas, "Intraoperative optical coherence tomography imaging to identify parathyroid glands," *Surgical endoscopy,* vol. 29, p. 2698–2704, 2015.

[36] H.-C. Lee, C. Zhou, D. W. Cohen, A. E. Mondelblatt, Y. Wang, A. D. Aguirre, D. Shen, Y. Sheikine, J. G. Fujimoto and J. L. Connolly, "Integrated optical coherence tomography and optical coherence microscopy imaging of ex vivo human renal tissues," *The Journal of urology,* vol. 187, p. 691–699, 2012.

[37] M. L. Onozato, P. M. Andrews, Q. Li, J. Jiang, A. Cable and Y. Chen, "Optical coherence tomography of human kidney," *The Journal of urology,* vol. 183, p. 2090–2094, 2010.

[38] Y.-Q. Xiong, J. Tan, Y.-M. Liu, Y.-Z. Li, F.-F. You, M.-Y. Zhang, Q. Chen, K. Zou and X. Sun, "Diagnostic accuracy of optical coherence tomography for bladder cancer: A systematic review and meta-analysis," *Photodiagnosis and photodynamic therapy,* vol. 27, p. 298–304, 2019.

[39] K. Singh, C. L. Wu, G. J. Tearney and others, "Imaging the human prostate gland using 1-lm-resolution optical coherence tomography," 2019.

[40] L. Scolaro, R. A. McLaughlin, B. F. Kennedy, C. M. Saunders and D. D. Sampson, "A review of optical coherence tomography in breast cancer," *Photonics & Lasers in Medicine,* vol. 3, p. 225–240, 2014.

[41] R. Ha, L. C. Friedlander, H. Hibshoosh, C. Hendon, S. Feldman, S. Ahn, H. Schmidt, M. K. Akens, M. Fitzmaurice, B. C. Wilson and others, "Optical coherence tomography: A novel imaging method for post-lumpectomy breast margin assessment—A multi-reader study," *Academic radiology,* vol. 25, p. 279–287, 2018.

[42] A. Butola, A. Ahmad, V. Dubey, V. Srivastava, D. Qaiser, A. Srivastava, P. Senthilkumaran and D. S. Mehta, "Volumetric analysis of breast cancer tissues using machine learning and swept-source optical coherence tomography," *Applied optics,* vol. 58, p. A135–A141, 2019.

[43] B. Baumann, "Optical Coherence Tomography for Brain Imaging," in *Advanced Optical Methods for Brain Imaging*, Springer, 2019, p. 49–68.

[44] J. Malone, G. Hohert, L. Hoang, D. M. Miller, J. McAlpine, C. MacAulay and P. Lane, "Endoscopic optical coherence tomography (OCT) and autofluorescence imaging (AFI) of ex vivo fallopian tubes," in *Multimodal Biomedical Imaging XV*, 2020.

[45] T. Wang, M. Brewer and Q. Zhu, "An overview of optical coherence tomography for ovarian tissue imaging and characterization," *Wiley Interdisciplinary Reviews: Nanomedicine and Nanobiotechnology,* vol. 7, p. 1–16, 2015.

[46] Peters et al., ""Noninvasive detection of metastases and follicle density in ovarian tissue using full-field optical coherence tomography."," *Clinical Cancer Research 22.22 (2016): 5506-5513.*, 2016.

[47] R. Ladurner, K. K. J. Hallfeldt, N. Al Arabi, H. Stepp, S. Mueller and J. K. S. Gallwas, "Optical coherence tomography as a method to identify parathyroid glands," *Lasers in surgery and medicine,* vol. 45, p. 654–659, 2013.

[48] C. Zhou, Y. Wang, A. D. Aguirre, T.-H. Tsai, D. W. Cohen, J. L. Connolly and J. G. Fujimoto, "Ex vivo imaging of human thyroid pathology using integrated optical coherence tomography and optical coherence microscopy," *Journal of biomedical optics,* vol. 15, p. 016001, 2010.

[49] G. Capocasale, M. Mignogna, D. A. Santarelli and G. Campisi, "Validation of Optical Coherence Tomography in the assessment of Oral Potentially Malignant Disorders and Oral Cancer," 2018.

[50] G. J. Tearney, B. E. Bouma and J. G. Fujimoto, "High-speed phase-and group-delay scanning with a grating-based phase control delay line," *Optics letters,* vol. 22, p. 1811–1813, 1997.

[51] S. Luo, Y. Fan, W. Chang, H. Liao, H. Kang and L. Huo, "Classification of human stomach cancer using morphological feature analysis from optical coherence tomography images," *Laser Physics Letters,* vol. 16, p. 095602, 2019.

[52] Y. Zhu, W. Gao, Y. Zhou, Y. Guo, F. Guo and Y. He, "Rapid and high-resolution imaging of human liver specimens by full-field optical coherence tomography," *Journal of biomedical optics*, vol. 20, p. 116010, 2015.

[53] K. Liang, O. O. Ahsen, H.-C. Lee, Z. Wang, B. M. Potsaid, M. Figueiredo, V. Jayaraman, A. E. Cable, Q. Huang, H. Mashimo and others, "Volumetric mapping of Barrett's esophagus and dysplasia with en face optical coherence tomography tethered capsule," *The American journal of gastroenterology*, vol. 111, p. 1664, 2016.

[54] M. T. El-Haddad and Y. K. Tao, "Advances in intraoperative optical coherence tomography for surgical guidance," *Current Opinion in Biomedical Engineering*, vol. 3, p. 37–48, 2017.

[55] L. P. Hariri, M. Mino-Kenudson, M. Lanuti, A. J. Miller, E. J. Mark and M. J. Suter, "Diagnosing lung carcinomas with optical coherence tomography," *Annals of the American Thoracic Society*, vol. 12, p. 193–201, 2015.

[56] L. P. Hariri, D. C. Adams, M. Lanuti, J. C. Wain, A. M. Tager and M. J. Suter, "Bronchoscopic optical coherence tomography as a low risk method for microscopic diagnosis of idiopathic pulmonary fibrosis," in *A94. new insights in ipf*, American Thoracic Society, 2016, p. A2608–A2608.

[57] T. M. Jørgensen, A. Tycho, M. Mogensen, P. Bjerring and G. B. E. Jemec, "Machine-learning classification of non-melanoma skin cancers from image features obtained by optical coherence tomography," *Skin Research and Technology*, vol. 14, p. 364–369, 2008.

[58] M. Mogensen, T. M. Jørgensen, B. M. Nürnberg, H. A. Morsy, J. B. THOMSEN, L. Thrane and G. B. E. Jemec, "Assessment of optical coherence tomography imaging in the diagnosis of non-melanoma skin cancer and benign lesions versus normal skin: observer-blinded evaluation by dermatologists and pathologists," *Dermatologic Surgery*, vol. 35, p. 965–972, 2009.

[59] M. Ulrich, T. Von Braunmuehl, H. Kurzen, T. Dirschka, C. Kellner, E. Sattler, C. Berking, J. Welzel and U. Reinhold, "The sensitivity and specificity of optical coherence tomography for the assisted diagnosis of nonpigmented basal cell carcinoma: an observational study," *British Journal of Dermatology*, vol. 173, p. 428–435, 2015.

[60] Z. Hamdoon, W. Jerjes, G. McKenzie, A. Jay and C. Hopper, "Optical coherence tomography in the assessment of oral squamous cell carcinoma resection margins," *Photodiagnosis and photodynamic therapy,* vol. 13, p. 211–217, 2016.

[61] F. De Leeuw, O. Casiraghi, A. B. Lakhdar, M. Abbaci and C. Laplace-Builhé, "Full-field OCT for fast diagnostic of head and neck cancer," in *Photonic Therapeutics and Diagnostics XI*, 2015.

[62] S. Lam, B. Standish, C. Baldwin, A. McWilliams, A. Gazdar, A. I. Vitkin, V. Yang, N. Ikeda, C. MacAulay and others, "In vivo optical coherence tomography imaging of preinvasive bronchial lesions," *Clinical cancer research,* vol. 14, p. 2006–2011, 2008.

[63] R. G. Michel, G. T. Kinasewitz, K.-M. Fung and J. I. Keddissi, "Optical coherence tomography as an adjunct to flexible bronchoscopy in the diagnosis of lung cancer: a pilot study," *Chest,* vol. 138, p. 984–988, 2010.

[64] S. C. Whiteman, Y. Yang, D. G. van Pittius, M. Stephens, J. Parmer and M. A. Spiteri, "Optical coherence tomography: real-time imaging of bronchial airways microstructure and detection of inflammatory/neoplastic morphologic changes," *Clinical Cancer Research,* vol. 12, p. 813–818, 2006.

[65] O. Assayag, M. Antoine, B. Sigal-Zafrani, M. Riben, F. Harms, A. Burcheri, K. Grieve, E. Dalimier, B. Le Conte de Poly and C. Boccara, "Large field, high resolution full-field optical coherence tomography: a pre-clinical study of human breast tissue and cancer assessment," *Technology in cancer research & treatment,* vol. 13, p. 455–468, 2014.

[66] R. M. Nolan, S. G. Adie, M. Marjanovic, E. J. Chaney, F. A. South, G. L. Monroy, N. D. Shemonski, S. J. Erickson-Bhatt, R. L. Shelton, A. J. Bower and others, "Intraoperative optical coherence tomography for assessing human lymph nodes for metastatic cancer," *BMC cancer,* vol. 16, p. 144, 2016.

[67] K. Grieve, K. Mouslim, O. Assayag, E. Dalimier, F. Harms, A. Bruhat, C. Boccara and M. Antoine, "Assessment of sentinel node biopsies with full-field optical coherence tomography," *Technology in cancer research & treatment,* vol. 15, p. 266–274, 2016.

[68] X. Yao, Y. Gan, E. Chang, H. Hibshoosh, S. Feldman and C. Hendon, "Visualization and tissue classification of human breast cancer images using ultrahigh-resolution OCT," *Lasers in surgery and medicine,* vol. 49, p. 258–269, 2017.

[69] C. Zhou, D. W. Cohen, Y. Wang, H.-C. Lee, A. E. Mondelblatt, T.-H. Tsai, A. D. Aguirre, J. G. Fujimoto and J. L. Connolly, "Integrated optical coherence tomography and microscopy for ex vivo multiscale evaluation of human breast tissues," *Cancer research,* vol. 70, p. 10071–10079, 2010.

[70] K. M. RL Siegel, ""Cancer statistics"," *Ca Cancer J Clin,* 2018.

[71] Yang et al., ""Potential role of a hybrid intraoperative probe based on OCT and positron detection for ovarian cancer detection and characterization."," *Biomedical optics express 2.7 (2011): 1918-1930.,* 2011.

[72] M. S. Nandy and Q. Zhu., ""Classification and analysis of human ovarian tissue using full field optical coherence tomography."," *Biomedical optics express 7.12 (2016): 5182-5187.,* 2016.

[73] Pierre et al., ""Dimension reduction technique using a multilayered descriptor for high-precision classification of ovarian cancer tissue using optical coherence tomography: a feasibility study."," *Journal of Medical Imaging 4.4 (2017): 041306.,* 2017.

[74] P. A. Testoni, A. Mariani, B. Mangiavillano, L. Albarello, P. G. Arcidiacono, E. Masci and C. Doglioni, "Main pancreatic duct, common bile duct and sphincter of Oddi structure visualized by optical coherence tomography: An ex vivo study compared with histology," *Digestive and liver disease,* vol. 38, p. 409–414, 2006.

[75] P. A. Testoni, A. Mariani, B. Mangiavillano, P. G. Arcidiacono, S. Di Pietro and E. Masci, "Intraductal optical coherence tomography for investigating main pancreatic duct strictures," *American Journal of Gastroenterology,* vol. 102, p. 269–274, 2007.

[76] M. Arvanitakis, L. Hookey, G. Tessier, P. Demetter, N. Nagy, A. Stellke, V. De Maertelaer, J. Devière and O. Le Moine, "Intraductal optical coherence tomography during endoscopic retrograde cholangiopancreatography for investigation of biliary strictures," *Endoscopy,* vol. 41, p. 696–701, 2009.

[77] L. van Manen, P. L. Stegehuis, A. Farina-Sarasqueta, L. M. de Haan, J. Eggermont, B. A. Bonsing, H. Morreau, B. P. F. Lelieveldt, C. J. H. van de Velde, A. L. Vahrmeijer and others, "Validation of full-field optical coherence tomography in distinguishing malignant and benign tissue in resected pancreatic cancer specimens," *PloS one,* vol. 12, 2017.

[78] B. E. Bouma, G. J. Tearney, C. C. Compton and N. S. Nishioka, "High-resolution imaging of the human esophagus and stomach in vivo using optical coherence tomography," *Gastrointestinal endoscopy,* vol. 51, p. 467–474, 2000.

[79] A.-F. Swager, D. F. Boerwinkel, D. M. de Bruin, D. J. Faber, T. G. van Leeuwen, B. L. Weusten, S. L. Meijer, J. J. Bergman and W. L. Curvers, "Detection of buried Barrett's glands after radiofrequency ablation with volumetric laser endomicroscopy," *Gastrointestinal endoscopy,* vol. 83, p. 80–88, 2016.

[80] J. A. Evans, J. M. Poneros, B. E. Bouma, J. Bressner, E. F. Halpern, M. Shishkov, G. Y. Lauwers, M. Mino–Kenudson, N. S. Nishioka and G. J. Tearney, "Optical coherence tomography to identify intramucosal carcinoma and high-grade dysplasia in Barrett's esophagus," *Clinical Gastroenterology and Hepatology,* vol. 4, p. 38–43, 2006.

[81] X. Qi, M. V. Sivak, G. Isenberg, J. Willis and A. M. Rollins, "Computer-aided diagnosis of dysplasia in Barrett's esophagus using endoscopic optical coherence tomography," *Journal of biomedical optics,* vol. 11, p. 044010, 2006.

[82] G. Isenberg, M. V. Sivak Jr, A. Chak, R. C. K. Wong, J. E. Willis, B. Wolf, D. Y. Rowland, A. Das and A. Rollins, "Accuracy of endoscopic optical coherence tomography in the detection of dysplasia in Barrett's esophagus: a prospective, double-blinded study," *Gastrointestinal endoscopy,* vol. 62, p. 825–831, 2005.

[83] Y. Chen, A. D. Aguirre, P.-L. Hsiung, S. Desai, P. R. Herz, M. Pedrosa, Q. Huang, M. Figueiredo, S.-W. Huang, A. Koski and others, "Ultrahigh resolution optical coherence tomography of Barrett's esophagus: preliminary descriptive clinical study correlating images with histology," *Endoscopy,* vol. 39, p. 599–605, 2007.

[84] G. Zuccaro, N. Gladkova, J. Vargo, F. Feldchtein, E. Zagaynova, D. Conwell, G. Falk, J. Goldblum, J. Dumot, J. Ponsky and others, "Optical coherence tomography of the esophagus and proximal stomach in health and disease," *The American journal of gastroenterology,* vol. 96, p. 2633–2639, 2001.

[85] W. Hatta, K. Uno, T. Koike, S. Yokosawa, K. Iijima, A. Imatani and T. Shimosegawa, "Optical coherence tomography for the staging of tumor infiltration in superficial esophageal squamous cell carcinoma," *Gastrointestinal endoscopy,* vol. 71, p. 899–906, 2010.

[86] G. J. Tearney, M. E. Brezinski, J. F. Southern, B. E. Bouma, S. A. Boppart and J. G. Fujimoto, "Optical biopsy in human gastrointestinal tissue using optical coherence tomography.," *American Journal of Gastroenterology,* vol. 92, 1997.

[87] V. Westphal, A. M. Rollins, J. Willis, M. V. Sivak Jr and J. A. Izatt, "Correlation of endoscopic optical coherence tomography with histology in the lower-GI tract," *Gastrointestinal endoscopy,* vol. 61, p. 537–546, 2005.

[88] P. C. Ashok, B. B. Praveen, N. Bellini, A. Riches, K. Dholakia and C. S. Herrington, "Multi-modal approach using Raman spectroscopy and optical coherence tomography for the discrimination of colonic adenocarcinoma from normal colon," *Biomedical optics express,* vol. 4, p. 2179–2186, 2013.

[89] Q. Q. Zhang, X. J. Wu, T. Tang, S. W. Zhu, Q. Yao, B. Z. Gao and X. C. Yuan, "Quantitative analysis of rectal cancer by spectral domain optical coherence tomography," *Physics in Medicine & Biology,* vol. 57, p. 5235, 2012.

[90] N. Gladkova, O. Streltsova, E. Zagaynova, E. Kiseleva, V. Gelikonov, G. Gelikonov, M. Karabut, K. Yunusova and O. Evdokimova, "Cross-polarization optical coherence tomography for early bladder-cancer detection: statistical study," *Journal of biophotonics,* vol. 4, p. 519–532, 2011.

[91] A. C. Goh and S. P. Lerner, "Application of new technology in bladder cancer diagnosis and treatment," *World journal of urology,* vol. 27, p. 301–307, 2009.

[92] M. J. Manyak, N. D. Gladkova, J. H. Makari, A. M. Schwartz, E. V. Zagaynova, L. Zolfaghari, J. M. Zara, R. Iksanov and F. I. Feldchtein, "Evaluation of superficial bladder transitional-cell carcinoma by optical coherence tomography," *Journal of endourology,* vol. 19, p. 570–574, 2005.

[93] Montagne et al., ""Quality control and primo-diagnosis of transurethral bladder resections with full-field OCT."," *Therapeutics and Diagnostics in Urology: Lasers, Robotics, Minimally Invasive, and Advanced Biomedical Devices. Vol. 10038.*, 2017.

[94] G. P. Agrawal, Fiber-optic communication systems, vol. 222, John Wiley & Sons, 2012.

[95] B. Bouma, G. J. Tearney, S. A. Boppart, M. R. Hee, M. E. Brezinski and J. G. Fujimoto, "High-resolution optical coherence tomographic imaging using a mode-locked Ti: Al 2 O 3 laser source," *Optics letters,* vol. 20, p. 1486–1488, 1995.

[96] S. Iyer, S. Coen and F. Vanholsbeeck, "Dual-fiber stretcher as a tunable dispersion compensator for an all-fiber optical coherence tomography system," *Optics letters,* vol. 34, p. 2903–2905, 2009.

[97] L. Froehly, S. Iyer and F. Vanholsbeeck, "Dual-fibre stretcher and coma as tools for independent 2nd and 3rd order tunable dispersion compensation in a fibre-based 'scan-free'time domain optical coherence tomography system," *Optics Communications,* vol. 284, p. 4099–4106, 2011.

[98] N. Lippok, S. Coen, P. Nielsen and F. Vanholsbeeck, "Dispersion compensation in Fourier domain optical coherence tomography using the fractional Fourier transform," *Optics express,* vol. 20, p. 23398–23413, 2012.

[99] Y. Park, T. Yamauchi, W. Choi, R. Dasari and M. S. Feld, "Spectroscopic phase microscopy for quantifying hemoglobin concentrations in intact red blood cells," *Optics letters,* vol. 34, p. 3668–3670, 2009.

[100] D. Fu, W. Choi, Y. Sung, Z. Yaqoob, R. R. Dasari and M. Feld, "Quantitative dispersion microscopy," *Biomedical optics express,* vol. 1, p. 347–353, 2010.

[101] H. Ding, J. Q. Lu, W. A. Wooden, P. J. Kragel and X.-H. Hu, "Refractive indices of human skin tissues at eight wavelengths and estimated dispersion relations between 300 and 1600 nm," *Physics in Medicine & Biology,* vol. 51, p. 1479, 2006.

[102] A. J. Levine, G. V. Woude, W. C. Topp and J. D. Watson, *Cancer Cells, The Transformed Phenotype, vol. 1,* Cold Spring Harbor Laboratory Press, Cold Spring Harbor, NY, 1984.

[103] G. Shetty, C. Kendall, N. Shepherd, N. Stone and H. Barr, "Raman spectroscopy: elucidation of biochemical changes in carcinogenesis of oesophagus," *British journal of cancer,* vol. 94, p. 1460–1464, 2006.

[104] G. P. Agrawal, "Applications of Nonlinear Fiber Optics Academic," *San Diego,* 2001.

[105] M. R. Hee, "Optical coherence tomography of the eye," 1997.

[106] N. Lippok, S. G. Murdoch, K.-L. Wu and F. Vanholsbeeck, "Dispersion mapping at the micrometer scale using tri-band optical frequency domain imaging," *Optics letters,* vol. 38, p. 3028–3031, 2013.

[107] S. M. Kolenderska, B. Bräuer and F. Vanholsbeeck, "Dispersion mapping as a simple postprocessing step for Fourier domain Optical Coherence Tomography data," *Scientific reports,* vol. 8, p. 1–7, 2018.

[108] S. Schlichting, T. Willemsen, H. Ehlers, U. Morgner and D. Ristau, "Direct in situ GDD measurement in optical coating process," in *Optical Systems Design 2015: Advances in Optical Thin Films V*, 2015.

[109] C. Dorrer, N. Belabas, J.-P. Likforman and M. Joffre, "Spectral resolution and sampling issues in Fourier-transform spectral interferometry," *JOSA B*, vol. 17, p. 1795–1802, 2000.

[110] G. J. Tearney, M. E. Brezinski, J. F. Southern, B. E. Bouma, M. R. Hee and J. G. Fujimoto, "Determination of the refractive index of highly scattering human tissue by optical coherence tomography," *Optics letters*, vol. 20, p. 2258–2260, 1995.

[111] Y. Cotte, F. Toy, P. Jourdain, N. Pavillon, D. Boss, P. Magistretti, P. Marquet and C. Depeursinge, "Marker-free phase nanoscopy," *Nature Photonics*, vol. 7, p. 113, 2013.

[112] T. Kim, R. Zhou, M. Mir, S. D. Babacan, P. S. Carney, L. L. Goddard and G. Popescu, "White-light diffraction tomography of unlabelled live cells," *Nature Photonics*, vol. 8, p. 256, 2014.

[113] M. Bennet, D. Gur, J. Yoon, Y. Park and D. Faivre, "A bacteria-based remotely tunable photonic device," *Advanced Optical Materials*, vol. 5, p. 1600617, 2017.

[114] K. Lee, K. Kim, J. Jung, J. Heo, S. Cho, S. Lee, G. Chang, Y. Jo, H. Park and Y. Park, "Quantitative phase imaging techniques for the study of cell pathophysiology: from principles to applications," *Sensors*, vol. 13, p. 4170–4191, 2013.

[115] K. Kim, H. Yoon, M. Diez-Silva, M. Dao, R. R. Dasari and Y. Park, "High-resolution three-dimensional imaging of red blood cells parasitized by Plasmodium falciparum and in situ hemozoin crystals using optical diffraction tomography," *Journal of biomedical optics*, vol. 19, p. 011005, 2013.

[116] D. J. Weatherall, "Systems biology and red cells," *N. Engl. J. Med*, vol. 364, p. 376–377, 2011.

[117] J. Jung, L. E. Matemba, K. Lee, P. E. Kazyoba, J. Yoon, J. J. Massaga, K. Kim, D.-J. Kim and Y. Park, "Optical characterization of red blood cells from individuals with sickle cell trait and disease in Tanzania using quantitative phase imaging," *Scientific reports*, vol. 6, p. 31698, 2016.

[118] S. Martin and R. G. Parton, "Lipid droplets: a unified view of a dynamic organelle," *Nature reviews Molecular cell biology*, vol. 7, p. 373–378, 2006.

[119] M. A. Welte, *Fat on the move: intracellular motion of lipid droplets*, Portland Press Ltd., 2009.

[120] J. Beuthan, O. Minet, J. Helfmann, M. Herrig and G. Müller, "The spatial variation of the refractive index in biological cells," *Physics in Medicine & Biology,* vol. 41, p. 369, 1996.

[121] F. Wilfling, J. T. Haas, T. C. Walther and R. V. Farese Jr, "Lipid droplet biogenesis," *Current opinion in cell biology,* vol. 29, p. 39–45, 2014.

[122] S. Sridharan, V. Macias, K. Tangella, A. Kajdacsy-Balla and G. Popescu, "Prediction of prostate cancer recurrence using quantitative phase imaging," *Scientific reports,* vol. 5, p. 1–10, 2015.

[123] H. Majeed, M. E. Kandel, K. Han, Z. Luo, V. Macias, K. V. Tangella, A. Balla and G. Popescu, "Breast cancer diagnosis using spatial light interference microscopy," *Journal of biomedical optics,* vol. 20, p. 111210, 2015.

[124] J.-W. Su, Y.-H. Lin, C.-P. Chiang, J.-M. Lee, C.-M. Hsieh, M.-S. Hsieh, P.-W. Yang, C.-P. Wang, P.-H. Tseng, Y.-C. Lee and others, "Precancerous esophageal epithelia are associated with significantly increased scattering coefficients," *Biomedical optics express,* vol. 6, p. 3795–3805, 2015.

[125] M. Lee, E. Lee, J. Jung, H. Yu, K. Kim, J. Yoon, S. Lee, Y. Jeong and Y. Park, "Label-free optical quantification of structural alterations in Alzheimer's disease," *Scientific reports,* vol. 6, p. 31034, 2016.

[126] S.-A. Yang, J. Yoon, K. Kim and Y. Park, "Measurements of morphological and biophysical alterations in individual neuron cells associated with early neurotoxic effects in Parkinson's disease," *Cytometry part A,* vol. 91, p. 510–518, 2017.

[127] S. S. Batsanov, E. D. Ruchkin and I. A. Poroshina, Refractive Indices of Solids, Springer, 2016.

[128] H. Onodera, I. Awai and J.-i. Ikenoue, "Refractive-index measurement of bulk materials: prism coupling method," *Applied optics,* vol. 22, p. 1194–1197, 1983.

[129] A. J. Werner, "Methods in high precision refractometry of optical glasses," *Applied optics,* vol. 7, p. 837–843, 1968.

[130] H. J. Choi, H. H. Lim, H. S. Moon, T. B. Eom, J. J. Ju and M. Cha, "Measurement of refractive index and thickness of transparent plate by dual-wavelength interference," *Optics Express,* vol. 18, p. 9429–9434, 2010.

[131] G. D. Gillen and S. Guha, "Use of Michelson and Fabry–Perot interferometry for independent determination of the refractive index and physical thickness of wafers," *Applied optics,* vol. 44, p. 344–347, 2005.

[132] I. Ohlídal, "Immersion spectroscopic reflectometry of multilayer systems. I. Theory," *JOSA A,* vol. 5, p. 459–464, 1988.

[133] W. P. Ellis, "Immersion Spectrophotometry of Interference Films: Refractive Indices of Fluoride Films on Uranium Dioxide and Anodic Oxide Films on Uranium Metal," *JOSA,* vol. 53, p. 613–619, 1963.

[134] I. Ohlídal and K. Navrátil, "Optical analysis of non-absorbing double layers by means of immersion reflectometry II: Solid state immersion method," *Thin Solid Films,* vol. 71, p. 91–102, 1980.

[135] W.-C. Kuo, Y.-K. Bou and C.-M. Lai, "Simultaneous measurement of refractive index and thickness of transparent material by dual-beam confocal microscopy," *Measurement Science and Technology,* vol. 24, p. 075003, 2013.

[136] U. Schnell, E. Zimmermann and R. Dandliker, "Absolute distance measurement with synchronously sampled white-light channelled spectrum interferometry," *Pure and Applied Optics: Journal of the European Optical Society Part A,* vol. 4, p. 643, 1995.

[137] M. Ohmi, T. Shiraishi, H. Tajiri and M. Haruna, "Simultaneous measurement of refractive index and thickness of transparent plates by low coherence interferometry," *Optical review,* vol. 4, p. 507–515, 1997.

[138] M. Ohmi, Y. Ohnishi, K. Yoden and M. Haruna, "In vitro simultaneous measurement of refractive index and thickness of biological tissue by the low coherence interferometry," *IEEE Transactions on Biomedical Engineering,* vol. 47, p. 1266–1270, 2000.

[139] Y. Zhou, K. K. H. Chan, T. Lai and S. Tang, "Characterizing refractive index and thickness of biological tissues using combined multiphoton microscopy and optical coherence tomography," *Biomedical optics express,* vol. 4, p. 38–50, 2013.

[140] M. Haruna, M. Ohmi, T. Mitsuyama, H. Tajiri, H. Maruyama and M. Hashimoto, "Simultaneous measurement of the phase and group indices and the thickness of transparent plates by low-coherence interferometry," *Optics letters,* vol. 23, p. 966–968, 1998.

[141] K. Zhang, L. Tao, W. Cheng, J. Liu and Z. Chen, "Air etalon facilitated simultaneous measurement of group refractive index and thickness using spectral interferometry," *Applied optics,* vol. 53, p. 7483–7486, 2014.

[142] S. Kim, J. Na, M. J. Kim and B. H. Lee, "Simultaneous measurement of refractive index and thickness by combining low-coherence interferometry and confocal optics," *Optics express,* vol. 16, p. 5516–5526, 2008.

[143] H. Maruyama, T. Mitsuyama, M. Ohmi and M. Haruna, "Simultaneous measurement of refractive index and thickness by low coherence interferometry considering chromatic dispersion of index," *Optical Review,* vol. 7, p. 468–472, 2000.

[144] M. Ohmi, H. Nishi, Y. Konishi, Y. Yamada and M. Haruna, "High-speed simultaneous measurement of refractive index and thickness of transparent plates by low-coherence interferometry and confocal optics," *Measurement Science and Technology,* vol. 15, p. 1531, 2004.

[145] T. Fukano and I. Yamaguchi, "Simultaneous measurement of thicknesses and refractive indices of multiple layers by a low-coherence confocal interference microscope," *Optics letters,* vol. 21, p. 1942–1944, 1996.

[146] S. A. Alexandrov, A. V. Zvyagin, K. D. Silva and D. D. Sampson, "Bifocal optical coherenc refractometry of turbid media," *Optics letters,* vol. 28, p. 117–119, 2003.

[147] A. V. Zvyagin, K. D. Silva, S. A. Alexandrov, T. R. Hillman, J. J. Armstrong, T. Tsuzuki and D. D. Sampson, "Refractive index tomography of turbid media by bifocal optical coherence refractometry," *Optics Express,* vol. 11, p. 3503–3517, 2003.

[148] G. Min, W. J. Choi, J. W. Kim and B. H. Lee, "Refractive index measurements of multiple layers using numerical refocusing in FF-OCT," *Optics express,* vol. 21, p. 29955–29967, 2013.

[149] F. Abelès, "La détermination de l'indice et de l'épaisseur des couches minces transparentes," 1950.

[150] J. Jin, J. W. Kim, C.-S. Kang, J.-A. Kim and T. B. Eom, "Thickness and refractive index measurement of a silicon wafer based on an optical comb," *Optics Express,* vol. 18, p. 18339–18346, 2010.

[151] H.-C. Cheng and Y.-C. Liu, "Simultaneous measurement of group refractive index and thickness of optical samples using optical coherence tomography," *Applied optics,* vol. 49, p. 790–797, 2010.

[152] W. V. Sorin and D. F. Gray, "Simultaneous thickness and group index measurement using optical low-coherence reflectometry," *Ieee Photonics Technology Letters,* vol. 4, p. 105–107, 1992.

[153] Y.-P. Wang, D.-N. Wang, W. Jin, J.-P. Chen, X.-W. Li and J.-H. Zhou, "Reflectometry measuring refractive index and thickness of polymer samples simultaneously," *Journal of Modern Optics,* vol. 53, p. 1845–1851, 2006.

[154] C.-T. Yen, J.-F. Huang, M.-J. Wu, Y.-F. Lee, C.-T. Huang, S.-F. Huang and H.-C. Cheng, "Simultaneously measuring the refractive index and thickness of an optical sample by using improved fiber-based optical coherence tomography," *Optical Engineering,* vol. 53, p. 044108, 2014.

[155] Y.-S. Ghim and S.-W. Kim, "Thin-film thickness profile and its refractive index measurements by dispersive white-light interferometry," *Optics express,* vol. 14, p. 11885–11891, 2006.

[156] S. J. Park, K. S. Park, Y. H. Kim and B. H. Lee, "Simultaneous measurements of refractive index and thickness by spectral-domain low coherence interferometry having dual sample probes," *IEEE Photonics Technology Letters,* vol. 23, p. 1076–1078, 2011.

[157] A. Hirai and H. Matsumoto, "Low-coherence tandem interferometer for measurement of group refractive index without knowledge of the thickness of the test sample," *Optics letters,* vol. 28, p. 2112–2114, 2003.

[158] H. Matsumoto, K. Sasaki and A. Hirai, "In situ measurement of group refractive index using tandem low-coherence interferometer," *Optics communications,* vol. 266, p. 214–217, 2006.

[159] V. Backman, M. B. Wallace, L. T. Perelman, J. T. Arendt, R. Gurjar, M. G. Müller, Q. Zhang, G. Zonios, E. Kline, T. McGillican and others, "Detection of preinvasive cancer cells," *nature,* vol. 406, p. 35–36, 2000.

[160] J. R. Mourant, I. J. Bigio, J. Boyer, R. L. Conn, T. Johnson and T. Shimada, "Spectroscopic diagnosis of bladder cancer with elastic light scattering," *Lasers in surgery and medicine,* vol. 17, p. 350–357, 1995.

[161] J. W. Pyhtila and A. Wax, "Rapid, depth-resolved light scattering measurements using Fourier domain, angle-resolved low coherence interferometry," *Optics Express,* vol. 12, p. 6178–6183, 2004.

[162] A. Wax, C. Yang and J. A. Izatt, "Fourier-domain low-coherence interferometry for light-scattering spectroscopy," *Optics letters,* vol. 28, p. 1230–1232, 2003.

[163] J. Yi, A. J. Radosevich, J. D. Rogers, S. C. P. Norris, İ. R. Çapoğlu, A. Taflove and V. Backman, "Can OCT be sensitive to nanoscale structural alterations in biological tissue?," *Optics express,* vol. 21, p. 9043–9059, 2013.

[164] H. L. Seck, Y. Zhang and Y. C. Soh, "Contrast enhancement using Mie spectra representation for spectroscopic optical coherence tomography," *Optics Communications,* vol. 338, p. 328–335, 2015.

[165] F. E. Robles, Y. Zhu, J. Lee, S. Sharma and A. Wax, "Detection of early colorectal cancer development in the azoxymethane rat carcinogenesis model with Fourier domain low coherence interferometry," *Biomedical optics express,* vol. 1, p. 736–745, 2010.

[166] C. Xu, P. S. Carney and S. A. Boppart, "Wavelength-dependent scattering in spectroscopic optical coherence tomography," *Optics express,* vol. 13, p. 5450–5462, 2005.

[167] R. N. Graf, F. E. Robles, X. Chen and A. P. Wax, "Detecting precancerous lesions in the hamster cheek pouch using spectroscopic white-light optical coherence tomography to assess nuclear morphology via spectral oscillations," *Journal of biomedical optics,* vol. 14, p. 064030, 2009.

[168] A. L. Oldenburg, C. Xu and S. A. Boppart, "Spectroscopic optical coherence tomography and microscopy," *IEEE Journal of Selected Topics in Quantum Electronics,* vol. 13, p. 1629–1640, 2007.

[169] D. C. Adler, T. H. Ko, P. R. Herz and J. G. Fujimoto, "Optical coherence tomography contrast enhancement using spectroscopic analysis with spectral autocorrelation," *Optics express,* vol. 12, p. 5487–5501, 2004.

[170] A. Kartakoullis, E. Bousi and C. Pitris, "Scatterer size-based analysis of optical coherence tomography images using spectral estimation techniques," *Optics express,* vol. 18, p. 9181–9191, 2010.

[171] V. Jaedicke, S. Agcaer, F. E. Robles, M. Steinert, D. Jones, S. Goebel, N. C. Gerhardt, H. Welp and M. R. Hofmann, "Comparison of different metrics for analysis and visualization in spectroscopic optical coherence tomography," *Biomedical optics express,* vol. 4, p. 2945–2961, 2013.

[172] B. C.-M. Tay, T.-H. Chow, B.-K. Ng and T. K.-S. Loh, "Dual-window dual-bandwidth spectroscopic optical coherence tomography metric for qualitative

scatterer size differentiation in tissues," *IEEE transactions on biomedical engineering*, vol. 59, p. 2439–2448, 2012.

[173] M. Kassinopoulos, E. Bousi, I. Zouvani and C. Pitris, "Correlation of the derivative as a robust estimator of scatterer size in optical coherence tomography (OCT)," *Biomedical optics express*, vol. 8, p. 1598–1606, 2017.

[174] A. Rosenfeld and A. C. Kak, *Digital image processing, Vol. 2*, Academic Press Amsterdam, 1982.

[175] M. D. Levine, Vision in man and machine, McGraw-Hill College, 1985.

[176] R. M. Haralick, "Statistical and structural approaches to texture," *Proceedings of the IEEE*, vol. 67, p. 786–804, 1979.

[177] J. Serra, "Image analysis and mathematical morphology. Academic Press, London.," *Image analysis and mathematical morphology. Academic Press, London.*, 1982.

[178] Y. Chen and E. R. Dougherty, "Gray-scale morphological granulometric texture classification," *Optical Engineering*, vol. 33, p. 2713–2723, 1994.

[179] J. S. Weszka, C. R. Dyer and A. Rosenfeld, "A comparative study of texture measures for terrain classification," *IEEE transactions on Systems, Man, and Cybernetics*, p. 269–285, 1976.

[180] B. Julesz, "Experiments in the visual perception of texture," *Scientific American*, vol. 232, p. 34–43, 1975.

[181] H. Niemann, Pattern analysis, vol. 4, Springer Science & Business Media, 2012.

[182] K. Valkealahti and E. Oja, "Reduced multidimensional co-occurrence histograms in texture classification," *IEEE Transactions on Pattern Analysis and Machine Intelligence*, vol. 20, p. 90–94, 1998.

[183] M. Strzelecki, "Segmentation of textured biomedical images using neural networks," in *IEEE Workshop on Signal Processing, Poznan*, 1995.

[184] G. R. Cross and A. K. Jain, "Markov random field texture models," *IEEE Transactions on Pattern Analysis and Machine Intelligence*, p. 25–39, 1983.

[185] B. S. Manjunath and R. Chellappa, "Unsupervised texture segmentation using Markov random field models," *IEEE Transactions on Pattern Analysis & Machine Intelligence*, p. 478–482, 1991.

[186] M. Cichy, A. Materka and J. Tuliszkiewicz, "Computerised analysis of X-ray images for early detection of osteoporotic changes in the bone," in *Proc. Conf. Information Technology in Medicine TIM '97, Jaszowiec, Poland*, 1997.

[187] L. M. Kaplan and C.-C. J. Kuo, "Texture roughness analysis and synthesis via extended self-similar (ESS) model," *IEEE Transactions on Pattern Analysis and Machine Intelligence*, vol. 17, p. 1043–1056, 1995.

[188] A. C. Bovik, "Properties of multichannel texture analysis filters," in *International Conference on Acoustics, Speech, and Signal Processing*, 1990.

[189] C. S. Lu, P. C. Chung, C. F. Chen and others, "Unsupervised texture segmentation via wavelet transform," *Pattern recognition*, vol. 30, p. 729–742, 1997.

[190] W.-K. Lam and C.-K. Li, "Rotated texture classification by improved iterative morphological decomposition," *IEE Proceedings-Vision, Image and Signal Processing*, vol. 144, p. 171–179, 1997.

[191] W. K. Pratt, "Digital image processing john wiley & sons," *Inc., New York*, 1991.

[192] M. Amadasun and R. King, "Textural features corresponding to textural properties," *IEEE Transactions on systems, man, and Cybernetics*, vol. 19, p. 1264–1274, 1989.

[193] K. W. Gossage, C. M. Smith, E. M. Kanter, L. P. Hariri, A. L. Stone, J. J. Rodriguez, S. K. Williams and J. K. Barton, "Texture analysis of speckle in optical coherence tomography images of tissue phantoms," *Physics in Medicine & Biology*, vol. 51, p. 1563, 2006.

[194] Y. Chen, A. D. Aguirre, P.-L. Hsiung, S.-W. Huang, H. Mashimo, J. M. Schmitt and J. G. Fujimoto, "Effects of axial resolution improvement on optical coherence tomography (OCT) imaging of gastrointestinal tissues," *Optics express*, vol. 16, p. 2469–2485, 2008.

[195] D. Harwood, T. Ojala, M. Pietikäinen, S. Kelman and L. Davis, "Texture classification by center-symmetric auto-correlation, using Kullback discrimination of distributions," *Pattern Recognition Letters*, vol. 16, p. 1–10, 1995.

[196] P. B. Garcia-Allende, I. Amygdalos, H. Dhanapala, R. D. Goldin, G. B. Hanna and D. S. Elson, "Morphological analysis of optical coherence tomography images for automated classification of gastrointestinal tissues," *Biomedical optics express*, vol. 2, p. 2821–2836, 2011.

[197] V. X. D. Yang, S.-j. Tang, M. L. Gordon, B. Qi, G. Gardiner, M. Cirocco, P. Kortan, G. B. Haber, G. Kandel, I. A. Vitkin and others, "Endoscopic Doppler optical

coherence tomography in the human GI tract: initial experience," *Gastrointestinal endoscopy,* vol. 61, p. 879–890, 2005.

[198] E. Osiac, A. Săftoiu, D. I. Gheonea, I. Mandrila and R. Angelescu, "Optical coherence tomography and Doppler optical coherence tomography in the gastrointestinal tract," *World journal of gastroenterology: WJG,* vol. 17, p. 15, 2011.

[199] K. Hufendiek, M.-A. Gamulescu, K. Hufendiek, H. Helbig and D. Märker, "Classification and characterization of acute macular neuroretinopathy with spectral domain optical coherence tomography," *International ophthalmology,* vol. 38, p. 2403–2416, 2018.

[200] V. Konidaris, S. Androudi, A. Alexandridis, A. Dastiridou and P. Brazitikos, "Optical coherence tomography-guided classification of epiretinal membranes," *International ophthalmology,* vol. 35, p. 495–501, 2015.

[201] S. Apinyawasisuk, T. McCannel and A. C. Arnold, "Clinical and spectral-domain optical coherence tomography appearance of optic disc melanocytoma: a new classification and differentiation from pigmented choroidal lesions," *Ocular oncology and pathology,* vol. 3, p. 142–148, 2017.

[202] P. Jelvehgaran, D. M. de Bruin, F. J. Salguero, G. R. Borst, J.-Y. Song, T. G. van Leeuwen, J. F. de Boer, T. Alderliesten and M. B. van Herk, "Feasibility of using optical coherence tomography to detect acute radiation-induced esophageal damage in small animal models," *Journal of biomedical optics,* vol. 23, p. 046004, 2018.

[203] A. Abdolmanafi, L. Duong, N. Dahdah and F. Cheriet, "Deep feature learning for automatic tissue classification of coronary artery using optical coherence tomography," *Biomedical optics express,* vol. 8, p. 1203–1220, 2017.

[204] T. Marvdashti, L. Duan, S. Z. Aasi, J. Y. Tang and A. K. E. Bowden, "Classification of basal cell carcinoma in human skin using machine learning and quantitative features captured by polarization sensitive optical coherence tomography," *Biomedical optics express,* vol. 7, p. 3721–3735, 2016.

[205] S. Adabi, M. Hosseinzadeh, S. Noei, S. Conforto, S. Daveluy, A. Clayton, D. Mehregan and M. Nasiriavanaki, "Universal in vivo textural model for human skin based on optical coherence tomograms," *Scientific reports,* vol. 7, p. 1–11, 2017.

[206] A. J. Trindade, B. J. George, J. Berkowitz, D. V. Sejpal and M. J. McKinley, "Volumetric laser endomicroscopy can target neoplasia not detected by conventional

endoscopic measures in long segment Barrett's esophagus," *Endoscopy international open,* vol. 4, p. E318–E322, 2016.

[207] N. S. Samel and H. Mashimo, "Application of OCT in the Gastrointestinal Tract," *Applied Sciences,* vol. 9, p. 2991, 2019.

[208] B. Mandebrot, "How long is the coast of britain," *Science,* vol. 156, p. 636–638, 1967.

[209] K. Falconer, Fractal geometry: mathematical foundations and applications, John Wiley & Sons, 2004.

[210] M. Long and F. Peng, "A box-counting method with adaptable box height for measuring the fractal feature of images," *Radioengineering,* vol. 22, p. 208–213, 2013.

[211] C. Flueraru, D. P. Popescu, Y. Mao, S. Chang and M. G. Sowa, "Added soft tissue contrast using signal attenuation and the fractal dimension for optical coherence tomography images of porcine arterial tissue," *Physics in Medicine & Biology,* vol. 55, p. 2317, 2010.

[212] A. C. Sullivan, J. P. Hunt and A. L. Oldenburg, "Fractal analysis for classification of breast carcinoma in optical coherence tomography," *Journal of biomedical optics,* vol. 16, p. 066010, 2011.

[213] W. Gao, V. P. Zakharov, O. O. Myakinin, I. A. Bratchenko, D. N. Artemyev and D. V. Kornilin, "Medical images classification for skin cancer using quantitative image features with optical coherence tomography," *Journal of Innovative Optical Health Sciences,* vol. 9, p. 1650003, 2016.

[214] O. Aharony, O. Gal-Or, A. Polat, Y. Nahum, D. Weinberger and Y. Zimmer, "Automatic Characterization of Retinal Blood Flow Using OCT Angiograms," *Translational Vision Science & Technology,* vol. 8, p. 6–6, 2019.

[215] S. Zahid, R. Dolz-Marco, K. B. Freund, C. Balaratnasingam, K. Dansingani, F. Gilani, N. Mehta, E. Young, M. R. Klifto, B. Chae and others, "Fractal dimensional analysis of optical coherence tomography angiography in eyes with diabetic retinopathy," *Investigative ophthalmology & visual science,* vol. 57, p. 4940–4947, 2016.

[216] T. Schmoll, A. S. G. Singh, C. Blatter, S. Schriefl, C. Ahlers, U. Schmidt-Erfurth and R. A. Leitgeb, "Imaging of the parafoveal capillary network and its integrity analysis using fractal dimension," *Biomedical optics express,* vol. 2, p. 1159–1168, 2011.

[217] G. M. Somfai, E. Tátrai, L. Laurik, B. E. Varga, V. Ölvedy, W. E. Smiddy, R. Tchitnga, A. Somogyi and D. C. DeBuc, "Fractal-based analysis of optical coherence tomography data to quantify retinal tissue damage," *BMC bioinformatics,* vol. 15, p. 295, 2014.

[218] N. Sandhya and K. R. Charanjeet, "A review on machine learning techniques," *International Journal on Recent and Innovation Trends in Computing and Communication,* vol. 4, p. 451–458, 2016.

[219] B. M. Dawant, M. Ozkan, H. Sprenkels, H. Aramata, K. Kawamura and R. A. Margolin, "A neural network approach to magnetic resonance imaging tissue characterization," *Communication, Control, and Signal Processing,* vol. 2, p. 1803–1809, 1990.

[220] G. R. Gindi, C. J. Darken, K. M. O'Brien, M. L. Stetz and L. I. Deckelbaum, "Neural network and conventional classifiers for fluorescence-guided laser angioplasty," *IEEE transactions on biomedical engineering,* vol. 38, p. 246–252, 1991.

[221] Z. Guo, L.-G. Durand, H. C. Lee, L. Allard, M.-C. Grenier and P. D. Stein, "Artificial neural networks in computer-assisted classification of heart sounds in patients with porcine bioprosthetic valves," *Medical and Biological Engineering and Computing,* vol. 32, p. 311–316, 1994.

[222] G. Coppini, R. Poli and G. Valli, "Recovery of the 3-D shape of the left ventricle from echocardiographic images," *IEEE transactions on medical imaging,* vol. 14, p. 301–317, 1995.

[223] P. M. Delaney, G. D. Papworth and R. G. King, "Fibre optic confocal imaging (FOCI) for in vivo subsurface microscopy of the colon," *Methods in disease investigating the gastrointestinal tract,* p. 169–178, 1998.

[224] E.-S. A. El-Dahshan, H. M. Mohsen, K. Revett and A.-B. M. Salem, "Computer-aided diagnosis of human brain tumor through MRI: A survey and a new algorithm," *Expert systems with Applications,* vol. 41, p. 5526–5545, 2014.

[225] S. B. Chaabane and F. Fnaiech, "Color edges extraction using statistical features and automatic threshold technique: application to the breast cancer cells," *Biomedical engineering online,* vol. 13, p. 4, 2014.

[226] Y. Wang, Z. Zhang, H. Wang and S. Bi, "Segmentation of the clustered cells with optimized boundary detection in negative phase contrast images," *PloS one,* vol. 10, 2015.

[227] X. Du and S. Dua, "Segmentation of fluorescence microscopy cell images using unsupervised mining," *The open medical informatics journal,* vol. 4, p. 41, 2010.

[228] S. Kharya, "Using data mining techniques for diagnosis and prognosis of cancer disease," *arXiv preprint arXiv:1205.1923,* 2012.

[229] B. Zheng, S. W. Yoon and S. S. Lam, "Breast cancer diagnosis based on feature extraction using a hybrid of K-means and support vector machine algorithms," *Expert Systems with Applications,* vol. 41, p. 1476–1482, 2014.

[230] O. Russakovsky, J. Deng, H. Su, J. Krause, S. Satheesh, S. Ma, Z. Huang, A. Karpathy, A. Khosla, M. Bernstein and others, "Imagenet large scale visual recognition challenge," *International journal of computer vision,* vol. 115, p. 211–252, 2015.

[231] M. Havaei, A. Davy, D. Warde-Farley, A. Biard, A. Courville, Y. Bengio, C. Pal, P.-M. Jodoin and H. Larochelle, "Brain tumor segmentation with deep neural networks," *Medical image analysis,* vol. 35, p. 18–31, 2017.

[232] A. Prasoon, K. Petersen, C. Igel, F. Lauze, E. Dam and M. Nielsen, "Deep feature learning for knee cartilage segmentation using a triplanar convolutional neural network," in *International conference on medical image computing and computer-assisted intervention,* 2013.

[233] P. Burlina, S. Billings, N. Joshi and J. Albayda, "Automated diagnosis of myositis from muscle ultrasound: Exploring the use of machine learning and deep learning methods," *PloS one,* vol. 12, 2017.

[234] M. Huang, W. Yang, Y. Wu, J. Jiang, Y. Gao, Y. Chen, Q. Feng, W. Chen and Z. Lu, "Content-based image retrieval using spatial layout information in brain tumor T1-weighted contrast-enhanced MR images," *PloS one,* vol. 9, 2014.

[235] T. Zeng and J. Liu, "Mixture classification model based on clinical markers for breast cancer prognosis," *Artificial Intelligence in Medicine,* vol. 48, p. 129–137, 2010.

[236] H.-L. Chen, B. Yang, J. Liu and D.-Y. Liu, "A support vector machine classifier with rough set-based feature selection for breast cancer diagnosis," *Expert Systems with Applications,* vol. 38, p. 9014–9022, 2011.

[237] J. F. G. Molina, L. Zheng, M. Sertdemir, D. J. Dinter, S. Schönberg and M. Rädle, "Incremental learning with SVM for multimodal classification of prostatic adenocarcinoma," *PloS one,* vol. 9, 2014.

[238] F. Ciompi, B. de Hoop, S. J. van Riel, K. Chung, E. T. Scholten, M. Oudkerk, P. A. de Jong, M. Prokop and B. van Ginneken, "Automatic classification of pulmonary peri-fissural nodules in computed tomography using an ensemble of 2D views and a convolutional neural network out-of-the-box," *Medical image analysis*, vol. 26, p. 195–202, 2015.

[239] H. Lu, H. Wang, Q. Zhang, D. Won and S. W. Yoon, "A dual-tree complex wavelet transform based convolutional neural network for human thyroid medical image segmentation," in *2018 IEEE International Conference on Healthcare Informatics (ICHI)*, 2018.

[240] Q. Zhang, H. Wang, H. Lu, D. Won and S. W. Yoon, "Medical image synthesis with generative adversarial networks for tissue recognition," in *2018 IEEE International Conference on Healthcare Informatics (ICHI)*, 2018.

[241] A. Abbasi, A. Monadjemi, L. Fang, H. Rabbani and Y. Zhang, "Three-dimensional optical coherence tomography image denoising through multi-input fully-convolutional networks," *Computers in biology and medicine*, vol. 108, p. 1–8, 2019.

[242] H. S. Salehi, M. Barchini and M. Mahdian, "Optimization methods for deep neural networks classifying OCT images to detect dental caries," in *Lasers in Dentistry XXVI*, 2020.

[243] J. Hossbach, L. Husvogt, M. F. Kraus, J. G. Fujimoto and A. K. Maier, "Deep OCT Angiography Image Generation for Motion Artifact Suppression," *arXiv preprint arXiv:2001.02512*, 2020.

[244] J. Lee, D. Prabhu, C. Kolluru, Y. Gharaibeh, V. N. Zimin, L. A. P. Dallan, H. G. Bezerra and D. L. Wilson, "Fully automated plaque characterization in intravascular OCT images using hybrid convolutional and lumen morphology features," *Scientific Reports*, vol. 10, p. 1–13, 2020.

[245] M. Christopher, C. Bowd, A. Belghith, M. H. Goldbaum, R. N. Weinreb, M. A. Fazio, C. A. Girkin, J. M. Liebmann and L. M. Zangwill, "Deep Learning Approaches Predict Glaucomatous Visual Field Damage from OCT Optic Nerve Head En Face Images and Retinal Nerve Fiber Layer Thickness Maps," *Ophthalmology*, vol. 127, p. 346–356, 2020.

[246] K. Dubey, N. Singla, A. Butola, A. Lathe, D. Quaiser, A. Srivastava, D. S. Mehta and V. Srivastava, "Ensemble classifier for improve diagnosis of the breast cancer using

optical coherence tomography and machine learning," *Laser Physics Letters,* vol. 16, p. 025602, 2019.

[247] A. Pérez del Palomar, J. Cegoñino, A. Montolío, E. Orduna, E. Vilades, B. Sebastián, L. E. Pablo and E. Garcia-Martin, "Swept source optical coherence tomography to early detect multiple sclerosis disease. The use of machine learning techniques.," *PloS one,* vol. 14, 2019.

[248] Y. He, A. Carass, B. M. Jedynak, S. D. Solomon, S. Saidha, P. A. Calabresi and J. L. Prince, "Topology guaranteed segmentation of the human retina from oct using convolutional neural networks," *arXiv preprint arXiv:1803.05120,* 2018.

[249] S. K. Devalla, K. S. Chin, J.-M. Mari, T. A. Tun, N. G. Strouthidis, T. Aung, A. H. Thiéry and M. J. A. Girard, "A deep learning approach to digitally stain optical coherence tomography images of the optic nerve head," *Investigative ophthalmology & visual science,* vol. 59, p. 63–74, 2018.

[250] C. Kolluru, D. Prabhu, Y. Gharaibeh, H. Wu and D. L. Wilson, "Voxel-based plaque classification in coronary intravascular optical coherence tomography images using decision trees," in *Medical Imaging 2018: Computer-Aided Diagnosis*, 2018.

[251] P. Gholami, M. S. Hassani, M. K. Parthasarathy, J. S. Zelek and V. Lakshminarayanan, "Classification of optical coherence tomography images for diagnosing different ocular diseases," in *Multimodal Biomedical Imaging XIII*, 2018.

[252] Y. Rong, D. Xiang, W. Zhu, K. Yu, F. Shi, Z. Fan and X. Chen, "Surrogate-assisted retinal OCT image classification based on convolutional neural networks," *IEEE journal of biomedical and health informatics,* vol. 23, p. 253–263, 2018.

[253] D. Li, J. Wu, Y. He, X. Yao, W. Yuan, D. Chen, H.-C. Park, S. Yu, J. L. Prince and X. Li, "Parallel deep neural networks for endoscopic OCT image segmentation," *Biomedical optics express*, vol. 10, p. 1126–1135, 2019.

[254] F. Li, H. Chen, Z. Liu, X. Zhang and Z. Wu, "Fully automated detection of retinal disorders by image-based deep learning," *Graefe's Archive for Clinical and Experimental Ophthalmology,* vol. 257, p. 495–505, 2019.

[255] M. M. G. d. Macedo, C. K. Takimura, P. A. Lemos and M. A. Gutierrez, "A robust fully automatic lumen segmentation method for in vivo intracoronary optical coherence tomography," *Research on Biomedical Engineering,* vol. 32, p. 35–43, 2016.

[256] T. Heimann and H.-P. Meinzer, "Statistical shape models for 3D medical image segmentation: a review," *Medical image analysis,* vol. 13, p. 543–563, 2009.

[257] D. Terzopoulos, A. Witkin and M. Kass, "Constraints on deformable models: Recovering 3D shape and nonrigid motion," *Artificial intelligence,* vol. 36, p. 91–123, 1988.

[258] D. Cremers, M. Rousson and R. Deriche, "A review of statistical approaches to level set segmentation: integrating color, texture, motion and shape," *International journal of computer vision,* vol. 72, p. 195–215, 2007.

[259] A. Baghaie, Z. Yu and R. M. D'Souza, "State-of-the-art in retinal optical coherence tomography image analysis," *Quantitative imaging in medicine and surgery,* vol. 5, p. 603, 2015.

[260] H. S. Nam, C.-S. Kim, J. J. Lee, J. W. Song, J. W. Kim and H. Yoo, "Automated detection of vessel lumen and stent struts in intravascular optical coherence tomography to evaluate stent apposition and neointimal coverage," *Medical physics,* vol. 43, p. 1662–1675, 2016.

[261] A. Fuller, R. Zawadzki, S. Choi, D. Wiley, J. Werner and B. Hamann, "Segmentation of three-dimensional retinal image data," *IEEE transactions on visualization and computer graphics,* vol. 13, p. 1719–1726, 2007.

[262] M. K. Garvin, M. D. Abramoff, X. Wu, S. R. Russell, T. L. Burns and M. Sonka, "Automated 3-D intraretinal layer segmentation of macular spectral-domain optical coherence tomography images," *IEEE transactions on medical imaging,* vol. 28, p. 1436–1447, 2009.

[263] Y.-Y. Liu, M. Chen, H. Ishikawa, G. Wollstein, J. S. Schuman and J. M. Rehg, "Automated macular pathology diagnosis in retinal OCT images using multi-scale spatial pyramid and local binary patterns in texture and shape encoding," *Medical image analysis,* vol. 15, p. 748–759, 2011.

[264] A. Yazdanpanah, G. Hamarneh, B. R. Smith and M. V. Sarunic, "Segmentation of intra-retinal layers from optical coherence tomography images using an active contour approach," *IEEE transactions on medical imaging,* vol. 30, p. 484–496, 2010.

[265] J. Xu, H. Ishikawa, G. Wollstein and J. S. Schuman, "3D optical coherence tomography super pixel with machine classifier analysis for glaucoma detection," in *2011 Annual International Conference of the IEEE Engineering in Medicine and Biology Society*, 2011.

[266] H. Lu, M. Gargesha, Z. Wang, D. Chamie, G. F. Attizzani, T. Kanaya, S. Ray, M. A. Costa, A. M. Rollins, H. G. Bezerra and others, "Automatic stent detection in intravascular OCT images using bagged decision trees," *Biomedical optics express*, vol. 3, p. 2809–2824, 2012.

[267] N. Anantrasirichai, A. Achim, J. E. Morgan, I. Erchova and L. Nicholson, "SVM-based texture classification in optical coherence tomography," in *2013 IEEE 10th International Symposium on Biomedical Imaging*, 2013.

[268] P. P. Srinivasan, L. A. Kim, P. S. Mettu, S. W. Cousins, G. M. Comer, J. A. Izatt and S. Farsiu, "Fully automated detection of diabetic macular edema and dry age-related macular degeneration from optical coherence tomography images," *Biomedical optics express*, vol. 5, p. 3568–3577, 2014.

[269] S. P. K. Karri, D. Chakraborty and J. Chatterjee, "Transfer learning based classification of optical coherence tomography images with diabetic macular edema and dry age-related macular degeneration," *Biomedical optics express*, vol. 8, p. 579–592, 2017.

[270] M. Lenz, R. Krug, H. Welp, K. Schmieder and M. R. Hofmann, "Ex vivo brain tumor analysis using spectroscopic optical coherence tomography," in *Optical Coherence Tomography and Coherence Domain Optical Methods in Biomedicine XX*, 2016.

[271] K. Alsaih, G. Lemaître, J. M. Vall, M. Rastgoo, D. Sidibé, T. Y. Wong, E. Lamoureux, D. Milea, C. Y. Cheung and F. Mériaudeau, "Classification of SD-OCT volumes with multi pyramids, LBP and HOG descriptors: application to DME detections," in *2016 38th Annual International Conference of the IEEE Engineering in Medicine and Biology Society (EMBC)*, 2016.

[272] Y. Wang, Y. Zhang, Z. Yao, R. Zhao and F. Zhou, "Machine learning based detection of age-related macular degeneration (AMD) and diabetic macular edema (DME) from optical coherence tomography (OCT) images," *Biomedical optics express*, vol. 7, p. 4928–4940, 2016.

[273] G. J. Ughi, M. J. Gora, A.-F. Swager, A. Soomro, C. Grant, A. Tiernan, M. Rosenberg, J. S. Sauk, N. S. Nishioka and G. J. Tearney, "Automated segmentation and characterization of esophageal wall in vivo by tethered capsule optical coherence tomography endomicroscopy," *Biomedical optics express*, vol. 7, p. 409–419, 2016.

[274] C. A. Lingley-Papadopoulos, M. H. Loew, M. J. Manyak and J. M. Zara, "Computer recognition of cancer in the urinary bladder using optical coherence tomography and texture analysis," *Journal of biomedical optics,* vol. 13, p. 024003, 2008.

[275] W. Ding, M. Young, S. Bourgault, S. Lee, D. A. Albiani, A. W. Kirker, F. Forooghian, M. V. Sarunic, A. B. Merkur and M. F. Beg, "Automatic detection of subretinal fluid and sub-retinal pigment epithelium fluid in optical coherence tomography images," in *2013 35th Annual International Conference of the IEEE Engineering in Medicine and Biology Society (EMBC)*, 2013.

[276] A. Lang, A. Carass, M. Hauser, E. S. Sotirchos, P. A. Calabresi, H. S. Ying and J. L. Prince, "Retinal layer segmentation of macular OCT images using boundary classification," *Biomedical optics express,* vol. 4, p. 1133–1152, 2013.

[277] A. Albarrak, F. Coenen and Y. Zheng, "Dictionary learning-based volumetric image classification for the diagnosis of age-related macular degeneration," in *International Workshop on Machine Learning and Data Mining in Pattern Recognition*, 2014.

[278] T. Yoshida, A. Iwase, H. Hirasawa, H. Murata, C. Mayama, M. Araie and R. Asaoka, "Discriminating between glaucoma and normal eyes using optical coherence tomography and the 'Random Forests' classifier," *PloS one,* vol. 9, 2014.

[279] R. Kafieh, H. Rabbani and I. Selesnick, "Three dimensional data-driven multi scale atomic representation of optical coherence tomography," *IEEE transactions on medical imaging,* vol. 34, p. 1042–1062, 2014.

[280] M. S. Miri, M. D. Abràmoff, K. Lee, M. Niemeijer, J.-K. Wang, Y. H. Kwon and M. K. Garvin, "Multimodal segmentation of optic disc and cup from SD-OCT and color fundus photographs using a machine-learning graph-based approach," *IEEE transactions on medical imaging,* vol. 34, p. 1854–1866, 2015.

[281] H. Bogunović, M. D. Abràmoff and M. Sonka, "Geodesic graph cut based retinal fluid segmentation in optical coherence tomography," 2015.

[282] Y. Gan, D. Tsay, S. B. Amir, C. C. Marboe and C. P. Hendon, "Automated classification of optical coherence tomography images of human atrial tissue," *Journal of biomedical optics,* vol. 21, p. 101407, 2016.

[283] D. Lu, M. Heisler, S. Lee, G. Ding, M. V. Sarunic and M. F. Beg, "Retinal fluid segmentation and detection in optical coherence tomography images using fully convolutional neural network," *arXiv preprint arXiv:1710.04778,* 2017.

[284] L. Fang, D. Cunefare, C. Wang, R. H. Guymer, S. Li and S. Farsiu, "Automatic segmentation of nine retinal layer boundaries in OCT images of non-exudative AMD patients using deep learning and graph search," *Biomedical optics express*, vol. 8, p. 2732–2744, 2017.

[285] A. Breger, M. Ehler, H. Bogunovic, S. M. Waldstein, A.-M. Philip, U. Schmidt-Erfurth and B. S. Gerendas, "Supervised learning and dimension reduction techniques for quantification of retinal fluid in optical coherence tomography images," *Eye*, vol. 31, p. 1212–1220, 2017.

[286] C. S. Lee, A. J. Tyring, N. P. Deruyter, Y. Wu, A. Rokem and A. Y. Lee, "Deep-learning based, automated segmentation of macular edema in optical coherence tomography," *Biomedical optics express*, vol. 8, p. 3440–3448, 2017.

[287] A. Moiseev, L. Snopova, S. Kuznetsov, N. Buyanova, V. Elagin, M. Sirotkina, E. Kiseleva, L. Matveev, V. Zaitsev, F. Feldchtein and others, "Pixel classification method in optical coherence tomography for tumor segmentation and its complementary usage with OCT microangiography," *Journal of biophotonics*, vol. 11, p. e201700072, 2018.

[288] N. Gessert, M. Schlüter and A. Schlaefer, "A deep learning approach for pose estimation from volumetric OCT data," *Medical image analysis*, vol. 46, p. 162–179, 2018.

[289] T. W. Sawyer, P. F. S. Rice, D. M. Sawyer, J. W. Koevary and J. K. Barton, "Evaluation of segmentation algorithms for optical coherence tomography images of ovarian tissue," in *Diagnosis and Treatment of Diseases in the Breast and Reproductive System IV*, 2018.

[290] T. M. Aslam, H. R. Zaki, S. Mahmood, Z. C. Ali, N. A. Ahmad, M. R. Thorell and K. Balaskas, "Use of a neural net to model the impact of optical coherence tomography abnormalities on vision in age-related macular degeneration," *American journal of ophthalmology*, vol. 185, p. 94–100, 2018.

[291] L. Fang, C. Wang, S. Li, H. Rabbani, X. Chen and Z. Liu, "Attention to lesion: Lesion-aware convolutional neural network for retinal optical coherence tomography image classification," *IEEE transactions on medical imaging*, vol. 38, p. 1959–1970, 2019.

[292] D. Lu, M. Heisler, S. Lee, G. W. Ding, E. Navajas, M. V. Sarunic and M. F. Beg, "Deep-learning based multiclass retinal fluid segmentation and detection in optical

coherence tomography images using a fully convolutional neural network," *Medical image analysis,* vol. 54, p. 100–110, 2019.

[293] C. Photiou, E. Bousi, I. Zouvani and C. Pitris, "Using speckle to measure tissue dispersion in optical coherence tomography," *Biomed. Opt. Express,* vol. 8, p. 2528–2535, 5 2017.

[294] N. Meitav, E. N. Ribak and S. Shoham, "Point spread function estimation from projected speckle illumination," *Light: Science & Applications,* vol. 5, p. e16048–e16048, 2016.

[295] C. Photiou, E. Bousi, I. Zouvani and C. Pitris, "Measuring tissue dispersion using the cross-correlation of half-spectrum optical coherence tomography images," in *Optical Coherence Tomography and Coherence Domain Optical Methods in Biomedicine XXIII*, 2019.

[296] C. Photiou and C. Pitris, "Comparison of tissue dispersion measurement techniques based on optical coherence tomography," *Journal of biomedical optics,* vol. 24, p. 046003, 2019.

[297] I. H. Malitson, "Refractive properties of barium fluoride," *JOSA,* vol. 54, p. 628–632, 1964.

[298] H. H. Li, "Refractive index of alkali halides and its wavelength and temperature derivatives," *Journal of physical and chemical reference data,* vol. 5, p. 329–528, 1976.

[299] M. Debenham, "Refractive indices of zinc sulfide in the 0.405–13-μm wavelength range," *Applied optics,* vol. 23, p. 2238–2239, 1984.

[300] C. Photiou and C. Pitris, "Dual-angle optical coherence tomography for index of refraction estimation using rigid registration and cross-correlation," *Journal of biomedical optics,* vol. 24, p. 106001, 2019.

[301] Y. Díez, A. Oliver, X. Llado, J. Freixenet, J. Marti, J. C. Vilanova and R. Marti, "Revisiting intensity-based image registration applied to mammography," *IEEE Transactions on Information Technology in Biomedicine,* vol. 15, p. 716–725, 2011.

[302] A. E. Desjardins, B. J. Vakoc, W.-Y. Oh, S. M. R. Motaghiannezam, G. J. Tearney and B. E. Bouma, "Angle-resolved optical coherence tomography with sequential angular selectivity for speckle reduction," *Optics express,* vol. 15, p. 6200–6209, 2007.

[303] C. Photiou, G. Plastiras, G. Tearney and C. Pitris, "Comparison of classification methods of Barret's and dysplasia in the esophagus from in vivo optical coherence tomography images," in *Optical Coherence Tomography and Coherence Domain Optical Methods in Biomedicine XXIV*, 2020.

[304] E. Downs-Kelly, J. E. Mendelin, A. E. Bennett, E. Castilla, W. H. Henricks, L. Schoenfield, M. Skacel, L. Yerian, T. W. Rice, L. A. Rybicki and others, "Poor interobserver agreement in the distinction of high-grade dysplasia and adenocarcinoma in pretreatment Barrett's esophagus biopsies," *American Journal of Gastroenterology*, vol. 103, p. 2333–2340, 2008.

[305] M. J. Gora, J. S. Sauk, R. W. Carruth, K. A. Gallagher, M. J. Suter, N. S. Nishioka, L. E. Kava, M. Rosenberg, B. E. Bouma and G. J. Tearney, "Tethered capsule endomicroscopy enables less invasive imaging of gastrointestinal tract microstructure," *Nature medicine,* vol. 19, p. 238–240, 2013.

[306] J. R. Quinlan, "Induction of decision trees," *Machine learning,* vol. 1, p. 81–106, 1986.

[307] D. Opitz and R. Maclin, "Popular ensemble methods: An empirical study," *Journal of artificial intelligence research,* vol. 11, p. 169–198, 1999.

[308] B. J. Erickson, P. Korfiatis, Z. Akkus and T. L. Kline, "Machine learning for medical imaging," *Radiographics,* vol. 37, p. 505–515, 2017.

[309] E. R. Diaz and S. K. Singh, "Computer-Assisted Image Interpretation of Volumetric Laser Endomicroscopy in Barrett's Esophagus," *AGA,* 2015.

[310] A.-F. Swager, F. van der Sommen, S. R. Klomp, S. Zinger, S. L. Meijer, E. J. Schoon, J. J. G. H. M. Bergman, H. Peter and W. L. Curvers, "Computer-aided detection of early Barrett's neoplasia using volumetric laser endomicroscopy," *Gastrointestinal endoscopy,* vol. 86, p. 839–846, 2017.

[311] R. Fonollà, T. Scheeve, M. R. Struyvenberg, W. L. Curvers, A. J. de Groof, F. van der Sommen, E. J. Schoon, J. J. G. H. M. Bergman and others, "Ensemble of deep convolutional neural networks for classification of early Barrett's neoplasia using volumetric laser endomicroscopy," *Applied Sciences,* vol. 9, p. 2183, 2019.

[312] J. van der Putten, M. Struyvenberg, J. de Groof, T. Scheeve, W. Curvers, E. Schoon, J. J. G. H. M. Bergman, P. H. N. de With and F. van der Sommen, "Deep principal dimension encoding for the classification of early neoplasia in Barrett's Esophagus

with volumetric laser endomicroscopy," *Computerized Medical Imaging and Graphics,* vol. 80, p. 101701, 2020.